
Gravitational Waves from Binary Neutron Star systems

DISSERTATION

zur Erlangung des akademischen Grades
doctor rerum naturalium (Dr. rer. nat.)



**FRIEDRICH-SCHILLER-
UNIVERSITÄT
JENA**

vorgelegt dem Rat der
PHYSIKALISCH-ASTRONOMISCHEN FAKULTÄT
der
FRIEDRICH-SCHILLER-UNIVERSITÄT JENA
von

Reetika Dudi (M.tech)

geboren am 06.09.1991 in Timarni

GUTACHER:

1. PROF. DR. BERND BRÜGMANN (FRIEDRICH-SCHILLER-UNIVERSITÄT JENA)
2. DR. JOHN VEITCH (UNIVERSITY OF GLASGOW, UK)
3. PROF. DR. AJITH PARAMESWARAN (ICTS, TIFR, BANGALORE)

TAG DER DISPUTATION: 15.05.2020

Dissertation, Friedrich-Schiller-Universität Jena, [2020].

Dedicated to all the girls who dare to dream regardless of the circumstances,

and to my beloved brother, Raju Bhaiya.

Abbreviations and Notation

We employ geometrized units with $c = G = M_{\odot} = 1$ throughout this work. In some cases, c, G, M_{\odot} are given explicitly for better understanding. We use Greek letters like μ for four-dimensional indices running from 0 to 3 and Latin letters like i for three-dimensional indices running from 1 to 3. We refer to most references using numbers except for references to our own publications for which we use Arabic numerals. The following abbreviations are used throughout the thesis, in most cases these abbreviations are also introduced in the text at their first appearance:

BAM	Bi-functional Adaptive Mesh (code name)
BBH	binary-black holes
BH	black hole
BNS	binary neutron stars
BSSN	Baumgarte-Shapiro-Shibata-Nakamura
CRV	constant rotational velocity
EOB	effective-one-body
EOS	equation-of-state
Eq.	equation
GR	General Relativity
GRB	gamma-ray burst
GRHD	General relativistic hydrodynamics
GW	gravitational-wave
HMNS	hypermassive neutron star
LIGO	Laser Interferometer Gravitational Wave Observatory
LORENE	Langage objet pour la relativite numerique (code name)
LVC	LIGO/Virgo collaboration
LSC	LIGO Scientific Collaboration
NLO	next to leading order
NNLO	next to next to leading order
NR	Numerical-relativity
NS	Neutron star
ODE	ordinary-differential-equation
O1	first observing run
O2	second observing run
O3	third observing run
PDE	partial differential equations
PDF	probability density function
PN	post-Newtonian

PSD	power spectral density
PSDs	power spectral densities
SNR	signal-to-noise ratio
ZDHP	zero-detuned high-power configuration

Abstract

The first observation of gravitational waves from a merger of binary neutron stars (BNS) along with measurements of electromagnetic counterpart has led the beginning of multimessenger gravitational wave astronomy. In this thesis, we investigate various gravitational waveform models. These models are employed for extracting source properties from the gravitational wave signal from the BNS merger. We perform parameter estimation studies in order to deduce the systematics among these models. We employ different injection scenarios to understand the biases that occur due to differences in the physics included in different waveform models. We present the construction of hybrid waveforms and discuss their applications as a full waveform, e.g., for validation of other waveform models and to check the performance of the models by performing mismatch calculations and parameter estimation studies where hybrid waveforms used as a substitute for a real signal. Based on the systematics study, we show a few of the waveform models give biased estimates of the parameters for specific injection scenarios. We improve those models and present the results of the improved models. In the context of having an accurate yet fast-to-evaluate waveform model, we review reduced-order-modeling techniques and present its application for the multipolar `TEOBResum` model.

Furthermore, to validate and tune analytical models, and to investigate the last few orbits near the merger and after the merger, numerical simulations are inevitable. We evaluate the performance of an initial data generating code, called *new* SGRID code for BNS systems. With the upcoming advance detectors, it is highly likely that events with extreme source properties will get observed. Therefore, in this thesis, we show preliminary results for numerical simulations of BNS mergers with high spins. We vary equation-of-states (EOSs) and spins to investigate the effects of spin and EOS on the dynamics and gravitational waves.

Contents

Abbreviations and Notation	v
Abstract	vii
1 Introduction	3
2 Basics of Gravitational waves	7
2.1 Basics: Theory of General Relativity	7
2.2 Sources of gravitational waves: Binary Neutron Stars	12
2.3 Bayesian Inference	15
2.4 GW170817 event	18
3 Waveform models	24
3.1 Post-Newtonian waveforms	24
3.2 Effective-one-body family	27
3.3 Phenomenological family	29
3.4 NRTidal model	31
4 Hybrid waveform	34
4.1 Applications	39
5 Waveform systematic study	42
5.1 Systematics study	42
5.1.1 Effects of tidal terms	45
5.1.2 Effect of postmerger	50
5.2 GW170817- systematics study	53
6 Improving the waveform models	58
6.1 TaylorF2 at quasi 5.5 post Newtonian	58
6.1.1 Q_ω analysis	59
6.1.2 Effect on $\tilde{\Lambda}$ inference	61
6.2 NRTidalv2 model	66
6.3 Surrogate Model	69

6.3.1	Results	72
7	Numerical simulations	76
7.1	Numerical relativity	76
7.2	Initial data	79
7.3	Spinning BNS mergers	84
7.3.1	Analysis	85
8	Conclusion	97
Appendix A	Quasi-5.5PN-accurate orbital phasing	102
Appendix B	Algorithms for Surrogate model	105
Appendix C	SGRID	107
Publications		110

Chapter 1

Introduction

When a giant star runs out of fuel, its core collapses, squeezing the electrons and protons to form an object mostly consisting of neutrons and neutrinos. If the star is lighter than $\sim 3M_{\odot}$, then the neutron pressure keeps it stable; otherwise, it collapses to a black hole. This stable star is called a neutron star (NS). NSs are 10 - 15 km in radii and have masses around 1 - 3 M_{\odot} , thus are one of the most compact objects in the known universe [1–3]. A merger of two such compact objects is an exotic event, provides multi-wavelength observation (from X-ray to optical and radio), and emits gravitational-waves (GWs). GWs can be understood as waves of distorted space, radiated away from the source, traveling through the spacetime at the speed of light [3–5]. GWs arise in General Relativity (GR) due to time-varying quadrupole and higher-order multipole moments. They contain important information about their sources as they emerge from regions of strong gravity and relativistic motion. They interact very weakly with matter, which makes them ideal for investigating the nature of spacetime and matter under extreme conditions of gravity, density, and pressure.

During the first observing run (*O1*) of the LIGO detectors at Hanford and Livingston, the first direct detection of the GW signal from a coalescing binary-black hole (BBH) was made [6] on 14th September 2015. In *O1* and second observing run (*O2*), several GW signals were detected consistent with the inspiral and merger of BBHs. Moreover, during *O2*, first signal consistent with a binary neutron star (BNS) merger was detected (GW170817) on 14th August 2017 [Collab1], along with the observation of electromagnetic counterparts (see [7]). A short gamma-ray burst (GRB) GRB-170817A was observed 1.7 seconds after the GW detection by Fermi Gamma-ray Space Telescope and the International Gamma-Ray Astrophysics Laboratory.

These electromagnetic observations supported the hypothesis of BNS mergers as the progenitor of short GRBs. This spectacular event has started a new era of multi-messenger astronomy. As predicted, the direct detection of the BNS merger has

provided unique opportunities to answer long-standing questions in astrophysics. For example, GW170817 was used to place a constraint on the behavior of matter at supranuclear densities [8–12] and sites where heavy elements form. The detection also led to an independent measure of Hubble constant [13]. GW170817 also ruled out a large class of modified gravity theories by placing a limit on the difference in speed of gravity and electromagnetic waves. We discuss the properties of GW170817 in Sec. 2.4 in detail. A complete analysis of the source properties measured from GW170817 is given in Ref. [Collab2].

To date, ten signals consistent with BBH mergers and one with BNS coalescence have been observed in *O1* and *O2* [14]. We have seen and expect to see many more detections in the third observing run (*O3*), which is currently ongoing (started in April 2019). All three GW detectors, LIGO Hanford and Louisiana (in the US, [15]) and the Virgo detector in Italy [16] are operational in *O3* which was not the case for the entire duration of *O1* and *O2*¹, and the sensitivity of the detectors have been improved. Therefore, signals with extreme source properties are expected.

The detection and extraction of source properties of such signals are of great importance for both astrophysics and nuclear physics. GWs are used to test General Relativity (GR) in dynamical spacetime and provide insights into the nature of the matter in the strong-field regime. The upcoming next-generation GW observatories (3G), like the Einstein Telescope and Cosmic Explorer, will observe sources at high redshift ($z \sim 10 - 20$), i.e., 3G detectors will see mergers of black holes (BHs) and NSs from a very early time, probably from the first stars and BHs. We hope to see extremely bright events that might offer some hints of new physics. We expect to observe other classes of compact objects, such as boson, axion, and gravastars stars, which are theoretically predicted in extensions to GR or rule them out. At the sensitivity of future detectors, the measurement of the merger and post-merger regimes of the BNS signal is expected, which will help in constraining the cold EOS, and with more observations, we will constrain the EOS at supranuclear densities significantly better.

There are two categories, modeled search and unmodeled search for detecting the signal deep buried in the detector noise. Unmodeled search is for signals such as stochastic background, signals from rotating NSs with asymmetry, asymmetric core-collapse supernovae, etc., for which we do not have a model to describe the signal. Though, we sometimes do employ unmodeled search for coalescing compact binary signals. These searches are less sensitive than modeled searches. For signals from coalescing compact binaries, such as merging BBH, BNS, and BH-NS, we employ modeled or semi-modeled searches. Accurate waveform templates are necessary for the detection, as well as for inferring the properties of the source of the signals for

¹Virgo joined *O2* in August 2017

modeled search. There are several waveform models (discussed in Chapter 3), also called approximants, implemented in LSC (LIGO Scientific Collaboration)-Algorithm Library (LAL) to facilitate the searches and estimating the parameters of the source. It is essential to understand the systematics among the existing waveform models in order to make meaningful statements about the source properties at the end. It is crucial to improve these approximants such that accurate and fast waveforms can be generated in the unexplored regions of the parameter space for the analysis of upcoming events with extreme properties as the Advanced LIGO and VIRGO detectors are at high sensitivity. In this thesis, we mainly focus on the BNS merger as a source of GWs. For the inspiral regime, when the two compact objects are well-separated, analytical models like post-Newtonian (PN) and analytical approximations like effective-one-body (EOB) are used to generate template waveforms. However, for information near merger, numerical simulations of the non-linear field equation with full relativistic hydrodynamics is required. Numerical-relativity (NR) waveforms are also required to tune and validate the analytical approximation.

We explore three different aspects of GW data analysis in this thesis, namely, understanding the waveform models, improving the current waveform models, and performing numerical simulations with extreme parameters to provide high-resolution waveforms, which can be used as a testbed to extract the spin and tidal effects. The thesis is organized as follows: In Chapter 2, we discuss the basic concepts related to GWs, sources of GWs, and Bayesian inference algorithm employed to extract the source properties. We also discuss the properties of the first BNS detection GW170817 [Collab1, Collab2]. In Chapter 3, we discuss various waveform model families like PN, EOB, and phenomenological waveforms and also discuss various approximants derived from these families like TaylorF2, IMRPhenomD, TEOBResumS, etc. However, these waveforms do not cover the full inspiral-merger-post-merger regime. One can join together waveform for the inspiral regime and NR waveforms, which describe merger and post-merger regime, to obtain full waveforms called hybrid waveforms. We discuss the construction of hybrid waveforms in Chapter 4. We also discuss some of their applications; as an example, we show how the NRTidal model can be evaluated using hybrid waveforms. We calculate mismatches between the NRTidal model with several hybrid waveforms in order to test its performance. The hybrid waveforms are publicly available on the CoRe database², cf. [Collab3]. In Chapter 5, we explore systematic differences among various waveform models. We inject hybrid waveforms as a real signal in the LIGO data stream and recover their parameters by employing different waveform approximants. We then investigate the biases in the extracted parameters. We also study the impact of the presence of the post-merger regime in the signal, but absent in approximants, on parameter esti-

²<http://www.computational-relativity.org/>

mates [Dudi1]. We find that some of the waveforms models are giving biased results due to approximate treatment of the physics. We improve these waveform models and discuss the results in Chapter 6. For example, we implemented TaylorF2 at quasi 5.5 PN waveform model in LAL and studied its improvement over TaylorF2 at 3.5 PN by comparing the results of parameter estimation and Q_ω relation [Dudi2]. We review the reduced-order-modeling techniques to generate compact, accurate, and fast-to-evaluate waveforms in place of a very accurate but slow waveform model [Dudi7].

Furthermore, to probe the last orbits around the merger, to describe the post-merger dynamics and to tune and validate the analytical models, NR simulations are essential. We present a preliminary numerical investigation of BNS mergers with very high spins in Chapter 7. The initial data is constructed using a new code called *new* SGRID code (developed by Tichy et al.) [Dudi5] and evolved by employing the BAM code, followed by the eccentricity reduction procedure. We also evaluate the performance of the *new* SGRID code for the BNS merger. We would like to provide the high spinning gravitational waveforms as a testbed to extract the spin effects in the GW phase evolution and to test other semi-analytical waveform models [Dudi6].

For additional information, we provide a derivation of quasi 5.5 PN phasing in Appendix A, algorithms employed in the construction of the surrogate model in Appendix B, and basic framework of the *new* SGRID code in Appendix C.

Chapter 2

Basics of Gravitational waves

In this chapter, we briefly illustrate the origin of GWs in GR and discuss some of their properties. We also explore BNS, as a source of GWs and discuss the effects of NS matter on GWs due to tidal interaction between two NSs. Then, very briefly, we discuss *Bayesian* analysis which is a tool to estimate the source properties once the GW signal gets measured. For a more detailed description of GWs, we refer the reader to Refs. [4, 5, 17, 18]

2.1 Basics: Theory of General Relativity

The theory of general relativity states that gravitation is not a force but rather a manifestation of the curvature (R) of spacetime, which is related to the local energy-momentum tensor ($T_{\mu\nu}$) [4]:

$$G_{\mu\nu} \equiv R_{\mu\nu} - \frac{1}{2}g_{\mu\nu}R = 8\pi T_{\mu\nu} \quad (G = 1), \quad (2.1)$$

where $G_{\mu\nu}$ is the Einstein tensor, $R_{\mu\nu}$ is the Ricci curvature tensor and is obtained by contracting Riemann tensor ($R^\alpha_{\beta\mu\nu}$) on the first and third indices. R is the Ricci scalar and obtained by contracting Ricci tensor, and $g_{\mu\nu}$ is the spacetime metric. Eq. (2.1) known as Einstein's field equation. The Riemann tensor is given by:

$$R^\alpha_{\beta\mu\nu} = \partial_\mu \Gamma^\alpha_{\beta\nu} - \partial_\nu \Gamma^\alpha_{\beta\mu} + \Gamma^\alpha_{\gamma\mu} \Gamma^\gamma_{\beta\nu} - \Gamma^\alpha_{\gamma\nu} \Gamma^\gamma_{\beta\mu}, \quad (2.2)$$

where $\Gamma^\gamma_{\mu\nu}$ are the affine connection coefficients to the metric, called Christoffel symbols and are defined as:

$$\Gamma^\gamma_{\mu\nu} = \frac{1}{2}g^{\gamma\beta}(\partial_\nu g_{\beta\mu} + \partial_\mu g_{\beta\nu} - \partial_\beta g_{\mu\nu}). \quad (2.3)$$

Here ∂_μ means the partial derivative $\partial/\partial x^\mu$. Though gravity is strong near compact and heavy objects like BHs and NSs, it is weak in most places in the universe. The study of weak gravitational fields is important as it leads to the derivation of

gravitational radiation.

Linearised theory of gravity

Eq. (2.1) is a set of complicated non-linear second-order differential equations. These equations can be simplified using perturbation theory in the weak field limit, where the deviation from the exact solution is small. Linearized gravity is a suitable approximation to GR when gravity is weak, i.e., the spacetime metric $g_{\mu\nu}$ can be treated as a slight deviation from the flat Minkowski metric $\eta_{\mu\nu}$:

$$g_{\mu\nu} = \eta_{\mu\nu} + h_{\mu\nu}, \quad (2.4)$$

where $\eta_{\mu\nu}$ is $\text{diag}(-1,1,1,1)$ and $h_{\mu\nu}$ is a small metric perturbation. We assume $\|h_{\mu\nu}\| \ll 1$, which allows us to ignore higher order terms in this quantity and impose the gravitational field to be weak. Thus, indices are raised and lowered using the flat metric $\eta_{\mu\nu}$. The Lorentz transform (Λ^ν_μ) of the metric Eq. (2.4), shows that $h_{\mu\nu}$ transforms as a rank 2 tensor (2.5), but not under general coordinate transformations. Therefore, we can think of the metric perturbation as a tensor field propagating on the background spacetime.

$$h_{\bar{\mu}\bar{\nu}} = \Lambda^\mu_{\bar{\mu}} \Lambda^\nu_{\bar{\nu}} h_{\mu\nu}. \quad (2.5)$$

We now expand the Christoffel symbols in terms of $h_{\mu\nu}$:

$$\begin{aligned} \Gamma^\nu_{\alpha\beta} &= \frac{1}{2} \eta^{\nu\mu} (\partial_\beta h_{\mu\alpha} + \partial_\alpha h_{\mu\beta} - \partial_\mu h_{\alpha\beta}) \\ &= \frac{1}{2} (\partial_\beta h^\nu_{\alpha} + \partial_\alpha h^\nu_{\beta} - \partial^\nu h_{\alpha\beta}) \end{aligned} \quad (2.6)$$

In linearized theory, the Riemann tensor is then given by:

$$\begin{aligned} R^\nu_{\alpha\beta\mu} &= \partial_\beta \Gamma^\nu_{\alpha\mu} - \partial_\mu \Gamma^\nu_{\alpha\beta} \\ &= \frac{1}{2} (\partial_\alpha \partial_\beta h^\nu_{\mu} + \partial_\mu \partial^\nu h_{\alpha\beta} - \partial_\beta \partial^\nu h_{\alpha\mu} - \partial_\mu \partial_\alpha h^\nu_{\beta}). \end{aligned} \quad (2.7)$$

We now construct the Ricci tensor by contracting first and third indices:

$$R_{\alpha\beta} = R^\mu_{\alpha\mu\beta} = \frac{1}{2} (\partial_\mu \partial_\beta h^\mu_{\alpha} + \partial^\mu \partial_\alpha h_{\beta\mu} - \square h_{\beta\alpha} - \partial_\alpha \partial_\beta h), \quad (2.8)$$

where $h = h^\alpha_{\alpha}$ is the trace of metric perturbation and $\square = \partial_\mu \partial^\mu = \nabla^2 - \partial_t^2$ is the d'Alembertian wave operator. We now compute curvature scalar by contracting again:

$$R = R^\alpha_{\alpha} = (\partial_\mu \partial^\alpha h^\mu_{\alpha} - \square h) \quad (2.9)$$

and then the Einstein tensor is given by:

$$\begin{aligned} G_{\alpha\beta} &= R_{\alpha\beta} - \frac{1}{2}\eta_{\alpha\beta}R \\ &= \frac{1}{2}(\partial_\mu\partial_\beta h^\mu{}_\alpha + \partial^\mu\partial_\alpha h_{\beta\mu} - \square h_{\alpha\beta} - \partial_\alpha\partial_\beta h - \eta_{\alpha\beta}\partial_\mu\partial^\nu h^\mu{}_\nu + \eta_{\alpha\beta}\square h) \end{aligned} \quad (2.10)$$

To clean up the above expression we change the notation. We define the ‘trace reverse’ of $h^{\mu\nu}$ as $\bar{h}^{\mu\nu}$.

$$\bar{h}^{\mu\nu} = h^{\mu\nu} - \frac{1}{2}\eta^{\alpha\beta}h. \quad (2.11)$$

Note that $\bar{h}^\alpha{}_\alpha = -h$, we replace $h_{\alpha\beta}$ with $(\bar{h}_{\alpha\beta} + \frac{1}{2}\eta_{\alpha\beta}h)$ in Eq. (2.10). Then the Einstein tensor, to first order, is:

$$G_{\alpha\beta} = \frac{1}{2}(\partial_\mu\partial^\mu\bar{h}_{\alpha\beta} + \eta_{\alpha\beta}\partial^\mu\partial^\nu\bar{h}_{\mu\nu} - \partial^\mu\partial_\beta\bar{h}_{\alpha\mu} - \partial^\mu\partial_\alpha\bar{h}_{\beta\mu} + O(h_{\alpha\beta}^2)). \quad (2.12)$$

To simplify the above Eq. (2.12) further, we exploit the gauge freedom, i.e., choose an appropriate coordinate system. We can write a general infinitesimal coordinate transformation as $x^{\alpha'} = x^\alpha + \xi^\alpha$, where $\xi^\alpha(x^\beta)$ is an arbitrary infinitesimal vector field. Then the metric perturbation changes as:

$$h'_{\alpha\beta} = h_{\alpha\beta} - 2\partial_\alpha\xi_\beta, \quad (2.13)$$

and the trace-reversed metric is:

$$\begin{aligned} \bar{h}'_{\alpha\beta} &= h'_{\alpha\beta} - \frac{1}{2}\eta_{\alpha\beta}h' \\ &= \bar{h}_{\alpha\beta} - 2\partial_\beta\xi_\alpha + \eta_{\alpha\beta}\partial^\mu\xi_\mu. \end{aligned} \quad (2.14)$$

The Lorenz gauge are suitable gauge choice, is given by the:

$$\partial_\nu\bar{h}^{\mu\nu} = 0. \quad (2.15)$$

We can compute ξ_α such that the Lorenz gauge can be imposed on the metric perturbation, i.e., we find a new metric $h'_{\alpha\beta}$ such that it satisfies the Lorenz gauge condition Eq. (2.15):

$$\begin{aligned} \partial^\alpha\bar{h}'_{\alpha\beta} &= \partial^\alpha\bar{h}_{\alpha\beta} - \partial^\alpha\partial_\beta\xi_\alpha - \square\xi_\beta + \partial_\beta\partial^\mu\xi_\mu \\ &= \partial^\alpha\bar{h}_{\alpha\beta} - \square\xi_\beta. \end{aligned} \quad (2.16)$$

Therefore, by imposing the Lorenz gauge, we force the infinitesimal coordinate transform to satisfy:

$$\square\xi_\beta = \partial^\alpha\bar{h}_{\alpha\beta}. \quad (2.17)$$

Thus, applying Eq. (2.15) to the Eq. (2.12) yields:

$$G_{\alpha\beta} = -\frac{1}{2}\square\bar{h}_{\alpha\beta}. \quad (2.18)$$

Rearranging, we arrive at the final form of the weak field Einstein equations under the Lorenz gauge condition:

$$\square\bar{h}_{\mu\nu} = -16\pi T_{\mu\nu}. \quad (2.19)$$

Solving Einstein's Field Equation

Let's consider the case far from the source and in vacuum ($T^{\mu\nu} = 0$), then the field Eq. (2.19) reduces to:

$$\square\bar{h}^{\mu\nu} = 0. \quad (2.20)$$

The solution of the above equation is a superposition of plane waves:

$$\bar{h}_{\mu\nu}(\mathbf{x}, t) = \Re \int d^3k A_{\mu\nu}(\mathbf{k}) e^{i(\mathbf{k}\cdot\mathbf{x} - \omega t)}, \quad (2.21)$$

where $A_{\mu\nu}$ is the polarization tensor which contains information about the amplitude and polarization and depends on the wavevector \mathbf{k} . $\omega = |\mathbf{k}|$ with $k^\mu = (\omega, \mathbf{k})$ and it can be shown [4] that $k^\nu k_\nu = 0$, i.e, k^ν is a null vector. k^μ the wave vector which provides propagation direction and frequency of the wave. Imposing the Lorenz gauge condition implies that $A^{\mu\nu} k_\nu = 0$, i.e, $A^{\mu\nu}$ is orthogonal to the direction of the wave propagation \vec{k} , thus the wave is a transverse plane wave. We can further impose a transverse traceless (TT) gauge condition while still satisfying Lorenz gauge condition for a globally vacuum spacetime to make the metric perturbation purely spatial:

$$h_{tt} = h_{ti} = 0 \quad (2.22)$$

and traceless:

$$h = h_i^i = 0. \quad (2.23)$$

Then the Lorenz gauge condition (2.15) implies:

$$\partial_i h_{ij} = 0. \quad (2.24)$$

This is called the transverse-traceless gauge. We write the metric perturbation in TT gauge as $h_{\alpha\beta}^{TT}$. As it is traceless, therefore:

$$\bar{h}_{\mu\nu}^{TT} = h_{\mu\nu}^{TT} \quad (2.25)$$

Imposing TT gauge conditions fixes all the local gauge freedom, thus, $h_{\alpha\beta}^{TT}$ contains only physical information about the radiation. The fact that the gravitational waves

have two polarization components can also be shown in TT gauge. For example, if we orient the coordinates such that the wave propagates in the z-direction then, a valid solution to the wave equation $\square h_{ij}^{TT} = 0$ is $h_{ij}^{TT} = h_{ij}^{TT}(t - z)$. Then applying Lorenz condition implies that the only non-zero components of the metric perturbation are h_{xx}^{TT} , h_{xy}^{TT} , h_{yx}^{TT} and h_{yy}^{TT} . The conditions given in Eqs. (2.22, 2.23), implies that only two of these components are independent. Therefore, in TT gauge, the only non-zero components of h_{ij}^{TT} are $h_{xx}^{TT} = -h_{yy}^{TT}$ and $h_{xy}^{TT} = h_{yx}^{TT}$, i.e.,

$$h_{\mu\nu}^{TT}(t, z) = \begin{pmatrix} 0 & 0 & 0 & 0 \\ 0 & h_+(t-z) & h_\times(t-z) & 0 \\ 0 & h_\times(t-z) & -h_+(t-z) & 0 \\ 0 & 0 & 0 & 0 \end{pmatrix}, \quad (2.26)$$

where $h_+(t-z)$ and $h_\times(t-z)$ are the ‘plus’ and ‘cross’ polarizations of the gravitational waveform. Since we have exploited all our gauge freedom, these two polarizations are physically observable phenomena. To find out how the GWs are generated by the source, one needs to solve the Einstein equation coupled with matter (2.19) and with the conservation equation, $\partial^\mu T_{\mu\nu} = 0$. The Green’s function associated with the wave operator is well known. One can show that by using retarded Green’s function, Eq. (2.19) reduces to:

$$\bar{h}_{\mu\nu}(t, x) = 4 \int d^3x' \frac{T_{\mu\nu}(t - |\vec{x} - \vec{x}'|, \vec{x}')}{|\vec{x} - \vec{x}'|}, \quad (2.27)$$

where x is spatial coordinate of the field point at which $\bar{h}_{\mu\nu}$ is determined, x' is spatial coordinate of a point of the source and $t - |\vec{x} - \vec{x}'|$ is the retarded time where speed of light is set to unity ($c = 1$). It accounts for the lag between the propagation of information from position x to x' . We only require the spatial components of the metric perturbation as they only contain the radiative degrees of freedom. We compute Eq. (2.27) at large distances from the source and therefore we can pull $r \equiv |\vec{x} - \vec{x}'|$ out of the integral:

$$\bar{h}_{ij}(t, x) = \frac{4}{r} \int d^3x' T_{ij}(t - r, \vec{x}'). \quad (2.28)$$

The above equation is the leading-order term in the multipolar expansion of the radiation field. Using the stress-energy conservation $\partial_\alpha T^{\alpha\beta} = 0$ and after massaging the above equation a bit, it can be shown that:

$$\frac{4}{r} \int d^3x' T_{ij} = \frac{2}{r} \frac{\partial^2}{\partial t^2} \int d^3x' \rho x^i x^j, \quad (2.29)$$

where ρ is the mass density T^{tt} , in a volume element d^3x at the position x^i . We can define the third moment I_{ij} of the mass distribution as:

$$I_{ij}(t) = \int \rho(t, x) x^i x^j d^3x. \quad (2.30)$$

Combining Eq. (2.28) and (2.29) gives:

$$h_{ij}(t, x) = \frac{2}{r} \ddot{I}_{ij}(t - r). \quad (2.31)$$

The final quadrupole formula is obtained by projecting the above equation into TT gauge:

$$h_{ij}^{TT}(t, x) = \frac{2}{r} \frac{d^2 \mathcal{I}_{kl}(t - r)}{dt^2} P_{ik}(n) P_{jl}(n). \quad (2.32)$$

Here P_{ij} is the projection operator and the quadrupole moment tensor \mathcal{I}_{ij} is obtained by subtracting the trace from I_{ij} :

$$\mathcal{I}_{ij} = I_{ij} - \frac{1}{3} \delta_{ij} I, \quad I = I_{ii}. \quad (2.33)$$

2.2 Sources of gravitational waves: Binary Neutron Stars

The quadrupole formula (2.32) shows that any matter that can produce time-varying quadrupole moment can produce GWs. However, to detect the GWs from terrestrial interferometers like LIGO/Virgo [15, 16], the amplitude of the waves need to be large enough. Therefore, events which involve compact and heavy objects, such as BHs and NSs, moving at relativistic speed are more detectable. Approximately, two years after the first detection of GWs from two merging BHs, the first GW signal consistent with a BNS merger was observed [Collab1]. GW170817 was observed at the luminosity distance of only 40_{-14}^{+8} Mpc from Earth with a combined signal-to-noise ratio (SNR) of 32.4 [Collab1], which makes it the closest and loudest event yet. We focus mainly on the BNS mergers as a source of GWs in this thesis. The emitted GWs from the coalescence of a BNS is a chirp-like signal and characterized by increasing amplitude and frequency, similar to the case of a BBH coalescence. The gravitational-wave spectrum from a BNS merger can be characterized into three regimes: inspiral, merger and post-merger. Fig. 2.1 shows an NR- gravitational waveform as well as the associated $M\omega_{22}$ as a function of mass rescaled retarded time for the three regimes. The corresponding snapshots of the rest-mass density $\log_{10}\rho$ for three different regimes are shown in the bottom panel. We now discuss the three regimes in detail.

(i) **Inspiral phase** - As the two NSs orbit and slowly inspiral, they emit GW and come closer and closer. Each star becomes tidally deformed by the gravitational field of its companion. This effect leads to an increase in the inspiral rate [19] and adds tidal

information to the GW [20–22]. The deformability of the NS can be characterized in terms of its Love number. Let \mathcal{E}_{ij} is the quadrupolar tidal field generated by the external gravitational potential, then the induced quadrupole, to linear order:

$$Q_{ij}(t) = -\lambda \mathcal{E}_{ij}(t), \quad \lambda = \text{constant}. \quad (2.34)$$

For ($l = 2$) the dimensionless Love number k_2 is defined as

$$k_2 = \frac{3 G \lambda}{2 R^5}, \quad (2.35)$$

where R is the radius of a NS. The magnitude of the tidal interaction is regulated by a set of tidal deformability coefficients

$$\Lambda_\ell^{A,B} = \frac{2k_\ell^{A,B}}{C_{A,B}^{2\ell+1}(2\ell-1)!!}, \quad (2.36)$$

where A, B label the two NSs, and $k_\ell^{A,B}$ and $C_{A,B} = M_{A,B}/R_{A,B}$ denote their Love numbers and compactnesses [22–24]. Since $\Lambda_\ell^{A,B}$ depend on the internal structure of the NSs, their measurement provides constraints on the EOS of cold degenerate matter at supranuclear densities. The tidal deformabilities of the individual stars $\Lambda_2^{A,B}$ are difficult to measure, but the combination

$$\tilde{\Lambda} = \frac{16 (M_A + 12M_B) M_A^4 \Lambda_2^A}{13 (M_A + M_B)^5} + [A \leftrightarrow B]. \quad (2.37)$$

can be extracted from the detected GW signal with significantly higher precision [25, 26]. The gravitational waveform in the frequency domain can be written as:

$$\tilde{h}(f) = A(f) \exp^{-i\Psi(f)}, \quad (2.38)$$

where A is the amplitude, f is frequency and Ψ is the phase of the GW. The tidal interactions (for non-spinning binaries) enter the phase evolution at the 5 PN order [20, 21, 27–32], then the leading-order phase correction due to tides is given by:

$$\Delta\Psi_{5PN}^{tidal} = \frac{-111}{256} \frac{M^2}{M_A M_B} \tilde{\Lambda} \left(\frac{v}{c}\right)^5 \quad (2.39)$$

where M is the total mass of the binary. $\tilde{\Lambda}$ captures the entire 5 PN tidal correction; it also enters at 6 PN order in linear combination with

$$\begin{aligned} \delta\tilde{\Lambda} = & \left(M_A^2 - \frac{7996}{1319} M_A M_B - \frac{11005}{1319} M_B^2 \right) \frac{M_A^4 \Lambda_2^A}{(M_A + M_B)^6} \\ & - [A \leftrightarrow B], \end{aligned} \quad (2.40)$$

which, however, is unlikely to be measured by Advanced LIGO/Virgo detectors [26]. The imprint of tidal interaction on the GW phase is visible at low GW frequencies $\lesssim 150$ Hz, e.g. [20, 33].

(ii) **Merger Phase** - After a long inspiral, the two NS plunge into each other and form a single object. We use NR to investigate the merger and post-merger dynamics of a BNS coalescence. Studies of numerical simulations of BNS mergers predict that depending on the initial masses and EOS of the two NSs; the remnant could be either a hypermassive neutron star (HMNS), a supermassive neutron star or a BH [34]. If the total mass of the remnant is greater than twice of the total mass of a Tolman-Oppenheimer-Volkhov star (M_{TOV}), $M \geq 2M_{TOV}$, then the merger leads to a prompt collapse to a BH. However, if $M \sim 1.5M_{TOV}$ then a HMNS formation is more likely. Hypermassive neutron stars are massive ($M \sim 2M_{\odot}$), and have a large angular momentum, and are stabilized by differential rotation. They shed off the extra angular momentum through GW emission. For the given mass, if the EOS of the remnant, allows a stable non-rotating counterpart then it will stabilize to supermassive neutron star; otherwise, it will lead to a delayed collapse to a BH [34].

(iii) **Postmerger Phase** - the spectrum of this phase depends on the remnant. In general, the merger remnant has a characteristic GW spectrum with a small number of broad peaks in the $f_{GW} \sim 1.8 - 4$ kHz frequency range. The main peak frequencies of the post-merger GW spectrum correlate with properties of a zero-temperature spherical equilibrium star [35, 36] following EOS-independent quasi-universal relations [35–44]. While measuring the post-merger GW signal would, in principle, allow one to determine the EOS independently of the inspiral signal.

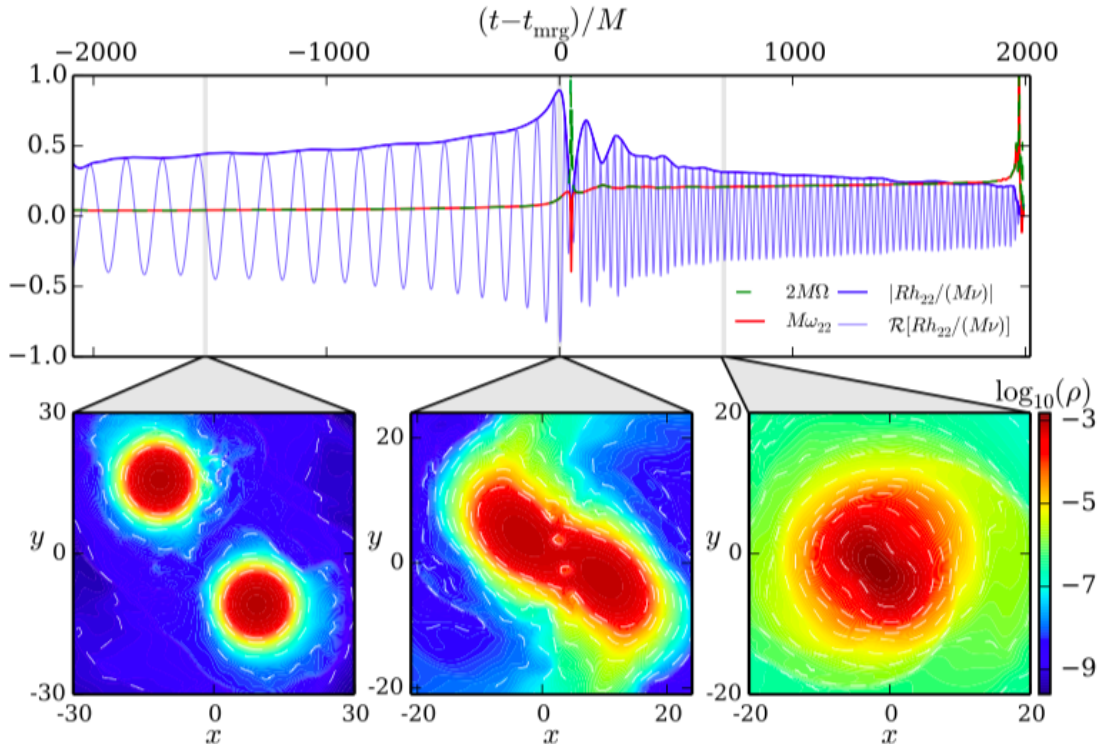


Figure 2.1: Top panel: Real part of the NR waveform $\mathcal{R}h_{22}/(\nu M)$ for BNS merger of an equal mass non-spinning system with mass $M_A = M_B = 1.35M_\odot$ and EOS H4, and associated dimensionless GW frequency $M\omega_{22}$ as function of total mass rescaled retarded time t/M . Bottom: the snapshots of the logarithmic of the rest-mass density $\log_{10}\rho$ for the inspiral, merger and postmerger regimes. The waveform is shifted such that merger time $t_{\text{mrg}} = 0$. The plot is taken from [42].

2.3 Bayesian Inference

We extract the properties of the detected GW signal by employing the LIGO/Virgo parameter estimation algorithm LALInference [45, 46], which is included into the LSC algorithm library (LALSuite) package. The algorithm relies on Bayesian inference that compares the observed signal against theoretical models [45, 47]. The analysis of a GW signal is divided into two parts. The first is to constrain or measure parameters of the source such as masses, spins, EOS of the NS, and sky location. For a given fixed model, this is known as *parameter estimation*. Another is to understand which model is more favorable among different models in the presence of the data, which refers to as *model selection*. Both of these problems are tackled by Bayesian analysis in GW astronomy.

A signal model for GWs from a compact binary is described by two sets of parameters, intrinsic and extrinsic. The *intrinsic* parameters are those which describe components of the system like individual masses of the binary M_A and M_B , mass ratio $q = M_B/M_A \leq 1$ ¹ The best-measured parameter from a GW signal is the chirp mass $\mathcal{M} = (M_A M_B)^{3/5}/(M_A + M_B)^{1/5}$. It enters the phase evolution at the lowest order.

¹Or $Q = M_A/M_B \geq 1$ is also used.

The spin angular momenta S_i , (i runs from A, B), represents six additional parameters. Usually, dimensionless spin parameter $\chi_i = S_i/(M_i)^2$ where ($G = c = 1$), is employed. For BNS systems, the dimensionless tidal parameter Λ_i [Eq. (2.37)] and $\delta\tilde{\Lambda}_i$ are additional intrinsic parameters whose measurement helps in constraining EOS of the NSs. The *extrinsic* parameters are those which determine the localization and orientation of the binary such as sky location (Θ, Φ) , luminosity distance (D_L), polarization angle (ψ), orbital inclination of the binary (θ), time and phase of coalescence (t_c, ϕ_c) , and the inclination angle $\cos\theta_{JN} = \hat{\mathbf{J}} \cdot \hat{\mathbf{N}}$, where $\hat{\mathbf{J}}$ is the unit vector in the direction of the total angular momentum and $\hat{\mathbf{N}}$ is the unit vector in the direction from the source towards the observer.

In this section, we provide a brief overview of the Bayesian analysis techniques in the context of GW astronomy. For a more thorough discussion, we refer the reader to [45, 47] and references therein. We begin with Bayes' theorem:

$$p(\boldsymbol{\theta}|d) = \frac{p(d|\boldsymbol{\theta})p(\boldsymbol{\theta})}{p(d)}, \quad (2.41)$$

where $p(\cdot)$ is the probability density and $p(\cdot|\cdot)$ is the conditional probability density. The term $p(\boldsymbol{\theta}|d)$, on the left hand side (LHS), is the *posterior* probability density function (PDF) (or simply posterior) for the model parameters $\boldsymbol{\theta}$ given the data d . This quantity is what we attempt to construct using Bayesian analysis. $p(d|\boldsymbol{\theta})$ is called the *likelihood* which describes how well our model fits the data. $p(\boldsymbol{\theta})$ is known as the *prior* PDF (or just prior) on the parameters. The denominator is known as the *evidence*, given by:

$$p(d) = \int p(d|\boldsymbol{\theta})p(\boldsymbol{\theta})d\boldsymbol{\theta}. \quad (2.42)$$

Likelihood is the probability of obtaining the data d given the parameter $\boldsymbol{\theta}$ for a given signal and noise model of the detector. Usually we assume detector noise to be Gaussian, i.e., the noise values follow Gaussian distribution. Then, the time series of detector data, $d(t)$, can be modeled as the sum of the true GW signal and detector noise, denoted by $h(t)$ and $n(t)$, respectively:

$$d(t) = h(t) + n(t). \quad (2.43)$$

For Gaussian noise, the likelihood for a single detector is given by [48]

$$p(d(t)|\boldsymbol{\theta}) \propto \exp \left[-2 \int_0^\infty \frac{|\tilde{d}(f) - \tilde{h}(f, \boldsymbol{\theta})|^2}{S_{\text{det}}(f)} df \right], \quad (2.44)$$

where tildes denote Fourier transforms of time series introduced so far and $S_{\text{det}}(f)$ is the one sided power spectral density (PSD) of the detector. Under the assumption that noise in different detectors is not correlated, this expression is readily gener-

alized to the case of a coherent network of detectors by taking the product of the likelihoods in each detector [49]. The prior incorporates our state of knowledge about the parameters θ before we carry out a measurement. E.g., for a BNS event, it is logical to choose a uniform mass prior in the range $(1 - 3)M_\odot$ as we know from the literature and observations that a NS cannot be heavier than $3M_\odot$ (Chandrasekhar limit). If we are ignorant about a parameter then we can choose a uniform or log uniform prior. Here in the context of GW data analysis, the model parameters θ represents the intrinsic and extrinsic parameters of the two compact objects that define our model. At times, we are interested in only one of these parameters, therefore, for a specific subset of source parameters in the set θ may be obtained by marginalising the full posterior over all but those parameters:

$$p(\theta_i|d) = \int \left(\prod_{k \neq i} d\theta_k \right) p(\theta|d). \quad (2.45)$$

It can be shown that Eq. (2.44) reduces to

$$p(d|\theta) \propto \exp \left[-\frac{1}{2} ((d, d) + (h(\theta), h(\theta)) - 2(d, h(\theta))) \right], \quad (2.46)$$

where (a, b) is the noise weighted inner product². The optimal SNR is defined as

$$\rho_{opt}^2 = (h, h) = 4 \int_0^\infty \frac{|\tilde{h}(f)|^2}{S_{det}(f)} df. \quad (2.47)$$

Let's assume that we have two competing hypothesis (or models), one is that a GW signal is present in the data, i.e, a signal model and the other is no signal is present, i.e, noise model. The ratio of two probabilities of obtaining the data d given one model versus another is called a Bayes' factor:

$$\mathcal{B} = \frac{p(d|\mathcal{H}_1)}{p(d|\mathcal{H}_0)}, \quad (2.48)$$

where \mathcal{H}_1 is the hypothesis that there is signal in the data and \mathcal{H}_0 is the null hypothesis. This is the ratio of Bayesian evidences. Evidence is independent of the parameters θ and hence for a given dataset is just a constant. It can be viewed as a completely marginalised likelihood function and used for model selection. Here, each hypothesis is defined by a set of fixed (known) parameters. Then using Eq. (2.46)

$$\Lambda = \exp \left[-\frac{1}{2} ((h(\theta), h(\theta)) - 2(d, h(\theta))) \right], \quad (2.49)$$

²The noise weighted inner product is defined as: $(a, b) = 4\Re \int_0^\infty \frac{\tilde{a}(f)\tilde{b}^*(f)}{S_{det}(f)}$.

where we have renamed the Bayes' factor as the likelihood ratio Λ . Note that any variation in Λ depends only on $(d, h(\boldsymbol{\theta}))$; therefore, it can be recognised as an optimal statistic. Any threshold to reject the hypothesis can be translated to this quantity. This quantity is also called matched filter as it is a noise weighted inner product of the expected signal with the data. Model selection tells us which model is statistically preferred by the data and by how much. When the absolute value of Λ is large we say that the data preferred one model over other. Formally, to compare two models (M_a and M_b), we define odds ratio $\mathcal{O}_{a,b}$ as:

$$\mathcal{O}_{a,b} = \frac{p(d|M_a) p(M_a)}{p(d|M_b) p(M_b)}. \quad (2.50)$$

This quantity is, in fact, the multiplication of Bayes' factor with a quantity we call prior odds. Prior odds encapsulates our prior belief about the models before we carry out the measurement. Prior odds helps penalize the complicated models. To compute posteriors or evidence, one needs to sample the N-dimensional parameter space, which is computationally infeasible. Markov-Chain-Monte-Carlo (MCMC) [50] and nested sampling are the two categories of sampling algorithms that are widely used. MCMC generates samples from a target distribution via a form of random walk jumping from one possible location to the next following a set of probabilistic rules. This algorithm is based on the Metropolis Hasting algorithm [51, 52]. While nested sampling is designed to calculate evidence. The generation of the posterior distribution is its by-product. It populates the parameter space with some points drawn from the prior distribution, then the point of minimum likelihood is removed, and iterates the algorithm until the point of higher likelihood is found. Typically, $10^6 - 10^7$ waveforms are evaluated by sampler to compute the posteriors. Both of these algorithms are included in the LALInference package [45] as part of the LALSuite [46]. Then, for analysis, the standard approach is to construct 1D or 2D marginalized posteriors and compute the mean, median, and mode of the posteriors. We often compute credible intervals which enclose desired integrated probability, say (90%, 95%).

2.4 GW170817 event

The rate and population models of the compact binaries have predicted that the detection rate of BNS would be one to hundreds per year, when the detector network reaches its design sensitivity [53, 54]. *O1* ran for about three months and delivered GWs from three BBH mergers. During *O2*, the first BNS merger was detected along with seven BBH coalescences. So far, LIGO/Virgo collaboration (LVC) has published detection of 10 BBH mergers and 1 BNS mergers [55]. The merger rate prediction for BNS inferred from *O1-O2* data, at 90% confidence level are $110 - 3840 \text{ Gpc}^{-3}\text{y}^{-1}$, $9.7 - 101 \text{ Gpc}^{-3}\text{y}^{-1}$ respectively [55]. The first BNS detection, GW170817, has pro-

vided unique opportunities to not only probe/test GR in the strong field regime. A gamma-ray burst was observed 1.7 seconds after the merger time by Fermi and INTEGRAL gamma-ray telescope [7, 56]. Later, a followup localized a counterpart near the galaxy NGC 4993, whose sky location and distance were consistent with what was inferred from the GW data. All three detectors were operating at the time of the event, which led to a source localization within an area of 28 deg^2 .

In the discovery paper [Collab1], TaylorF2_{Tides} model was used to estimate the properties of the source. This model is described in Chapter 3. Though, there is a degeneracy between the inclination angle $\cos \theta_{JN} = \hat{\mathbf{J}} \cdot \hat{\mathbf{N}}$ and distance measurements in GW measurements, since the luminosity distance is known independent of the GW data, this degeneracy can be broken. The data is found to be consistent with an anti-aligned source: $\cos \theta_{JN} \leq -0.54$, and the viewing angle $\Theta \equiv \min(\theta_{JN}, 180 \text{ deg} - \theta_{JN})$ is $\Theta \leq 56 \text{ deg}$. $\cos \theta_{JN}$ and Θ are constrained to $\cos \theta_{JN} \leq -0.88$ and $\Theta \leq 28 \text{ deg}$ using estimated redshift to NGC 4993 depending on the assumption for the Hubble flow velocity [Collab1]. For GW170817, the chirp mass is $\mathcal{M} = 1.188_{-0.002}^{+0.004}$ with the total mass in the range $[2.73 - 3.29] M_{\odot}$. The mass parameters in the detector frame are related to the rest-frame masses of the source by via redshift z as $m^{det} = m(1+z)$. The uncertainty in the chirp mass measurement in source frame is dominated by uncertainty in the luminosity distance. Therefore, the errors in the \mathcal{M} in source frame are $O(10)$ larger than in detector frame $\mathcal{M}^{det} = 1.1977_{-0.0003}^{+0.0008}$. The chirp mass \mathcal{M} enters at the lowest order in the phase evolution, thus for a long inspiral signal like GW170817, it is very well constrained. However, the measurement of component masses are affected by the degeneracy between q and spin components χ_A and χ_B ³. How this degeneracy could bias the measurements of q , component masses M_A and M_B , and spins is studied in the parameter estimation study [Dudi1] discussed in Chapter 4. Here, the assumption for spin prior is $|\chi_{\text{eff}}| \leq 0.89$ ⁴ (as for BHs $|\chi_{\text{eff}}| < 1$). Some studies with realistic NS EOS give the limit $\chi_{\text{eff}} < 0.7$ [57] though some EOS can exceed this bound. Therefore, an isotropic prior on the spin direction with $|\chi_{\text{eff}}| \leq 0.89$ has been assumed. We recover $q \in (0.4, 1.0)$ and $\chi_{\text{eff}} \in (-0.01, 0.17)$. We obtain the range of component masses $M_A \in (1.36, 2.26)M_{\odot}$ and $M_B \in (0.86, 1.36)M_{\odot}$. These values are consistent with the range of known NS masses and below those of known BHs. Given the spins of known NS, one can advocate that the high spin prior $|\chi| \leq 0.89$ is not astrophysically relevant. Therefore, a low spin prior $|\chi| \leq 0.05$ is also imposed, which gives $q \in (0.7, 1.0)$ and $M_A \in (1.36, 1.60)M_{\odot}$ and $M_B \in (1.17, 1.36)M_{\odot}$ and $\chi_{\text{eff}} \in (-0.01, 0.02)$. The range of the estimated masses are consistent with the previously observed BNS system in our galaxy. Additionally, the observation of electromagnetic counterpart indicate the presence of matter, therefore, GW170817 could be a BNS merger event. However,

³The dimensionless spin magnitude $\chi_i = S_i/M_i^2$ (i runs over A and B)

⁴ $\chi_{\text{eff}} = \frac{M_A \chi_A + M_B \chi_B}{M_A + M_B}$

more compact objects like quark stars or NS-BH binary, cannot be completely ruled out. With this event, the GW community had a chance to constrain the EOS of the NS matter for the first time. Here, Λ_ℓ^A and Λ_ℓ^B are allowed to vary independently. Meaning that the constraint that all NS should have the same EOS is not imposed. Though, in a later publication [12] where the constraints on the radii of NSs is studied, this constraint is imposed. Assuming a uniform prior for $\tilde{\Lambda}$, with the high spin prior, they obtained the upper limit on $\tilde{\Lambda} \leq 700$ and imposing low spin prior gave $\tilde{\Lambda} \leq 800$. They found that the upper limits on $\tilde{\Lambda}$ ruled out those EOS that predicts less compact stars.

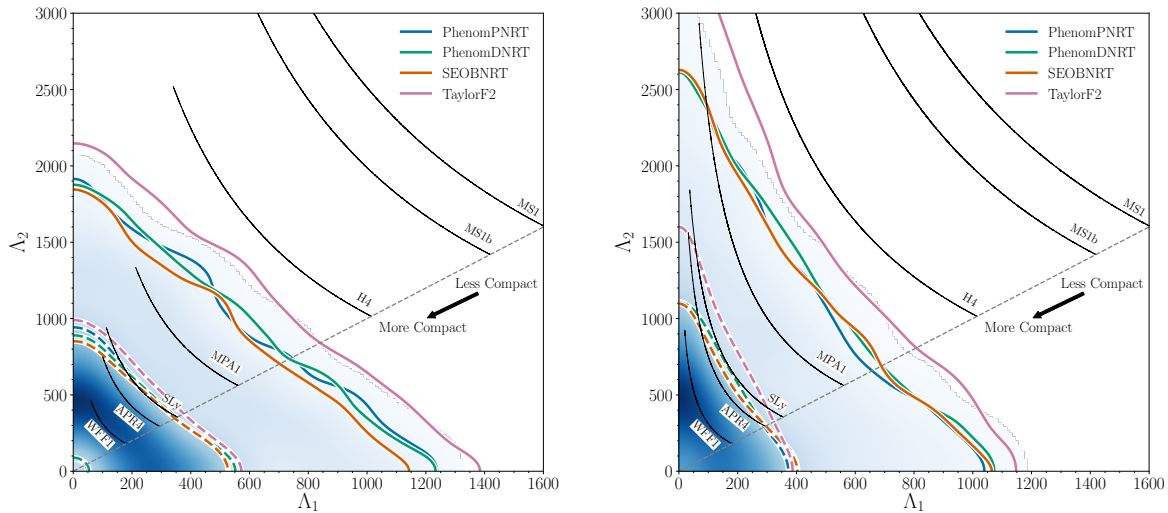


Figure 2.2: PDFs for the individual tidal deformability $\tilde{\Lambda}_2^A$ (Λ_1 in plot) and $\tilde{\Lambda}_2^B$ (Λ_2 in plot) using the high-spin (left panel) and low-spin (right panel) priors. The blue shading is the PDF for the precessing waveform IMRPhenomPv2_NRTidal. The 50% (dashed lines) and 90% (solid lines) credible regions are shown for the four waveform models. The seven black curves are the tidal parameters for the seven representative EOS models using the masses estimated with the IMRPhenomPv2_NRTidal model, ending at the $\tilde{\Lambda}^A = \tilde{\Lambda}^B$ boundary. The plot is taken from [58].

Later, studies analyzed the GWs data in more detail [Collab2], which improved the estimates of the binary's properties and led to improved results: (i) Instead of 30 Hz, the GW frequency starting from 23 Hz is considered, which gives an additional 1500 cycles. (ii) The recalibrated data from Virgo detector is used. (iii) The known source distance from the electromagnetic observations is used. Several electromagnetic signals covering the entire spectrum, ultraviolet, optical, infrared, and gamma, were observed by multiple instruments. As already predicted, the merger of NS produces a kilonova due to the synthesis of a large amount of heavy element via rapid neutron capture r-process in the ejecta [59]. The electromagnetic signatures are consistent with these predictions and confirm BNS mergers as the sites where heavy elements like gold and platinum forms [13] and BNS as a progenitor of the gamma-ray burst. The source properties are estimated by employing the

Bayesian inference method, as described in Sec. 2.3. Markov-chain Monte Carlo (MCMC) algorithm, implemented in LALInference package in LALSuite library, is used for stochastic sampling to compute the marginalized posteriors. For the analysis of the signal, multiple waveform models that are more accurate and have more physical effects are employed. The waveform models used for parameter extraction are `TaylorF2Tides`, `IMRPhenomD_NRTidal`, `SEOBNRv4_ROM_NRTidal`, and `IMRPhenomPv2_NRTidal`. We discuss all these waveform models in detail in Chapter 3. `IMRPhenomPv2_NRTidal` is the only model that incorporates tides, precession, and as well as spin-induced quadrupole effects that enter the phasing at 2 PN order. A uniform prior in detector frame masses with the constraint that $0.5M_{\odot} < M_A^{det}, M_B^{det} \leq 7.7M_{\odot}$ and an additional constraint on chirp mass $1.184 \leq \mathcal{M}^{det} \leq 2.168M_{\odot}$ are employed. They convert the detector frame to source frame quantities by estimating the redshift z using MUSE_VLT measurement of the redshift of the NGC 4993. Again, two different spin priors on the magnitude of the dimensionless spin, the high spin prior $\chi_{\text{eff}} \leq 0.89$ and low spin prior $\chi_{\text{eff}} \leq 0.05$ are employed. The high spin prior is chosen to be consistent with the initial analysis [Collab1], and to allow the possibility of an exotic binary system. The low spin prior choice is motivated by the fact that the fastest spinning BNS capable of merging within Hubble time will have at most $\chi_{\text{eff}} \leq 0.05$ when they merger. A uniform prior for tidal deformability in the range $0 \leq \Lambda_2^i \leq 5000$ is employed. Tab. 2.1 shows the median value with 90% credible bounds on the binary's parameter for both high spin (right column) and low spin prior (middle column). These values are inferred by employing `IMRPhenomD_NRTidal` model, though consistent results are obtained for other models as well, for details see the Appendix A of Ref. [Collab2]. We show marginalised PDFs of the individual tidal deformability Λ^A and Λ^B in Fig. 2.2 using high spin prior (right column) and low spin prior (left column) for the four waveform models employed. Note that the bounds of all three `NRTidal` models are in agreement with each other and 20-30% smaller than `TaylorF2Tides`. Although the results of `TaylorF2Tides` model is in agreement with [Collab1] but with using lower starting frequency and better data the bounds on $\Lambda_2^{A,B}$ is decreased 10-20% with respect to Ref. [Collab1]. This is because of a degeneracy between mass, spin and tidal parameters, thus other parameters are constrained well with longer inspiral, which helps in improving constraints on tidal parameters. A subset of piecewise-polytropic EOS, constructed using the mass posteriors are also shown. EOS which are more stiff such as H4, MS1b and MS1 are ruled out. In Fig. 2.3 the PDFs for the combination of individual tidal deformability $\tilde{\Lambda}$ [Eq. (2.37)] reweighted by the priors are shown, again for the four models and using high-spin (top panel) and low-spin prior (bottom panel). The gray PDFs are given by the same EOS as in Fig. 2.2 and using masses that are sampled from posteriors.

Parameters	Low-spin prior ($\chi \leq 0.05$)	High-spin prior ($\chi \leq 0.89$)
θ_{JN}	$146_{-27}^{+25} \text{deg}^2$	$152_{-27}^{+21} \text{deg}^2$
θ_{JN_2}	$151_{-11}^{+15} \text{deg}^2$	$153_{-11}^{+15} \text{deg}^2$
\mathcal{M}^{det}	$1.1975_{-0.0001}^{+0.0001} M_{\odot}$	$1.1976_{-0.0002}^{+0.0004} M_{\odot}$
\mathcal{M}	$1.186_{-0.001}^{+0.001} M_{\odot}$	$1.186_{-0.001}^{+0.001} M_{\odot}$
M_A	(1.36, 1.60) M_{\odot}	(1.36, 1.89) M_{\odot}
M_B	(1.16, 1.36) M_{\odot}	(1.00, 1.36) M_{\odot}
M	$2.73_{-0.01}^{+0.04} M_{\odot}$	$2.77_{-0.05}^{+0.22} M_{\odot}$
q	(0.73, 1.00)	(0.53, 1.00)
χ_{eff}	$0.0_{-0.01}^{+0.02}$	$0.02_{-0.02}^{+0.08}$
χ_A	(0.00, 0.04)	(0.00, 0.50)
χ_B	(0.00, 0.04)	(0.00, 0.61)
$\tilde{\Lambda}$	300_{-190}^{+500} (symm) / 300_{-230}^{+420} (HPD)	(0, 630)

Table 2.1: We list the properties of GW170817 such as binary inclination θ_{JN} and θ_{JN_2} using EM distance constraint, detector frame chirp mass \mathcal{M}^{det} , chirp mass \mathcal{M} , primary mass M_A , secondary mass M_B , total mass M , mass ratio q , effective spin χ_{eff} , primary dimensionless spin χ_A , secondary dimensionless spin χ_B and tidal deformability $\tilde{\Lambda}$ inferred using the IMRPhenomPv2_NRTidal waveform model. All properties are source properties except for the detector frame chirp mass $\mathcal{M}^{\text{det}} = \mathcal{M}(1+z)$. Errors quoted as x_{-y}^{+z} represent the median, 5% lower limit, and 95% upper limit. Errors quoted as (x, y) are one-sided 90% lower or upper limits, and are used when one side is bounded by a prior. For the masses, M_A is bounded from below and M_B is bounded from above by the equal mass line. The mass ratio is bounded by $q \leq 1$. For the tidal parameter $\tilde{\Lambda}$, we quote results using a constant (flat) prior in $\tilde{\Lambda}$. In the high-spin case, we quote a 90% upper limit for $\tilde{\Lambda}$, while in the low-spin case we report both the symmetric 90% credible interval (symm) and the 90% highest posterior density (HPD) interval, which is the smallest interval that contains 90% of the probability. The table is taken from [58].

The bimodal behavior of NRTidal models could be related to noise realization and requires further investigation. In summary, these results are broadly consistent with the initial estimates. With improvements like longer and recalibrated data, known luminosity distance, and sophisticated waveform models, the results are more precise. The sky localization, which was 28 deg^2 , is improved to 16 deg^2 . We find better constraints on the inclination angle by employing known luminosity distance using electromagnetic observation. We provide tighter constraints on binary properties than the initial analysis and found masses to be in the range expected for the BNS system.

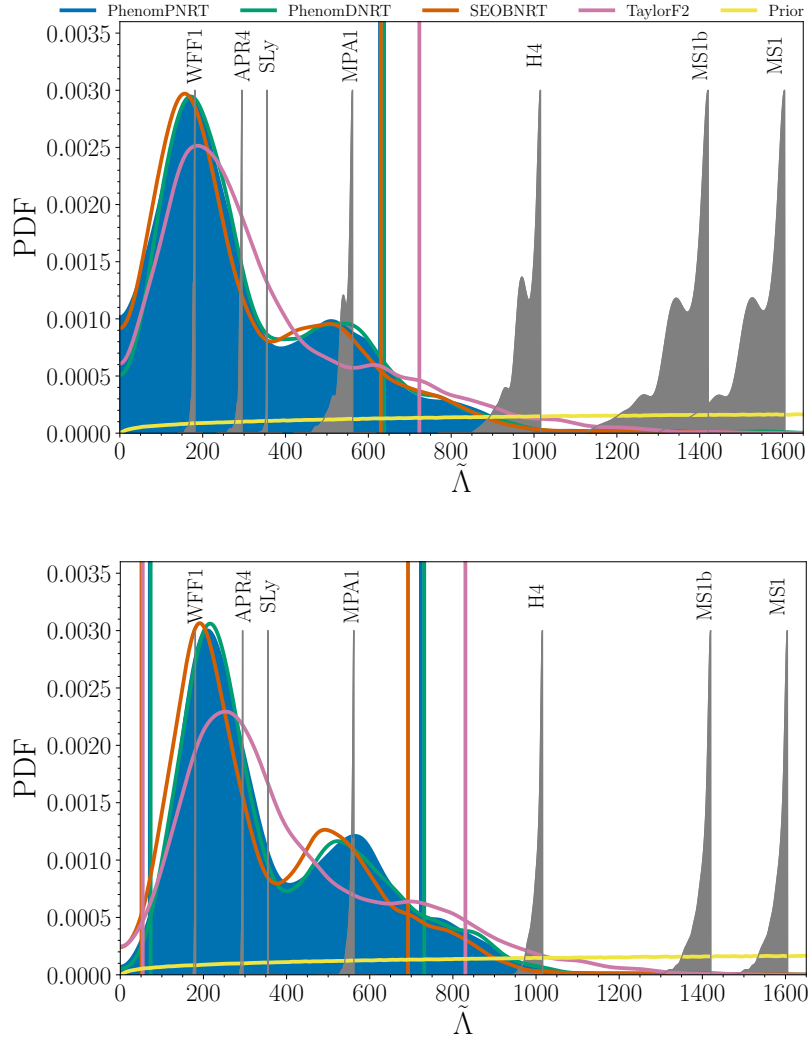


Figure 2.3: PDFs of the combined tidal parameter $\tilde{\Lambda}$ for the high-spin (top panel) and low-spin (bottom panel) priors. The PDFs have been reweighted by dividing by the original prior. The 90% HPD credible intervals are represented by vertical lines for each of the four waveform models: TaylorF2_{Tides}, IMRPhenomD_NRTidal, SEOBNRv4_ROM_NRTidal, and IMRPhenomPv2_NRTidal. For the high-spin prior, the lower limit on the credible interval is $\tilde{\Lambda} = 0$. The seven gray PDFs are those for the seven representative EOSs using the masses estimated with the IMRPhenomPv2_NRTidal model. Their normalization constants have been rescaled to fit in the figure. The plot is taken from [58].

Chapter 3

Waveform models

There are different techniques to model the GWs signals emitted from a compact binary coalescence. These models differ in their computational complexity, the physics they employ, and their regime of applicability. LALInference has been designed to interface with arbitrary waveform families efficiently. Each waveform family can be thought of as a function that takes as input a parameter vector (θ) and produces h_+ and h_\times in time or frequency domain. In this chapter, we discuss the analytical PN family, the EOB formalism, and phenomenological waveform models, including the NRTidal model. For modeling the signal a few cycles before the merger, at merger and post-merger part, NR simulations are employed, which we discuss in Chapter 7.

3.1 Post-Newtonian waveforms

It is tedious to solve Einstein's field equation in full generality even for the two-body problem. Thus approximate methods like PN, post-Minkowskian (non-linear expansion in G), multipole expansion are developed, which give results in good agreement with GR as higher orders included. These approximation methods are valid for sources that are slow-moving ($v \ll c$, v is the typical speed of the system), weakly self-gravitating, and weakly stressed. For the case of compact objects orbiting each other, one can divide the spatial region into two regimes: the *near zone* ($R \ll \lambda$, where R is the distance to the source and λ is the characteristic wavelength) and the *far zone* ($R \gg \lambda$). The fields in the near zone can be approximated to be instantaneous; thus, PN expansion in $(1/c^2 \sim GM/c^2R \implies v^2/c^2 \sim GM/c^2R)$ is employed around the instantaneous time (t) whereas in the far zone the effect of retardation needs to be included. Thus, a multipole expansion with different moments described by PN expansion around retarded time ($t - R/c$) is employed. The two expansions are matched together in the intermediate zone.

As the two objects inspiral each other, the orbit shrinks due to the emission of GWs.

The global conservation of energy leads to the energy balance equation:

$$\frac{dE}{dt} = -\mathcal{F}, \quad (3.1)$$

where E is the binding energy and \mathcal{F} denotes the total gravitational-wave “luminosity” and can be calculated from the quadrupole moment, as described in [60]. E can be deduced from high-order PN equations of motion of the binary. Landau Lifshitz representation of Einstein field equations in harmonic coordinates [60] and ADM-Hamiltonian formalism [61] are often used to study the dynamics of the binary system, and GWs and both methods give consistent results for the observables. The key elements of PN theory are equations of motion, energy and angular momentum fluxes, and gravitational waveforms. In the first-order approximation (0 PN), we get the Newtonian field, and by schematically iterating, higher orders are obtained. For a detailed description of the scheme of constructing equations of motion and wave generation formalism in high PN order, we refer to [60, 62]. As we include the higher-order terms, the non-linearity of gravity kicks in, and various effects can be observed. Some of the critical effects associated with physical phenomena are discussed here. Radiation-reaction force that causes the orbits to inspiral and circularizes over time through dissipation of energy enters at 2.5 PN in the dynamics and at the leading order in phasing. The tail terms also enter at 2.5 PN at leading order. They arise because the propagating field gets scattered off from the static background. It contains information about the source at an earlier time than the retarded time.

Including the spin of the two objects gives rise to two main effects, namely spin-orbit (SO), which is linear and spin-spin (SS), which is quadratic. The leading-order SO effect arises at the 1.5 PN, next to leading order (NLO) at 2.5 PN and next to next to leading order (NNLO) at the 3.5 PN. The SS effect enters at leading order at 2 PN and NLO at 3 PN (it includes both the coupling between different spins and spin squared terms) and NNLO at 4 PN (includes interaction between different spins).

The PN evolution is based on adiabatic approximation according to which the fractional change in the orbital frequency ω over each orbital period is negligibly small, i.e., $\Delta\omega/\omega \ll 1$ and this assumption starts failing as the system approaches last stable orbit. The frequency of last stable orbit is given by $f_{LSO} = (6^{\frac{3}{2}}\pi M)^{-1}$. For GW, we are interested in the evolution of the orbital phase $\phi(t)$, which is computed as a perturbative expansion in terms of a small parameter $v = (\pi M f)^{\frac{1}{3}}$ in PN approximation, where v is the characteristic velocity of the system and f is the GW frequency. Under the adiabatic approximation and for the restricted waveform (in which the GW phase is twice the orbital phase), the evolution of the orbital phase is given by

the following differential equations:

$$\frac{d\Phi(t)}{dt} = \frac{v^3}{M}, \quad (3.2)$$

$$\frac{dv}{dt} = \frac{-\mathcal{F}(v)}{ME'(v)}, \quad (3.3)$$

which can be recast as

$$t(v) = t_{ref} + M \int_v^{v_{ref}} dv \frac{E'(v)}{\mathcal{F}(v)}, \quad (3.4)$$

$$\Phi(v) = \Phi_{ref} + \int_v^{v_{ref}} dv v^3 \frac{E'(v)}{\mathcal{F}(v)}, \quad (3.5)$$

where $\mathcal{F}(v)$ is the GW luminosity and $E'(v)$ is the derivative of the binding energy with respect to v . t_{ref} and Φ_{ref} are the constants of integration and v_{ref} is an arbitrary reference velocity. As this is a perturbative expansion, we have the freedom to treat the RHS of Eq. (3.2) with different methods, as long as we maintain the correct order of the expansion. This gives rise to different PN approximants. For instance, the `TaylorT1` approximant is obtained by expanding the $\mathcal{F}(v)$ and $E'(v)$ individually to a consistent PN order, plugging those into Eq. (3.2) and then solving the differential equations numerically. Alternatively, we can also expand the ratio of $\mathcal{F}(v)/E'(v)$ to a consistent PN order which gives rise to the `TaylorT4` approximant. We can also use the equivalent phasing relations (3.4) to obtain GW phasing by expanding the ratio of $\mathcal{F}(v)/E'(v)$, substituting and then integrating the equations (3.4) give rise to transcendental equations for $\Phi(v)$ and $t(v)$. This approximant is `TaylorT2`. Before solving the transcendental equations we can also invert $t(v)$ to get $v(t)$ and $\Phi(t) \equiv \Phi(v(t))$, this gives rise to the `TaylorT3` approximant. `TaylorEt` approximant is obtained by writing the energy E in terms of another variable (suitably adimensional) and then solving the evolution of v in terms of the new variable. All these approximants are time domain and computationally expensive to be used for data analysis purposes though they are implemented in `LALSuite`. The frequency domain PN approximants are obtained by using stationary phase approximation (SPA). The equivalent equations to (3.2) in frequency domain are given by:

$$\frac{d\Psi}{df} = 2\pi t, \quad (3.6)$$

$$\frac{dt}{df} = -\frac{\pi M^2 E'(f)}{3v^2 \mathcal{F}(f)}. \quad (3.7)$$

`TaylorF2` is one of the most used PN approximant and obtained by solving the above equations by expanding the energy and flux to a consistent order. The gravitational

waveform (TaylorF2) in SPA approximation in frequency domain can be written as:

$$\tilde{h}_{SPA}(f) = \mathcal{A} f^{-\frac{7}{6}} \exp^{-i\Psi(f)}, \quad (3.8)$$

where \mathcal{A} is the amplitude, f is GW frequency and $\Psi(f)$ is the GW phase in the frequency domain. The explicit formula for GW phasing at 3.5 PN order for all mentioned approximants is given in Ref. [63]. The most used models based on PN approximation and implemented in LALSuite are the following. **TaylorF2**: The TaylorF2 model is a frequency-domain PN-based waveform model for the inspiral of BBH systems. It uses a 3.5 PN accurate point-particle baseline [64] and includes the spin-orbit interaction up to 3.5 PN [65] and the spin-spin interaction up to 3 PN and p to 3 PN-accurate, EOS-dependent, self-spin terms [66–70]. **TaylorF2_{Tides}**: The TaylorF2_{Tides} uses TaylorF2 as baseline, but adds tidal effects up to 6 PN as presented in Ref. [32]. This model was used in the analysis of GW170817 [Collab1, Collab2].

3.2 Effective-one-body family

The PN expansion which is based on adiabatic approximation is a poorly convergent series and when the two objects are very close it fails. Therefore, the merger cannot be modeled using PN expansion. To mitigate this problem [71–74] has come up with a resummation method for PN expansion which is non perturbative in nature. The basic idea is to map the relativistic two-body problem with masses M_A and M_B onto the motion of a test particle with mass $\mu = M_A M_B / M$ in some effective external metric, $g_{\mu\nu}^{\text{eff}}$. This approach is called effective-one-body (EOB) theory. In polar coordinates (r, θ, ϕ) , the effective metric is defined as:

$$g_{\mu\nu}^{\text{eff}} dx^\mu dx^\nu = -A(r; \nu) c^2 dt^2 + B(r; \nu) dr^2 + r^2 (d\theta + \sin^2(\theta) d\phi^2). \quad (3.9)$$

The potentials $A(r; \nu)$ and $B(r; \nu)$ can be written as Taylor expansions in $GM/(c^2 r)$. The metric is constructed in such a way that it reduces to Schwarzschild metric in the $\nu \rightarrow 0$ and for the non spinning case. The key elements of the EOB approach are the EOB Hamiltonian (H_{EOB}), a dissipative radiation-reaction force \mathcal{F} , and GWs. The rescaled effective Hamiltonian ($\hat{H}_{\text{eff}} = H_{\text{eff}}/\mu$) describes the dynamics of the system in terms of rescaled variables for non-spinning case is given by

$$\hat{H}_{\text{eff}}(u, p_{r_*}, p_\phi) = \sqrt{A(u; \nu) (1 + p_\phi^2 u^2 + 2\nu(4 - 3\nu) u^2 p_{r_*}^4) + p_{r_*}^2}, \quad (3.10)$$

and the mapping between the effective Hamiltonian and real Hamiltonian H_{EOB} is:

$$H_{EOB} = \mu \hat{H}_{EOB} = M \sqrt{1 + 2\nu(\hat{H}_{\text{eff}} - 1)}, \quad (3.11)$$

where $u \equiv 1/R \equiv GM/(rc^2)$, $p_\phi \equiv P_\phi/M\mu$ is the dimensionless angular momentum and $p_{r_*} \equiv P_r/\mu$ is the dimensionless radial momentum. The resulting Hamiltonian equations of motion are

$$\frac{dR}{dt} = \left(\frac{A}{B}\right)^{\frac{1}{2}} \frac{\partial \hat{H}_{EOB}}{\partial p_{r_*}}, \quad (3.12)$$

$$\frac{d\phi}{dt} = \Omega = \frac{\partial \hat{H}_{EOB}}{\partial p_\phi}, \quad (3.13)$$

$$\frac{dp_{r_*}}{dt} = -\left(\frac{A}{B}\right)^{\frac{1}{2}} \frac{\partial \hat{H}_{EOB}}{\partial R} + \hat{\mathcal{F}}_{r_*}, \quad (3.14)$$

$$\frac{dp_\phi}{dt} = \hat{\mathcal{F}}_\phi, \quad (3.15)$$

where $(\hat{\mathcal{F}}_{r_*,\phi} = \mathcal{F}_{r_*,\phi}/\mu)$ is the rescaled radiation reaction force. The radial component \mathcal{F}_{r_*} is set to zero (this is called Damour-Jaranowski-Schäfer gauge) [73, 75] though other choices can also be made, and the azimuthal component (\mathcal{F}_ϕ) is given by

$$\mathcal{F}_\phi = -\frac{1}{8\pi\nu\Omega} \sum_{\ell=2}^{\ell_{max}} \sum_{m=1}^{\ell} (m\Omega)^2 |r h_{\ell m}|^2, \quad (3.16)$$

where $h_{\ell m}$ are the waveform (complex) multipoles. The distance rescaled multipolar waveform strain is defined as

$$(h_+ - ih_\times) = \sum_{\ell=2}^{\ell_{max}} \sum_{m=-\ell}^{\ell} h_{\ell m} {}_{-2}Y_{\ell m}(\theta, \Phi). \quad (3.17)$$

${}_{-2}Y(\theta, \Phi)$ are the $s = -2$ spin-weighted spherical harmonics and the multipoles $h_{\ell m}$ are given by

$$h_{\ell m} = h_{\ell m}^{N,\epsilon} \hat{S}_{\text{eff}}^N \hat{h}_{\ell m}^{\text{tail}} f_{\ell m} \hat{h}_{\ell m}^{\text{NQC}}, \quad (3.18)$$

where $h_{\ell m}^{N,\epsilon}$ describes the Newtonian contribution, \hat{S}_{eff}^N is source term, $\hat{h}_{\ell m}^{\text{tail}}$ tail term, $f_{\ell m}$ the residual amplitude corrections and $\hat{h}_{\ell m}^{\text{NQC}}$ are the next-to-quasi-circular correction factors. For detailed description of each term we refer to [76].

There are two families of approximants based on the EOB approach, TEObResum and SEObNR. The two approximants are different in the context of computing Hamiltonian H_{eff} , $A(u; r)$ and $B(u; r)$. Both have parameters tuned to NR simulations to have better control on the dynamics at the merger, see e.g., section VI of [77] and references therein, for detailed comparison of the two models. The most recent avatars of both methods implemented in LALSuite are: **SEObNRv4_ROM**: This approximant is based on an EOB description of the general-relativistic two-body problem [71, 72], with free coefficients tuned to NR waveforms [71, 78]. It provides inspiral-merger-ringdown waveforms for BBH coalescences. For a faster computation of individual

waveforms reduced-order-modeling techniques are employed (indicated by the suffix ROM in the name tag) [79].

TEOBResum: TEOBResum was introduced in [76] following the general formalism outlined in [21]. The approximant incorporates an enhanced attractive tidal potential derived from resummed PN and gravitational self-force expressions of the EOB A -potential that describes tidal interactions [21, 80]. The resummed tidal potential of TEOBResum improves the description of tidal interactions near the merger with respect to the next-to-next-to-leading-order tidal EOB model [24, 81] and is compatible within large regions of the BNS parameter space with high-resolution, multi-orbit NR results within their uncertainties [76, 82]. We use this model to cover the inspiral regime to construct hybrids waveforms for a few cases (described in Chapter 4). **TEOBResum_ROM:** Given the high computational cost of the TEOBResum approximant, we employ a reduced-order-model technique for parameter estimation purposes [83]. There are some systematic differences between TEOBResum approximant and TEOBResum_ROM, which are discussed in the results section of Ref. [83]. **TEOBResumS:** This is the updated version of TEOBResum, which includes spins of the objects. For BNS, tidal effects are incorporated by computing a resummed attractive potential such that the tidal phase includes NLO tidal contributions, gravitational self-force description of relativistic tidal interactions, and is tuned to NR data. It incorporates the EOS dependent self-spin effects (or quadrupole-monopole term up to NLO). For details, we refer to [77].

3.3 Phenomenological family

For the GW data analysis, fast-to-evaluate and accurate waveform templates are required. The primary aim of the phenomenological model is to provide efficient, but approximate waveform models for template placement. Basically, it provides strain h as given in Eq. (3.8) in frequency domain for ($l = 2$ and $m = \pm 2$ modes). The first aligned-spin model for coalescing BBH based on this approach is known as IMRPhenomB. It depends on 3 parameters ($M, \eta, \chi_{\text{eff}}$), where amplitude is rescaled by $M = M_A + M_B$, $\eta = M_A M_B / M^2$ is the symmetric mass ratio, and the single spin parameter is $\chi_{\text{eff}} = (M_A \chi_A + M_B \chi_B) / M$, where $\chi_i = |\vec{S}_i| / M_i^2$ is dimensionless spin parameter and \vec{S}_i is spin angular momentum of the i^{th} BH.

The basic idea is to make phenomenological ansatz about the amplitude ($A(f)$) and phase ($\Psi(f)$) for different regime of the waveform, e.g.,:

$$A(f) \equiv \mathcal{C} f_1^{-\frac{7}{6}} \begin{cases} \left(\frac{f}{f_1}\right)^{-7/6} \left(1 + \sum_{i=2}^3 \alpha_i v^i\right) & \text{if } f < f_1 \\ w_m \left(\frac{f}{f_1}\right)^{-2/3} \left(1 + \sum_{i=1}^2 \epsilon_i v^i\right) & \text{if } f_1 \leq f < f_2 \\ w_r \mathcal{L}(f, f_2, \sigma) & \text{if } f_2 \leq f < f_3, \end{cases}$$

$$\Psi(f) \equiv 2\pi f t_0 + \varphi_0 + \frac{3}{128\eta v^5} \left(1 + \sum_{k=2}^7 v^k \Psi_k\right). \quad (3.19)$$

where \mathcal{C} is numerical constant that depends on sky location, orientation and masses of the source; $v \equiv (\pi M f)^{1/3}$, t_0 is the arrival time of the signal at the detector, and φ is the corresponding phase. (f_1, f_2) are the transition frequencies and f_3 is the cutoff frequency. w_m and w_r are normalization constants and are estimated by demanding that the amplitude and phase should be continuous throughout. \mathcal{L} is the Lorentzian function with width σ centered around f_2 . $\epsilon_{1,2}$ depends on spin and can be calculated by PN+NR waveforms. $\alpha_{2,3}$ are PN corrections to amplitude and depend on η . $(\Psi_k, f_1, f_2, f_3, \sigma)$ are the phenomenological parameters which are then mapped to the real physical parameters like (η, χ) and the mapping coefficients are calculated by fitting to the PN+NR waveforms. For explicit formulae see, e.g., [84]. Further development of this model led to IMRPhenomC approximant, where the transition between the different regimes of the waveform, namely, inspiral, merger-ringdown is smoother, which made the approximant more accurate. Its domain of validity is $q \leq 4, \chi_{\text{eff}} \leq 0.75$ (0.85 for equal mass system). Furthermore, IMRPhenomD approximant was constructed by calibrating it to 18 hybrid waveforms constructed by glueing together SEOB and NR waveforms with parameter span across $q \leq 18, \chi_{\text{eff}} \leq 0.85$ (0.98 for equal mass system). Moreover, the model comes with modularity, i.e., one can update inspiral and merger-ringdown part independently. IMRPhenomHM uses the dominant mode ($\ell = m = |2|$) information of a frequency domain non-precessing BBH model; and rescaled and stretch, the amplitude and phase such that the higher-order multipolar waveform is constructed. It employs PN and perturbation theory [85]. All these approximants are implemented in LAL, some of the most used ones are:

IMRPhenomD: IMRPhenomD is a phenomenological, frequency-domain waveform model discussed in detail in Refs. [86, 87]. It describes non-precessing BBH coalescences throughout inspiral, merger, and ringdown. While the inspiral is based on the TaylorF2 approximation, it is calibrated to EOB results, and the late inspiral, merger, and ringdown are calibrated to NR simulations.

IMRPhenomP: describes the GW from the precessing BBH merger throughout the inspiral, merger and ringdown [88]. It employs the fact that the multipoles gen-

erated by non-precessing BBHs in an inertial frame can model the multipoles produced by precessing BBH in a co-precessing frame. Then, the precessing model can be obtained by carefully rotating the non-precessing waveforms that account for the precession of orbital plane. Effect of precession can be seen as a modulation in amplitude and phase of GW signal, and it is most prominent for signals with small mass-ratios q , large spin components perpendicular to the orbital angular momentum and system viewed close to edge-on. The intrinsic parameters which characterizes the model are mass-ratio q , effective spin parameter χ_{eff} and effective spin-precession parameter χ_p ,

$$\chi_p = \text{max} \left(\chi_{A\perp}, \frac{3 + 4q}{4 + 3q} q \chi_{B\perp} \right) \quad (3.20)$$

where $\chi_{i\perp}$ denotes the magnitude of the component of the dimensionless spin perpendicular to the orbital angular momentum. The latest version of this model implemented in LAL is IMRPhenomPv2 [88, 89], which uses IMRPhenomD as its non-precessing model and rotates it to deliver precessing waveforms. For effective use of the model, one needs to specify a reference frequency at which spin related quantities such that χ_p and individual spin magnitude χ_i are extracted.

3.4 NRTidal model

This approximant provides the tidal contribution to the phase evolution which could be augmented to any BBH model to be then used as a BNS model [89] [Dudi3]. The key features are:

(i) The phase of the GW signal from a BNS merger as a function of dimensionless GW frequency $\hat{\omega} = M\partial\phi(t)/dt$, can be approximated as:

$$\phi(\hat{\omega}) \approx \phi(\hat{\omega})_{PP} + \phi(\hat{\omega})_{spins} + \phi(\hat{\omega})_{Tides}, \quad (3.21)$$

where $\phi(\hat{\omega})_{PP}$ denotes the point-particle baseline (non-spinning BH) contribution to the phasing. $\phi(\hat{\omega})_{spins}$ is the contribution due to spins of the stars and $\phi(\hat{\omega})_{Tides}$ denotes the tidal contribution to the phase evolution which enters at 5 PN order, see e.g., Sec. (2.2).

(ii) The tidal contribution to phase $\phi(\hat{\omega})_{Tides}$ can be parameterized by effective tidal coupling constant κ_{eff} , which captures the leading-order EOS effects very well.

$$\kappa_{\text{eff}}^T = \frac{2}{13} \left[\left(1 + 12 \frac{X_B}{X_A} \right) \left(\frac{X_A}{C_A} \right)^5 k_2^A + (A \leftrightarrow B) \right], \quad (3.22)$$

where $X_{A,B} = M_{A,B}/M$, $C_{A,B}$ are the compactness of star A and B and k_2^A is the quadrupolar Love number (see Sec. 2.2) where A and B label the two NSs. The tidal parameter κ_{eff}^T and tidal deformability parameter $\tilde{\Lambda}$ are connected via $\tilde{\Lambda} = 16/3\kappa_{\text{eff}}^T$

and individual tidal polarizabilities $\Lambda_{A,B} = 2k_2^{A,B}/(3C_{A,B}^5)$.

(iii) The NLO PN expression for the tidal contribution is fully known [21, 26, 90].

$$\Phi_{Tides} = -\kappa_{\text{eff}}^T \frac{C_{\text{Newt}}}{X_A X_B} x^{5/2} (1 + c_1 x), \quad (3.23)$$

where $x(\hat{\omega}) = (\hat{\omega}/2)^{2/3}$ and $c_{\text{Newt}} = -13/8$. $c_1 = 1817/364$ for the equal mass case.

(iv) Following expression represents the tidal effects beyond the NLO:

$$\Phi_{Tides} = -\kappa_{\text{eff}}^T \frac{C_{\text{Newt}}}{X_A X_B} x^{5/2} P_{\Phi}^{\text{NRTidal}}(\hat{\omega}). \quad (3.24)$$

In the low frequency regime ($\hat{\omega}) \leq 0.0074$, $P_{\Phi}^{\text{NRTidal}}$ converges to the PN expression already known for tidal phase Eq. (3.23). For $\hat{\omega} \in [0.0074, 0.04]$ $P(\hat{\omega})$ is determined using EOB waveforms [76, 91]. Richardson extrapolated NR data [89] is employed for $\hat{\omega} \in [0.04, 0.17]$. The spin and tidal contributions are decoupled for the spin values explored by NR data employed for fitting the coefficients, well within NR uncertainties, which gives:

$$P_{\Phi}^{\text{NRTidal}}(\hat{\omega}) = \frac{1 + n_1 x + n_{3/2} x^{3/2} + n_2 x^2 + n_{5/2} x^{5/2} + n_3 x^3}{1 + d_1 x + d_{3/2} x^{3/2}}. \quad (3.25)$$

The closed form fit for the tidal phase correction in time domain is given by:

$$\Phi_T = -\kappa_{\text{eff}}^T \frac{C_{\text{Newt}}}{X_A X_B} x^{5/2} \times \frac{1 + n_1 x + n_{3/2} x^{3/2} + n_2 x^2 + n_{5/2} x^{5/2} + n_3 x^3}{1 + d_1 x + d_{3/2} x^{3/2}}. \quad (3.26)$$

To capture the tidal phasing in strong field regime the coefficients are tuned to NR simulations of BNS mergers thus the model is called NRTidal. The fitting coefficients are $(n_1, n_{3/2}, n_2, n_{5/2}, n_3) = (-17.941, 57.983, -298.876, 964.192, -936.844)$, $d_{3/2} = 43.446$. For details about NR data and fitting see [89]. The frequency domain tidal phase is obtained using the SPA:

$$\Psi^{\text{NRTidal}} = -\kappa_{\text{eff}}^T \frac{\tilde{C}_{\text{Newt}}}{X_A X_B} x^{5/2} \times \frac{1 + \tilde{n}_1 x + \tilde{n}_{3/2} x^{3/2} + \tilde{n}_2 x^2 + \tilde{n}_{5/2} x^{5/2} + \tilde{n}_3 x^3}{1 + \tilde{d}_1 x + \tilde{d}_{3/2} x^{3/2}}, \quad (3.27)$$

where $x = x(f)$, $\tilde{C}_{\text{Newt}} = 39/16$ and $\tilde{d}_1 = \tilde{n}_1 - 3115/1248$ and $(\tilde{n}_1, \tilde{n}_{3/2}, \tilde{n}_2, \tilde{n}_{5/2}) = (-17.428, 31.867, -26.414, 62.362)$ and $\tilde{d}_{3/2} = 36.089$. $\tilde{d}_1 = (\hat{n}_1 - \hat{c}_1)$ ensures that the NLO tidal term is correctly recovered. The NRTidal model Eq. (3.27) can be

augmented to any tidal free waveform model:

$$h^{\text{tidal}} = h^{\text{PP}} \cdot (A^{\text{NRTidal}} e^{-i\Psi^{\text{NRTidal}}}), \quad (3.28)$$

where A^{NRTidal} is a function which smoothly turns off the waveform after termination frequency, which is related to the merger frequency. h^{PP} is the point particle baseline GW polarization obtained from `LALSimulation`. The `NRTidal` has been added to the following BBH models spin-aligned as well as precessing using the prescription given by Eq. (3.28) and these models are used for the analysis of GW170817 [92].

IMRPhenomD_NRtidal: To obtain BNS waveforms, `IMRPhenomD` BBH approximant is augmented with tidal phase corrections Ref. [89]. The waveform model terminates at the end of the inspiral; the termination frequency is prescribed by fits to NR simulations [see [Dudi3] for details].

SEOBNRv4_ROM_NRtidal: Similarly to the `IMRPhenomD_NRTidal` model, this model augments the BBH approximant `SEOBNRv4_ROM` with `NRtidal` phase corrections [89].

IMRPhenomPv2_NRtidal: The tidal effects are added to the underlying spin-aligned waveform model, and then the waveform is rotated to add precession effects (e.g., see [88]).

Chapter 4

Hybrid waveform

All the waveform models, discussed in Chapter 3, are limited in their region of validity, e.g., PN is valid during the inspiral part, EOB and phenomenological waveforms cover up to merger for BNS system and NR simulations probe the late inspiral, merger and post-merger part of the waveform. In this chapter, we discuss the construction of hybrid BNS waveforms that cover all three regimes, namely, the inspiral, merger, and post-merger, and serve as a full BNS waveform. The hybrid waveforms have been used in the studies [Dudi1, Dudi3, Dudi4, Collab3]. We list all the hybrids that we produced and are publicly available on the CoRe website [Collab3] in Tab. 4.1.

We often require to validate the waveform models against the full waveform (inspiral-merger-post-merger) to check their accuracy or to tune the free parameters of a model. This is done either by calculating the mismatch with the hybrid waveform or by injecting hybrid waveform as signals and then recover the parameters by employing the waveform model. These are some of the applications of the hybrid waveforms. We discuss the applications of hybrids with an example of `NRTidal` model in the last section.

We construct the full waveform by combining PN, EOB or phenomenological waveforms which cover the inspiral regime (left panel of Fig. 4.1) with waveforms produced by NR simulations to cover the merger and post-merger part (right panel of Fig. 4.1), this is called a hybrid waveform. We followed the procedure described in Ref. [Dudi1, Dudi3] to construct the hybrids. For the inspiral part of the signal, `TEOBResum` model (non-spinning) and `TEOBResumS` model (aligned-spin) [Sec. 3.3] constructed within EOB approach are employed. For late inspiral, merger and post-merger regime, the NR simulations, performed with `BAM` code provided the waveforms. These NR waveforms are already published in Ref. [Collab3] and the data is also publicly available at¹, cf. [Collab3]. More information about the NR simulations is provided in Chapter 7.

¹<http://www.computational-relativity.org/>

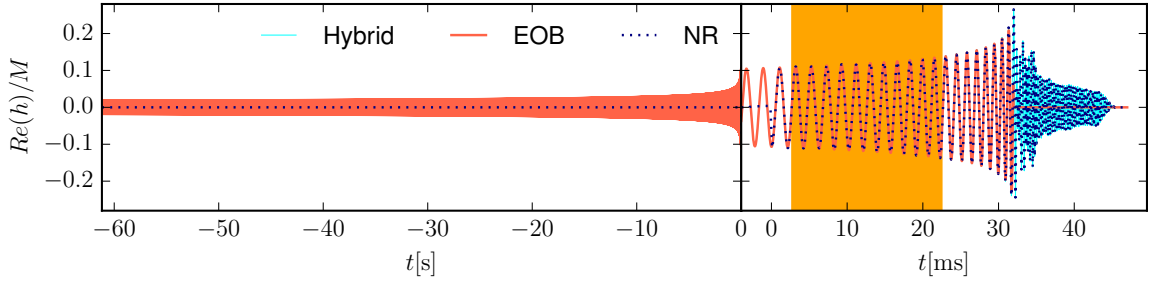


Figure 4.1: A hybrid waveform with $M_A = M_B = 1.35 M_\odot$ and employing the SLy EOS. The hybrid (thin, cyan line) consists of a tidal EOB part (red) and an NR part (dotted blue). The alignment interval is marked by the yellow shaded region in the right panel. The time $t = 0$ denotes the start of the NR simulation. The plot is taken from [Dudi1].

Consider the two waveforms, say EOB and NR, describing the same physical system, but covering two different regimes of the waveform with some overlap window. To hybridize them, we first align them by minimizing the phase difference between the two in a time window $[t_i, t_f]$:

$$\mathcal{I}(\delta t, \delta \phi) = \int_{t_i}^{t_f} dt |\phi_{\text{NR}}(t) - \phi_{\text{EOB}}(t + \delta t) + \delta \phi|^2, \quad (4.1)$$

with $\delta \phi$ and δt are relative constant phase and time shifts. ϕ_{NR} and ϕ_{EOB} denote the phases of the NR and tidal EOB waveform, respectively. The time window is chosen in such a way that it corresponds to the overlap window (yellow shaded region in 4.1) dimensionless frequency window $M\omega_{22} = \hat{\omega} \approx [0.04, 0.06]$. It has been showed in some studies [76, 82, 93] that the agreement between the EOB and NR waveform is remarkably excellent in this interval. Additionally, our particular choice for this window allows us to average out the phase oscillations linked to the residual eccentricity ($\sim 10^{-2}$) of the NR simulations. After aligning the waveforms, they are joined together using smooth transition function:

$$h_{\text{Hyb}}(t) = \begin{cases} h_{\text{EOB}}(t')e^{i\phi} & : t \leq t_i \\ h_{\text{NR}}(t)H(t) + h_{\text{EOB}}(t')e^{i\phi}[1 - H(t)] & : t_i \leq t \leq t_f \\ h_{\text{NR}}(t) & : t \geq t_f \end{cases} \quad (4.2)$$

where $t' = t + \delta t$, and $H(t)$ is the Hann window function

$$H(t) := \frac{1}{2} \left[1 - \cos \left(\pi \frac{t - t_i}{t_f - t_i} \right) \right]. \quad (4.3)$$

For estimating the accuracy of the hybrid waveforms, we calculate the phase difference between three different hybrids for same configuration but have different numerical resolutions and different time resolution dt for the ordinary-differential-

equation (ODE) integrator used in the `TEOBResum` model (Fig. 4.2). Hyb_1 (blue line on the top panel) denotes the hybrid with highest NR resolution ~ 128 grid points cover the NS and $dt = 0.50$ for the EOB ODE integrator resolution. Hyb_2 (green dash line in top panel) is the hybrid with lower NR resolution ~ 96 grid points but same EOB dataset. Hyb_3 denotes the hybrid with highest NR resolution 128 grid points and $dt = 0.25$ for the EOB. Hyb_1 is the hybrid shown in Fig. 4.1. To check the uncertainty in the hybrid construction, we calculate the dephasing between these hybrids and an error, defined as

$$\text{err} = \sqrt{(\phi_{\text{Hyb}_1} - \phi_{\text{Hyb}_2})^2 + (\phi_{\text{Hyb}_1} - \phi_{\text{Hyb}_3})^2}. \quad (4.4)$$

Here, ϕ_{Hyb_1} , ϕ_{Hyb_2} and ϕ_{Hyb_3} are the phases of hybrids Hyb_1 , Hyb_2 , and Hyb_3 , respectively. The error is shown in the bottom panel of Fig. 4.2. We aligned all three hybrids in early inspiral, i.e., in the frequency interval [32, 34] Hz to calculate the phase differences and error. We find that the difference between Hyb_1 and Hyb_2 is below ~ 0.1 radian and at merger well within the NR uncertainty (olive shaded region). The effect of the ODE integration within the EOB model is even smaller. However, this study does not include the systematic effects of the underlying EOB model, see Ref. [77] for further details. To further check the accuracy of the hybrids, we performed the Fourier transform of the hybrids and checked that the phase and amplitude vary smoothly with frequency. Fig. 4.3 shows the PSD of the same hybrid waveform that showed in Fig. 4.1. We also checked that the phase difference in the time domain between the EOB waveforms and the hybrids up to the merger has acceptable values. The wide range of applications of the hybrid waveforms can be seen in the following studies, where our hybrid waveforms are employed. (i) The waveform systematics study [Dudi1], where hybrids were injected as a true signal in a fiducial LIGO data stream at different SNRs and recovered using multiple waveform models (discussed in Sec. 4.1). (ii) To evaluate the performance of `NRTidal` models [Dudi3], we also employ the hybrid waveforms, which we discuss in Sec. 4.1 in detail. (iii) For further improvement of the `NRTidal` model, we also employed four hybrids starting at frequency 20 Hz with high resolution NR data (discussed in Sec. 6.2). We compared the new model `NRTidalv2` model against 18 hybrids (Tab. 4.1) to test its performance [Dudi4]. (iv) The hybrid waveforms are also used for evaluating and comparing the performance of `TaylorF2pseudo5.5PN` waveform model with other models (discussed in Sec. 6.1).

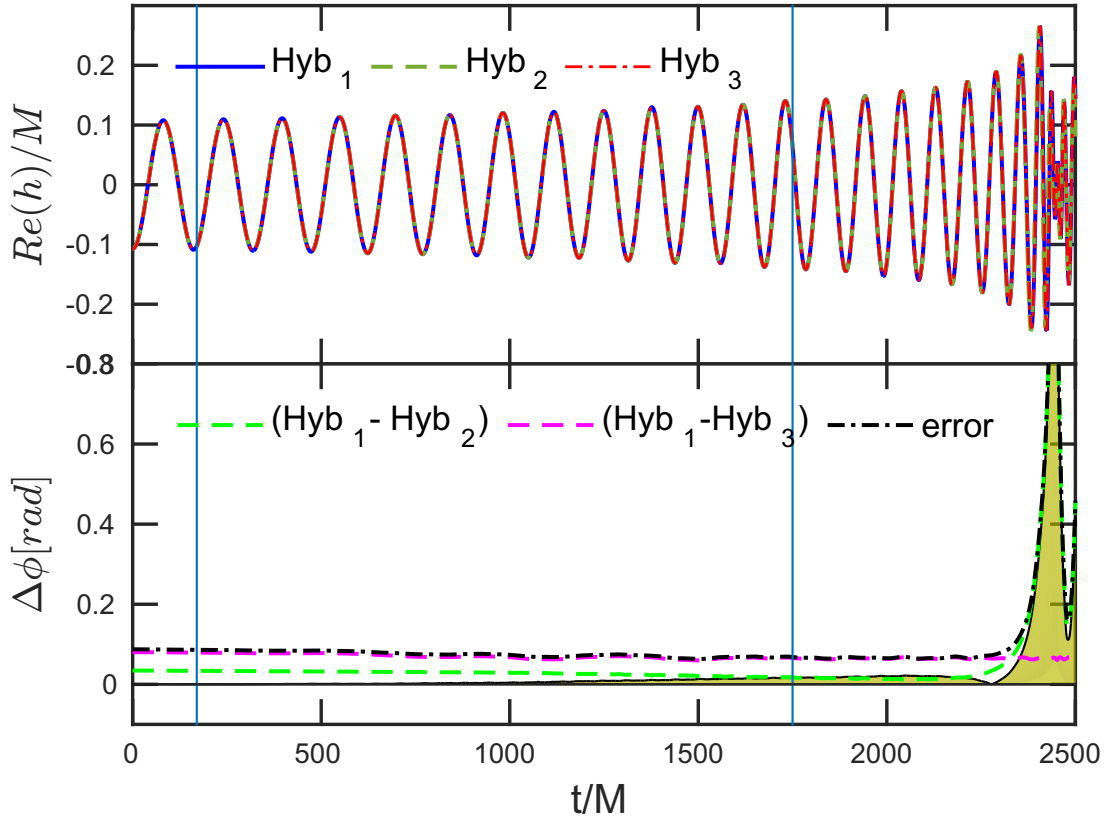
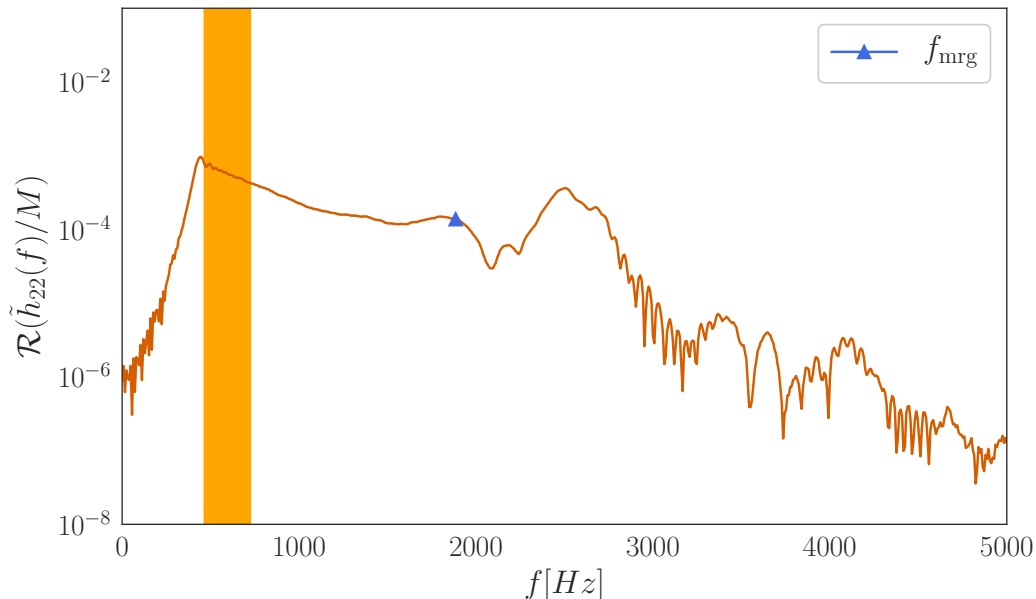


Figure 4.2: (*Top panel*): The three flavors of the hybrid discussed in the text, each constructed with a different NR resolution and EOB integrator settings. Red and blue dashed curves represent the same NR resolution but a different EOB integrator setting. The green dashed curve has a lower NR resolution but the same EOB integrator setting as the red curve. The hybrid in Fig. 4.1 corresponds to the blue curve here. (*Bottom panel*): Phase difference between the hybrid of Fig. 4.1, and its two other realizations. The green dashed curve represents the absolute dephasing with the hybrid with low NR resolution, while the pink curve shows the absolute dephasing with the hybrid using a different EOB integrator setting. The black curve represents the absolute error defined in Eq. (4.4). The vertical lines mark the boundaries of the alignment window. The olive shaded region is the dephasing between two NR resolutions used. The plot is taken from [Dudi1].

Table 4.1: BNS hybrid configurations. Name in CoRe database (first column), EOS (second column), primary and secondary gravitational mass of the two stars (column 3 and 4 respectively), dimensionless individual spin (column 5 and 6), compactness (column 7 and 8), and individual tidal deformability of the two stars (column 9 and 10). $\tilde{\Lambda}$ in column 11, and tidal coupling constant κ_{eff}^T in column 12 are given. Merger frequency of each waveform is listed in the last column. The table is adopted from Ref. [Dudi3].

Name	EOS	$M_A [M_\odot]$	$M_B [M_\odot]$	χ_A	χ_B	C_A	C_B	Λ^A	Λ^B	$\tilde{\Lambda}$	κ_{eff}^T	$f_{\text{mrg}} [\text{Hz}]$
equal mass, non-spinning												
CoRe:Hyb:0001	2B	1.3500	1.3500	0.000	0.000	0.205	0.205	127.5	127.5	127.5	23.9	2567
CoRe:Hyb:0002	SLy	1.3500	1.3500	0.000	0.000	0.174	0.174	392.1	392.1	392.1	73.5	2010
CoRe:Hyb:0003	H4	1.3717	1.3717	0.000	0.000	0.149	0.149	1013.4	1013.4	1013.4	190.0	1535
CoRe:Hyb:0004	MS1b	1.3500	1.3500	0.000	0.000	0.142	0.142	1536.7	1536.7	1536.7	288.1	1405
CoRe:Hyb:0005	MS1b	1.3750	1.3750	0.000	0.000	0.144	0.144	1389.4	1389.4	1389.4	260.5	1416
CoRe:Hyb:0006	SLy	1.3750	1.3750	0.000	0.000	0.178	0.178	347.3	347.3	347.3	65.1	1978
unequal mass, non-spinning												
CoRe:Hyb:0007	MS1b	1.5000	1.0000	0.000	0.000	0.157	0.109	866.5	7041.6	2433.5	456.3	1113
CoRe:Hyb:0008	MS1b	1.6500	1.1000	0.000	0.000	0.171	0.118	505.2	4405.9	1490.1	279.4	1170
CoRe:Hyb:0009	MS1b	1.5278	1.2222	0.000	0.000	0.159	0.130	779.6	2583.2	1420.4	266.3	1301
CoRe:Hyb:0010	SLy	1.5000	1.0000	0.000	0.000	0.194	0.129	192.3	2315.0	720.0	135.0	1504
CoRe:Hyb:0011	SLy	1.5274	1.2222	0.000	0.000	0.198	0.157	167.5	732.2	365.6	68.6	1770
CoRe:Hyb:0012	SLy	1.6500	1.0979	0.000	0.000	0.215	0.142	93.6	1372.3	408.1	76.5	1592
equal mass, spinning												
CoRe:Hyb:0013	H4	1.3726	1.3726	+0.141	+0.141	0.149	0.149	1009.1	1009.1	1009.1	189.2	1605
CoRe:Hyb:0014	MS1b	1.3504	1.3504	-0.099	-0.099	0.142	0.142	1534.5	1534.5	1534.5	287.7	1323
CoRe:Hyb:0015	MS1b	1.3504	1.3504	+0.099	+0.099	0.142	0.142	1534.5	1534.5	1534.5	287.7	1442
CoRe:Hyb:0016	MS1b	1.3509	1.3509	+0.149	+0.149	0.142	0.142	1531.8	1531.8	1531.8	287.2	1456
CoRe:Hyb:0017	SLy	1.3502	1.3502	+0.052	+0.052	0.174	0.174	392.0	392.0	392.0	73.5	2025
CoRe:Hyb:0018	SLy	1.3506	1.3506	+0.106	+0.106	0.174	0.174	391.0	391.0	391.0	73.5	2048

Figure 4.3: Fourier transform of the time domain hybrid waveform, which is shown in Fig. 4.1, as a function of frequency. The BNS system has equal mass stars with $M_A = M_B = 1.35M_\odot$ and EOS SLy.



4.1 Applications

To validate the phasing model based on `NRTidal` prescription given by Eq. (3.28), described in the Sec. 3.4, we compare them against the hybrid waveforms. We use the `TEOBResumS` model that covers the inspiral regime upto merger (discussed in Sec. 3.2) and NR waveforms that covers the merger and postmerger regime for full BNS waveform construction. All the hybrid waveforms listed in Tab. 4.1 are employed in this work. Here we briefly describe the tests we performed to quantify the performance of the `NRTidal` model as applications of the hybrid waveform and conclusion inferred from them. For more details, we refer the reader to Ref. [Dudi3]. The `NRTidal` model is augmented to various BBH models, which we have described in Sec. 3.4. We compute the mismatch in frequency domain between the augmented BBH models or also called template waveforms, and the hybrid waveforms. Additionally we also compute the mismatch with PN based models namely, `TaylorF2Tides` (here with 6.5 PN, 7 PN and 7.5 PN order tides included), `TaylorT4Tides` (with 5 PN and 6 PN tides). Both models incorporate up to 3 PN-accurate EOS-dependent self-spin terms [66–68]. The mismatch is computed as:

$$\bar{F} = 1 - \max_{\phi_c, t_c} \frac{(h_1(\phi_c, t_c)|h_2)}{\sqrt{(h_1|h_1)(h_2|h_2)}}, \quad (4.5)$$

where \bar{F} denotes the mismatch i.e., loss in SNR (squared) when the waveforms are aligned in time and phase. ϕ_c, t_c are an arbitrary phase and time shift between the approximants themselves and the hybrid waveforms. The noise-weighted inner product is defined as

$$(h_1|h_2) = 4\Re \int_{f_{\min}}^{f_{\max}} \frac{\tilde{h}_1(f)\tilde{h}_2^*(f)}{S_n(f)} df. \quad (4.6)$$

The waveforms in template bank are placed such that the maximum value of \bar{F} across the bank is 0.03. We compute mismatches for two scenarios, first when the minimum frequency, $f_{\min} = 30$ Hz, is constant and other by varying the f_{\min} and keeping the $f_{\max} = f_{\text{mrg}}$, (f_{mrg} is the merger frequency), i.e., constant. We calculate f_{mrg} from NR waveforms and show them as vertical dashed line in Fig. 4.4. Fig. 4.4 shows the mismatch between the hybrid waveforms and `NRTidal` templates for f_{\min} is constant. The solid curves are the mismatch between the hybrids with `TaylorF2Tides` (green), `TaylorT4Tides` (orange), `SEOBNRv4_ROM_NRTidal` (red), `IMRPhenomD_NRTidal` (blue), `IMRPhenomPv2_NRTidal` (cyan), and the dashed line represents the mismatch with respective point-mass baseline model. We find that the non-tidal models for the equal mass non-spinning case and for small tidal deformability have mismatches below $\sim 10^{-3}$ but with increasing the stiffness of the EOS mismatch also increases (left to right in Fig. 4.4). Mismatch for spinning cases

are unacceptably large ($> 1\%$) and increases with high spin values (see the third and fourth row in the figure). The mismatch between hybrids and $\text{TaylorF2}_{\text{Tides}}$ model also increases with $\tilde{\Lambda}$ for the equal mass non-spinning system. For the spinning case and soft EOS, mismatches are better, and we find overall acceptable mismatch ($< 1\%$) due to the inclusion of EOS dependent spin and tidal effects in $\text{TaylorF2}_{\text{Tides}}$. However, for unequal mass cases, $\text{TaylorF2}_{\text{Tides}}$ has the largest mismatch among all tidal models. Now, validating the performance of the NRTidal among each other, we find $\text{IMRPhenomD}_{\text{NRTidal}}$ and $\text{IMRPhenomPv2}_{\text{NRTidal}}$ have a smaller mismatch than $\text{SEOBNRv4}_{\text{ROM}_{\text{NRTidal}}}$, but the differences are small for equal mass non-spinning cases. However, for spinning cases $\text{IMRPhenomD}_{\text{NRTidal}}$ and $\text{SEOBNRv4}_{\text{ROM}_{\text{NRTidal}}}$, the mismatch exceeds the (1%) limit for a high spin. Although, $\text{IMRPhenomPv2}_{\text{NRTidal}}$, which is essentially $\text{IMRPhenomD}_{\text{NRTidal}}$ incorporated with EOS dependent self-spin terms, the mismatches are below 10^{-3} for spinning and non-spinning cases. As another test, we also compute the phase difference between hybrids and waveform approximants in the frequency domain, again for two cases. First, where we align the waveforms with hybrid waveforms from frequency 50 Hz to f_{mrg} and another where we align the waveforms only in range 50 to 500 Hz. We also test the performance of the waveform models in the time domain. We compute the accumulated error during the evolution by aligning the waveforms and hybrids in the time domain and comparing them. The main conclusions are: Non-tidal approximates have high mismatches for spinning or high $\tilde{\Lambda}$, i.e., stiff EOS cases. *For high spin magnitude $\chi_{A,B} \geq 0.1$, it is crucial to have EOS dependent self-spin terms in the waveform approximate to better describe the signal.* NRTidal model performs better than the PN based models for an unequal mass case and large tidal effects cases. We also compare the NRTidal model with non-hybridized TEOBResumS model upto dimensionless GW frequency $\hat{\omega} = 0.06$. This is the upper limit of the frequency interval in which we overlap and align the two waveforms for glueing them together. We compare dimensionless quantity $Q_{\hat{\omega}}$ (explained in Sec. 6.1) between the NRTidal and TEOBResumS model. We find that the NRTidal model systematically overestimates the tidal effects with respect to TEOBResumS . Therefore, improvements in NRTidal models are needed. For more details, see Sec. VI.B in Ref. [Dudi3]. This is also consistent with our findings in [Dudi1]. In Sec. 6.2, we discuss the improved NRTidal model, called NRTidalv2 .

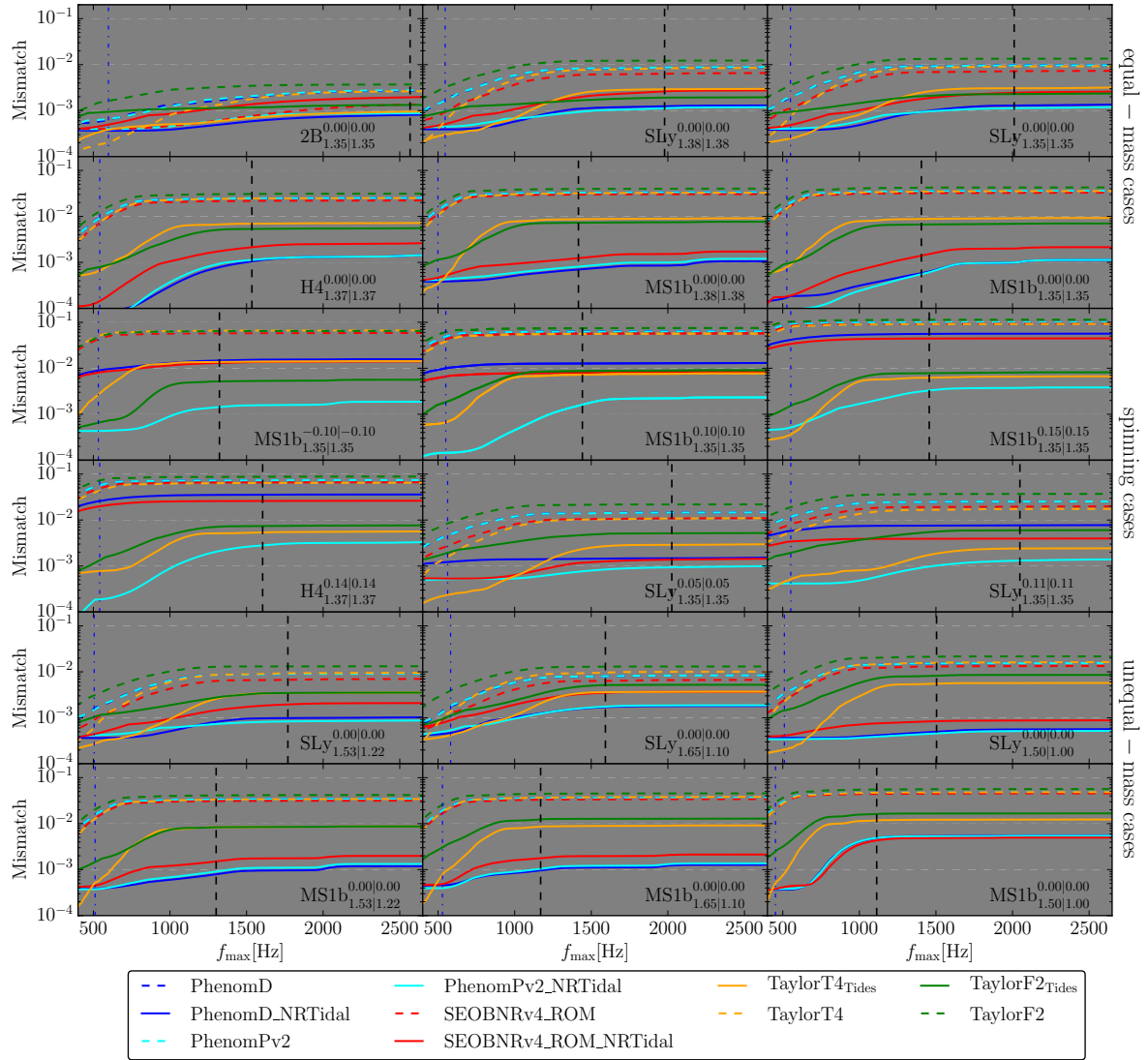


Figure 4.4: Mismatches between the tidal approximants and the hybrid waveforms based on the configurations listed in Tab. 4.1. Mismatches are computed following Eq. 4.5, where we set $f_{\min} = 30\text{Hz}$ and vary the maximum frequency f_{\max} . A black vertical dashed line marks the frequency corresponding to the moment of merger f_{mrg} . A blue dot-dashed line marks the middle of the hybridization region between the `TEOBResumS` and the NR data. Note that for the analysis of GW170817 in [94], a maximum frequency of 2048Hz was employed. The naming convention of the individual panels refers to the setup described in Tab. 4.1, namely: $\text{EOS}_{M_A|M_B}^{X_A|X_B}$. Regarding the waveform approximants, results for all models that do not include tidal effects are marked as dashed lines, while solid lines refer to waveform models with tidal effects. The color-coding is as follows: `TaylorF2Tides` (green), `TaylorT4Tides` (orange), `SEOBNRv4_ROM_NRTidal` (red), `IMRPhenomD_NRTidal` (blue), `IMRPhenomPv2_NRTidal` (cyan). Overall we find that the `IMRPhenomPv2_NRTidal` model performs best. In particular, this model is advantageous for spinning configurations. The plot is taken from [Dudi3].

Chapter 5

Waveform systematic study

The waveform models, discussed in Chapter 3, are used for parameter measurements of GW signals. However, the fidelity of parameter measurements depends not only on detector calibration uncertainty [95–97], the detector performance at the time of the event (both in terms of the overall sensitivity to the signal, and of the stability of the instrument due to the presence/absence of transient noise fluctuations [98]), but also on systematic errors in the theoretical waveforms employed to analyze the data, and any signal correlations between source parameters. In this chapter, we discuss the findings of [Dudi1], which focus on the systematic differences of the approximants in the context of parameter estimation of a BNS signal. We illustrate some of the results of the systematic study performed in Appendix B of Ref. [Collab2].

5.1 Systematics study

We investigate the errors/biases which occur due to approximate waveform models for BNS mergers. The waveform models, discussed in Chapter 3, are different from each other in terms of their region of validity and have approximate treatment of tidal effects; moreover, none of the waveform models have a post-merger part. Therefore, to be confident about one’s inference of parameters in light of a true signal, it is crucial to understand the differences between different waveform models. Therefore, we would like to investigate the following two questions in order to gain insights into the sources of systematics [Dudi1].

(i) *What kind of biases do we expect if tidal effects are neglected in the analysis of inspiral GW signal from a BNS merger?*

As already described, the NSs get closer while orbiting each other, and they deform each other by companion’s gravitational field, and this causes an increase in the inspiral rate. The inspiral rate also increases if the spins are anti-aligned with respect to the orbital angular momentum or by a change in binary’s mass ratio. Therefore, there is a degeneracy among the mass, spin, and tidal deformability parameter $\tilde{\Lambda}$. As the tidal effects enter at 5 PN order, it might be possible that for small tidal de-

formabilities or weak signals, i.e., small SNR, tidal effects can be neglected and or may be compensated by changing the spin and mass parameter for louder signals. We investigate these scenarios and present example in a later section.

(ii) *Does the use of inspiral-only waveforms lead to a significant loss of information, or possibly to biases in the estimation of the source properties?*

Currently, waveform models used to interpret BNS observations do not include the merger and post-merger regimes. Although NR simulations of BNS mergers have made tremendous progress in recent years [81, 89, 99–107], we do not yet have complete models of the inspiral, merger, and post-merger regime, as we do for BBH systems¹ [79, 88, 109, 110]. The waveform models used for current GW analyses are either truncated prior to the merger or are BBH models through the merger and ringdown (which we include here). While one might expect that these approximations do not impact parameter estimates, because of the signal detectable by current ground-based detectors contain negligible power at merger frequencies, this assumption must be properly validated, especially in light of the fact that the GW energy emitted during the post-merger stage can even exceed the GW energy released during the entire inspiral up to the merger, cf. Fig. 3 [111]. For our investigation, we produce complete inspiral, merger and post-merger BNS waveforms by combining state-of-the-art tidal EOB waveforms for the inspiral, and NR simulations of the late inspiral and merger (as described in Chapter 4). We do this for two choices of the NS EOS: a *soft* EOS, namely SLy [112], corresponding to relatively compressible nuclear matter, and a *stiff* EOS, namely MS1b [113], corresponding to relatively incompressible nuclear matter. These yield NSs with low and high tidal deformabilities, respectively. We inject hybrid waveforms in the fiducial data stream of two LIGO detectors, situated in Hanford and Livingston, US [15]. The event, GW170817 has put an upper bound on $\tilde{\Lambda} \leq 720^2$ [Collab2] but this work was started well before the detection of the event and also the extreme scenarios help us in understanding the systematics better. The binary systems employed in this work have equal masses of both NSs ($M_A = M_B = 1.35M_\odot$), with chirp mass $\mathcal{M} = 1.752$ and a total mass $M = 2.70M_\odot$ and are non-spinning. We use Bayesian inference for parameter estimation (discussed in Sec. 2.6). For sampling multidimensional parameter space to obtain credible intervals, we employ a `lalinference_mcmc` algorithm included in the LALInference package of (LALSuite). We choose uniform prior probability density $p(\theta)$ for the individual masses of the NSs in the interval $[1M_\odot, 3M_\odot]$ and also for dimensionless aligned spins between $[-1, 1]$. Uniform prior for individual tidal deformability $\tilde{\Lambda}_2^{A,B}$ is also chosen in the interval $[0, 5000]$ for all the waveform models except for TEObResum_ROM, where uniform prior between 50 to 5000 applied. With

¹Recently, Breschi et al. [108] has developed a time domain analytical model for the post-merger signals

²Recall that $\tilde{\Lambda}$ depends on mass and so as this bound

regards to tidal deformability, our setup makes the simplifying assumption of ignoring correlations between Λ_2^A , Λ_2^B , and the mass parameters, which are known to exist [19, 20, 25]. We employ the standard set up of GW data analysis for all other parameters, e.g., [Collab2].

EOS	$\tilde{\Lambda}$	$\mathcal{M} [M_\odot]$	χ_{eff}	PSD	f_{high}	SNR
SLy	392	1.1752	0.0	O1	2048 Hz	25
					2048 Hz	100
				ZDHP	2048 Hz	100
					8192 Hz	100
MS1b	1536	1.1752	0.0	O1	2048 Hz	25
					2048 Hz	100
				ZDHP	2048 Hz	100
					8192 Hz	100

Table 5.1: The eight injections employed to study systematic among different waveform models. We consider two equal-mass, non-spinning BNS hybrid waveforms (as described in the text) with the same chirp mass, but different EOS, and hence different tidal polarizability $\tilde{\Lambda}$. The SNR of each injection is specified in the seventh column. When assessing the impact of tidal effects on the analysis of a GW inspiral signal, we use the first observing run’s noise PSD. In such cases, the waveform models employed to recover the signal are IMRPhenomD_NRTidal, SEOBNRv4_ROM_NRTidal, TaylorF2_{Tides}, IMRPhenomD, TaylorF2, and TEOBResum_ROM. When assessing the impact of post-merger dynamics on GW inference, instead, we use the projected noise curve for the Advanced LIGO detectors in the ZDHP configuration and IMRPhenomD_NRTidal and TaylorF2_{Tides} waveform models for the signal recovery. Given that the high-frequency content of the post-merger portion of the signal reaches ~ 4 kHz, we produce injections with sampling rates of 16384 Hz and 4096 Hz, and correspondingly use a high-frequency cutoff in our Bayesian analysis of $f_{\text{high}} = 8192$ Hz and $f_{\text{high}} = 2048$ Hz. The merger frequencies are 2010 Hz, and 1405 Hz for waveforms with SLy and MS1b EOS, respectively. The table is taken from Ref. [Dudi1].

We employ different waveform models to extract the properties of the injected signal. Some of the models include tidal effects namely, TaylorF2_{Tides} (3.5 PN order point-particle baseline and 6 PN order tides), IMRPhenomD_NRTidal, SEOBNRv4_ROM_NRTidal, TEOBResum_ROM and BBH models namely, TaylorF2 and IMRPhenomD (discussed in chapter 3). We use a variety of waveform models so to estimate the systematic error in the parameter estimation pipelines. We also use TEOBResum_ROM [83] model for estimating the parameters, whereas our hybrids are constructed using tidal EOB TEOBResum approximant. We do this in order to check that the recovered values and injected values are consistent. Tab. 5.1 summarizes the various injection scenarios we consider for the injections. To investigate the first

question about the impact of neglecting the tidal effects in the analysis of GW inspiral, we inject the individual hybrid waveform for two EOS, SLy and MS1b and assume the noise PSD of first observing run $O1$ ³. We inject each hybrid with 4 different injection scenarios, which gives a total of 8 scenarios, as summarized in Tab. 5.1. We inject at two different SNR 25 and 100 [rows 1, 2, 5, and 6 in Tab. 5.1]. SNR 25 is moderately high and is also close to the SNR of GW170817, which was 32.4. Whereas SNR 100 allows us to investigate the impact of tidal effects have on the recovery of BNS source properties for an extreme scenario. We also use SNR 100 for investigating the impact of the absence of post-merger dynamics on the data analysis. As the post-merger signal has high frequency content upto ~ 4000 Hz, we produce injection at two different sampling rate namely, 4096 Hz and 16384 Hz which correspond to a high-frequency cutoff in our Bayesian analysis of $f_{\text{high}} = 2048$ Hz and $f_{\text{high}} = 8192$ Hz, respectively (rows 3, 4, 7, and 8 in Table 5.1). We assume the projected noise curve for the Advanced LIGO detectors in the ZDHP [115]. In all cases, no actual noise is added to the data. This allows us to obtain posteriors that do not depend upon a specific noise realization, therefore isolating systematic errors. All injections start at a frequency of 30 Hz, while our Bayesian analysis uses a low cutoff frequency $f_{\text{low}} = 32$ Hz to generate template waveforms. As discussed above, we use a number of different waveform approximants for estimating parameters. This allows us to assess systematic errors qualitatively present in such waveform models. As opposed to the full inspiral-merger-post-merger BNS signals we inject, the waveform models used for estimating parameters are limited to the inspiral regime. The insights we gained by comparing the results of parameter estimation using different waveform models are summarized in the following subsections.

5.1.1 Effects of tidal terms

First, we investigate what conditions bias the measurements of mass and spin, if one uses BBH models, i.e., neglect tidal effects to analyze the signal from a BNS coalescence. And then, qualitatively assess different tidal waveform approximants by investigating the biases in masses, spins, and measurement of tidal deformability for different injection scenarios. Let us recall that the chirp mass, mass ratio, spins, and tidal effects enter the waveform phase evolution at different PN order. The evolution is dominated by the chirp mass. χ_{eff} characterizes the spin contribution to the phase for parameter estimation. For the binary black hole problem, it has been shown that the effects of an increase in spins can be mimicked by a lower mass ratio of the binary [116–120]. Tidal effects also cause the inspiral to speed up, which could be partially compensated by changing the mass ratio and spin effects. Though

³The PSD is generated from 512 s of LIGO data measured adjacent to the coalescence time of the first BBH detection [6, 114]. This is of comparable sensitivity to that of the LIGO detectors during both the first and second observing runs.

the degeneracy is not definite, it is possible that neglecting tidal effects could lead to bias in spin and mass ratio measurements. We assess the extent of these biases by comparing the posteriors of the recovered parameter from different waveform model for different injection scenarios.

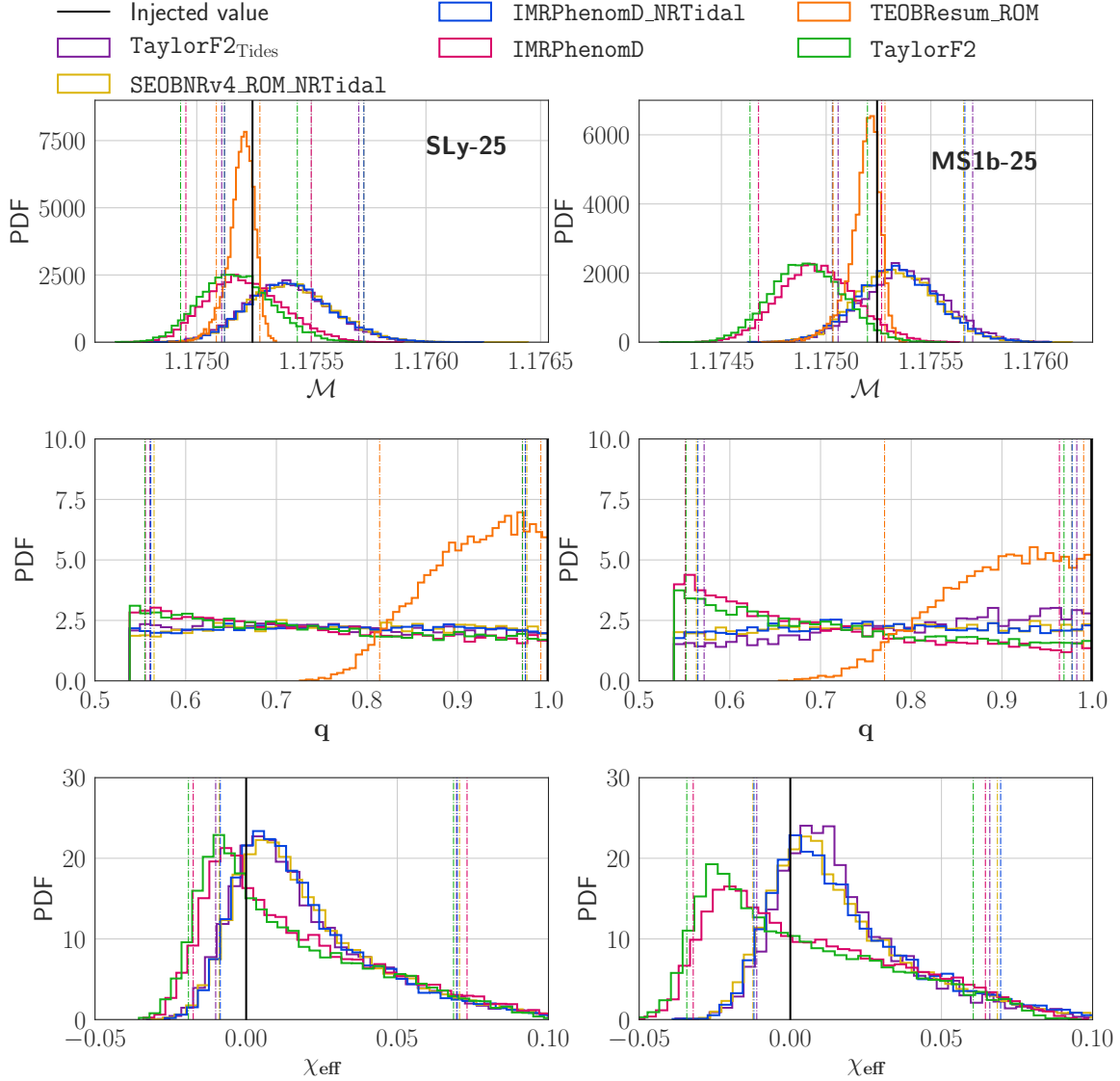


Figure 5.1: The chirp mass \mathcal{M} (*top panel*), mass ratio q (*middle panel*), and effective spin χ_{eff} (*bottom panel*) posterior distributions for the BNS injection with SLy EOS (left column) and MS1b EOS (right column) at SNR 25. The vertical dashed lines mark the 90% credible intervals, while the solid black line indicates the injected value. The plot is taken from [Dudi1].

First we discuss the recovered parameters for the signal injection with EOS SLy and SNR 25. Fig. 5.1 (left column) shows the posteriors of the chirp mass \mathcal{M} , mass ratio q and χ_{eff} , where the solid black line indicates the injected value. For all the approximants the injected value lies under the 90% credible interval. The posteriors obtained using TEOBResum_ROM approximant for chirp mass \mathcal{M} and mass ratio q differ from the ones yielded from other approximants; as TEOBResum_ROM is a non-

spinning waveform approximant thus, it explores a different parameter space than others. Except for `TEOBResum_ROM`, the peak of the posteriors distribution of chirp mass is slightly shifted towards the higher value for approximants containing tidal effects while for `BBH` model, i.e., approximants which neglect the tidal effects, the peak is slightly lower than the injected value. The effect of the degeneracy between mass-ratio and spin is clearly visible in the posteriors obtained for `TEOBResum_ROM`, which is a non-spinning model, and thus the mass-ratio is recovered with greater accuracy whereas, for other approximants, we obtain a flat distribution for q due to degeneracy. Though they do start to rail against the lower prior bound, this is a small effect for parameter estimation problems. The non-tidal approximant's peak is again shifted to lower values from the true value for measurements of spin and slightly towards higher value for tidal approximants. The injected value lies inside 90% credible region for all approximants again. For injection with soft EOS at low SNR ≈ 25 , neglecting tidal effects does not lead to significant bias in measurements of masses and spins. This picture changes when we consider a stiffer EOS. The right column of Fig. 5.1 shows the same quantities, but for the `MS1b` configuration ($\tilde{\Lambda} = 1536$) injected at SNR 25. The biases in the measurement of spins and mass-ratio are more significant here for non-tidal approximants. For the measurement of chirp mass, the tidal approximants are consistent with the injected value, but the non-tidal approximants are biased: for `TaylorF2`, the injected value is outside the 90% credible interval and for `IMRPhenomD` it is very close to the edge of the credible interval. The posteriors obtained for the measurement of mass-ratio also rail more significantly towards the lower prior limit for non-tidal approximants. Also, we observe the peaks of spin distribution is shifted more from the injected value towards the lower values for non-tidal approximants. Altogether, we conclude based on the above results that for stiff EOS at this SNR, neglecting tidal terms does lead to a bias in the measurements of the masses and spins. Assuming future observations will be similar to `GW170817` ($\tilde{\Lambda} < 720$ [Collab2]), and that SNRs higher than 25 will be rare; our results suggest that neglecting tidal effects will not significantly bias measurements of masses and spins for typical observations. However, careful analyses will be required once individual events are combined to extract information about the BNS population as a whole.

We also explore how these results change for the injections with much higher SNR. Fig. 5.2 shows again the same quantities for injection with EOS `SLy` at SNR 100. We see that for the non-tidal approximants the chirp mass is biased away from the true value, mass-ratio are railing towards the lower prior bound much more significantly and spins estimates are also biased. For parameter estimation we have put a limit over component masses $M_{A,B} \in [1, 3]M_{\odot}$, which implies $\mathcal{M} \in [0.8706, 2.6117]M_{\odot}$.

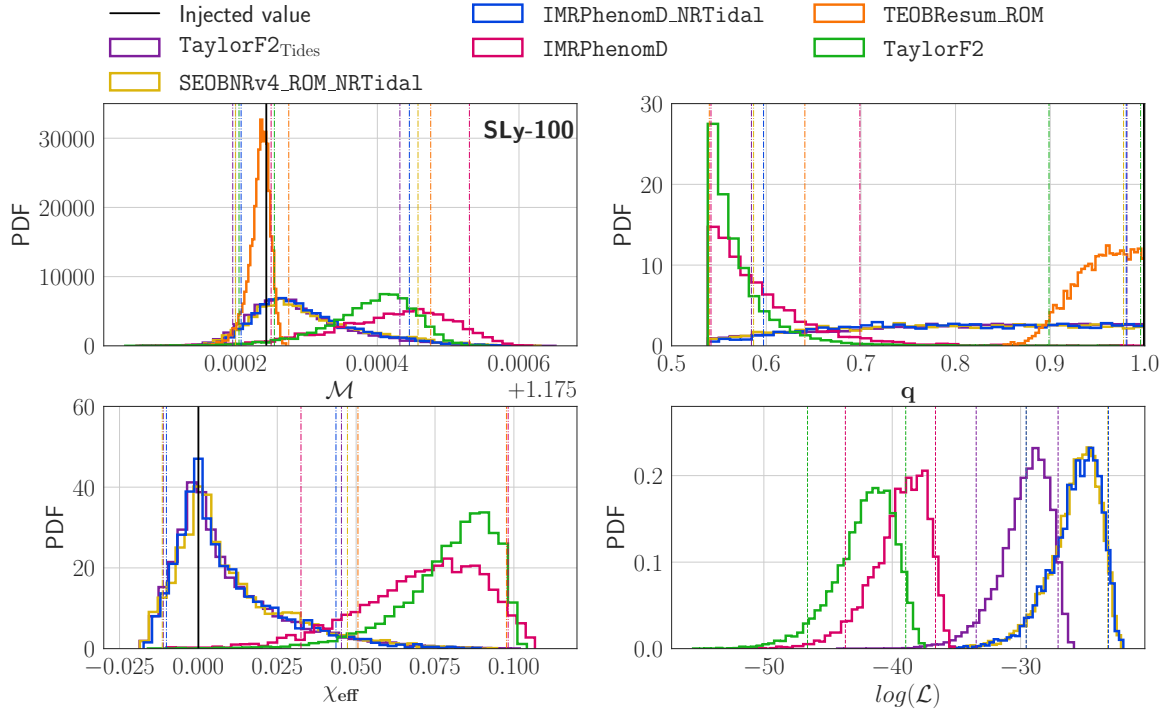


Figure 5.2: Same as Fig. 5.1, but with an injected SNR of 100 for SLy EOS. We also show the distribution of the logarithm of the likelihood in the bottom-right panel. The plot is taken from [Dudi1].

The parameter estimation code adjusts the masses and spins to find the best match with the data, and for those approximants that do not include tidal terms, the search rails against the limits on the masses, as well as on the physical limit $\chi \leq 1$ for the spins. This is most clear in the plot of the posterior distribution for q . The bottom-right panel of Fig. (5.2) shows the logarithm of the likelihood. It can be seen that the non-tidal approximant, namely, TaylorF2 and IMRPhenomD model, do not match the data as accurately as the tidal approximants as their likelihoods are lower. Though by changing the limits on masses and spins may lead to an increase in likelihood value for those approximants, but we do not expect it to be as high as for the tidal approximants since the missing tidal effects are partially mimicked by biases in masses and spins. It can also be seen that the TaylorF2_{Tides} approximant also has a lower likelihood as compare to NRTidal approximants, for which the tidal terms have been tuned to the NR waveforms. Let's now move on to comparing different tidal approximants in the context of measuring the tidal deformability, $\tilde{\Lambda}$. Fig. 5.3 shows the posteriors of tidal deformability; the left two panels show the result for injection with SLy EOS (at SNRs 25 (top panel) and 100 (bottom panel) and similarly, the right panel shows the result for MS1b configuration.

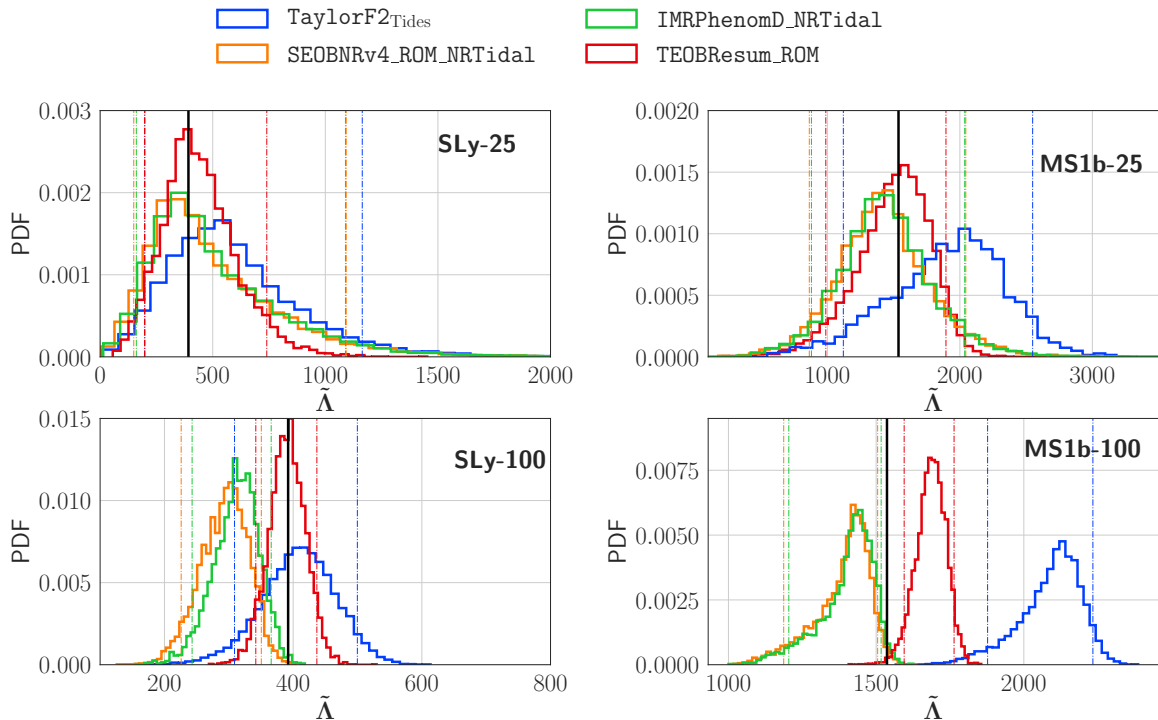


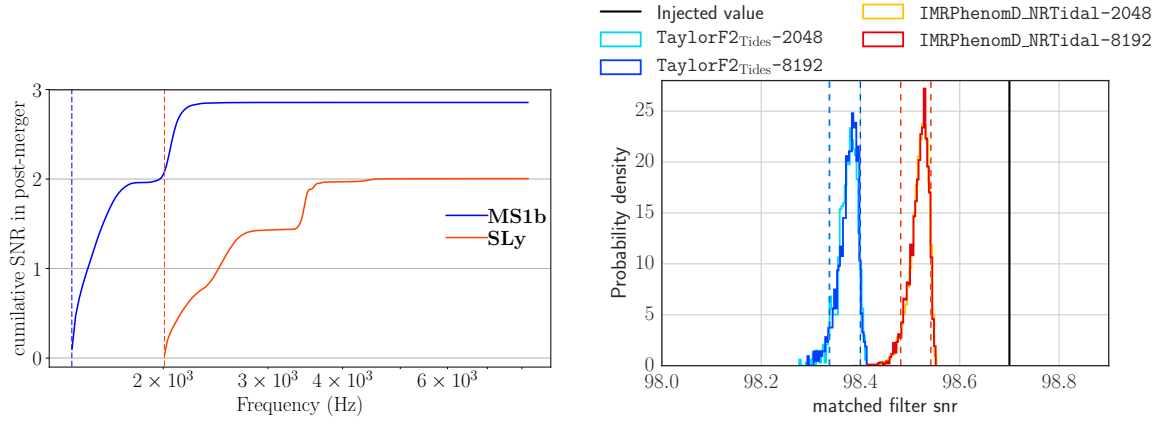
Figure 5.3: Measurements of the tidal deformability parameter. The two panels on the left show results for the SLy signal injected at SNR 25 (*top*) and 100 (*bottom*). The two panels on the right show results for the MS1b signal injected at SNR 25 (*top*) and 100 (*bottom*). The plot is taken from [Dudi1].

For injection at low SNR ≈ 25 which is comparable with the BNS event, GW170817, again, which is observed at an SNR of 32.4 Ref. [Collab1], all tidal approximants considered here agree within 90% credible interval for both soft and stiff EOS. We found that the $\text{TaylorF2}_{\text{Tides}}$ approximant can be used to put an upper bound on $\tilde{\Lambda}$ measurement, which is also consistent with findings of the Ref. [Collab2] for all configurations. The measurement of $\tilde{\Lambda}$ for signals at an SNR 100 is shifted towards lower values from the true values for the NRTidal approximants. This shows that we do not have sufficient hold on the systematics for high SNR setups. The reason for this behavior could be the differences in the BH limit between the two approximants. Another possible reason could be that the tidal effects in the NRTidal model are larger than in the TEOBResum model, as already highlighted in Fig. 10 of Ref. [Dudi3]. The agreement of $\text{TaylorF2}_{\text{Tides}}$ in the bottom-left panel of Fig. 5.3 is accidental. (We believe that this is due to a compensation of two effects: $\text{TaylorF2}_{\text{Tides}}$ models underestimating tidal effects and therefore overestimating $\tilde{\Lambda}$, and systematics errors in the point-particle description [Dudi2]. We investigate this in Sec. 6.1) We also note that at SNR 100, the TEOBResum approximant provides a biased measurement for MS1b. This may be surprising at first since TEOBResum was used in the construction of the MS1b hybrid, but the approximant is used only up to the hybridization frequency, from which point onwards the NR waveform is used. There is an SNR of ~ 16 from

the hybridization frequency up to the merger. As already stated, there are also systematic differences between `TEOBResum` and `TEOBResum_ROM` [83]. We found a phase difference between our hybrid and the waveform generated using `TEOBResum_ROM` of about ~ 4 radian at the merger for the MS1b case, and ~ 0.8 radian for the SLy case. We suggest this to be the reason for the offset between the injected value and the `TEOBResum_ROM` result at $\text{SNR} = 100$, cf. Fig. 5.3.

5.1.2 Effect of postmerger

We now investigate whether the lack of the post-merger part of the signal in the models, which we use for Bayesian inference, could lead to biases in parameter measurements. Previous studies of post-merger GW signals [44, 121, 122] suggest that this portion of the signal would be detectable, and its properties measurable, only if the SNR of the post-merger regime alone were above ~ 5 . Recently, [122] found that for soft EOSs and SNR of 3–4 might be sufficient for a detection of the post-merger GW using the BayesWave algorithm [123]. In this article, we assume a threshold SNR of 5 to produce more conservative estimates. Fig. 5.4a shows the accumulated SNR of the post-merger regime for our SLy and MS1b configurations at a total signal SNR of 100. In order to achieve a post-merger SNR of 5, we would need a total signal SNRs of approximately 185 and 250, for the MS1b and SLy EOSs, respectively. These would correspond to source distances of 17 Mpc and 13 Mpc. If we assume an SNR signal detection threshold of 10 and a uniform volume distribution of sources throughout the universe, then only about 1 in every 6000 observations will have an SNR greater than 185. This suggests that it is unlikely for Advanced LIGO and Virgo detectors to be able to measure post-merger signals and that it is therefore extremely unlikely that the post-merger part that is absent from our signal models will bias the parameter recovery from the inspiral waveform. Nonetheless, our hybrid waveforms provide the opportunity to test this expectation conclusively, and that is what we do in this section. To quantify the impact of the post-merger portion of the signal, we injected full, hybrid waveforms at $\text{SNR} = 100$ and compared results obtained using upper cutoff frequencies $f_{\text{high}} = 2048$ Hz and $f_{\text{high}} = 8192$ Hz. The merger frequencies f_{merger} are 2010 Hz and 1405 Hz for waveforms with the SLy and the MS1b EOS, respectively, and the frequency content of the post-merger signal reaches up to ~ 4000 Hz, with peak frequencies at $f_1 \sim 2600$ Hz and $f_2 \sim 3400$ Hz for SLy, and $f_1 \sim 1600$ Hz and $f_2 \sim 2100$ Hz for MS1b. We find that the results of parameter estimation for the two different cutoff frequencies are remarkably in agreement with each other, suggesting that the lack of post-merger content in the models used for parameter estimation has no impact on the recovery for this configuration.



(a) SNR accumulated during the post-merger regime as a function of frequency. The vertical lines indicate the merger frequency, where the computation of the SNR starts. Blue and red curves correspond to the hybrid being injected. The ZDHP projected noise curve for the Advanced LIGO detectors is used. The plot is taken from [Dudi1].

(b) The matched filter SNR recovered by TaylorF2_{Tides} and IMRPhenomD_NRTidal for the EOS-MS1b hybrid injected at SNR=100, using two different sampling rates for the templates, namely, 4096 Hz and 16384 Hz. Vertical dashed lines indicate 90% credible intervals, while the black solid line marks the injected value. The plot is taken from [Dudi1].

Fig. 5.4b shows that the recovered SNR is insensitive to the upper cutoff frequency, *i.e.*, to the presence/absence of post-merger content in the injected signal, and to the waveform model used in the recovery, since results for IMRPhenomD_NRTidal and TaylorF2_{Tides} are quite close. Further, in all four cases the full injected SNR is recovered. The $\sim 2\%$ drop from the nominal injected SNR of 100 to SNR = 98 is due to the fact that while the injected signal starts at 30 Hz, the filtering against the template waveform has a minimum frequency of 32 Hz. Fig. 5.5 shows the posterior distribution for $\tilde{\Lambda}$ for both choices of upper cutoff frequency, for the SLy (upper panel) and MS1b (bottom panel) configuration injected at SNR = 100, using the IMRPhenomD_NRTidal and TaylorF2_{Tides} waveform models. The upper cutoff frequency, or equivalently the inclusion or absence of the post-merger regime in the injected signal, has a negligible effect on the results. As was the case for the SNR = 100 injections performed with the first observing run noise PSD, the NRTidal models underestimate $\tilde{\Lambda}$ for all injections. For an explanation, we refer the reader to Sec. 5.1.1. These results are consistent with our expectation that the post-merger will have a negligible impact on our parameter recovery with the current generation of interferometric GW detectors.

In summary, we showed that neglecting tidal effects in the inspiral waveforms used to infer the source properties does not bias measurements of masses and spin for a canonical observation at SNR=25, as long as the NS EOS is fairly soft ($\tilde{\Lambda} \lesssim 400$). In the high SNR regime and/or for stiff EOSs ($\tilde{\Lambda} \sim 1500$), however, there will be a significant bias in the measurements of masses and spins when inspiral waveform models that do not include tidal effects are used (Figs. 5.1 (right panel) and 5.2).

Comparing tidal models amongst themselves, we found $\text{TaylorF2}_{\text{Tides}}$ overestimates the recovered value of $\tilde{\Lambda}$, as stated in the analysis of GW170817 [Collab2]. This is due to $\text{TaylorF2}_{\text{Tides}}$ favoring larger values of $\tilde{\Lambda}$ in order to compensate for the smaller tidal effects it includes in the phasing of the late inspiral regime when compared to NRTidal models [Dudi3]. At high SNR, the impact of systematic differences in the various waveform models is highlighted. In particular, the bottom panels of Fig. 5.3 show that NRTidal models yield a conservative lower estimate of $\tilde{\Lambda}$. It is not clear whether the differences between the NRTidal and TEOBResum approximants are dominated by differences in the BH ($\tilde{\Lambda} \rightarrow 0$) limit, or in the description of tidal effects, and this requires further study [124].

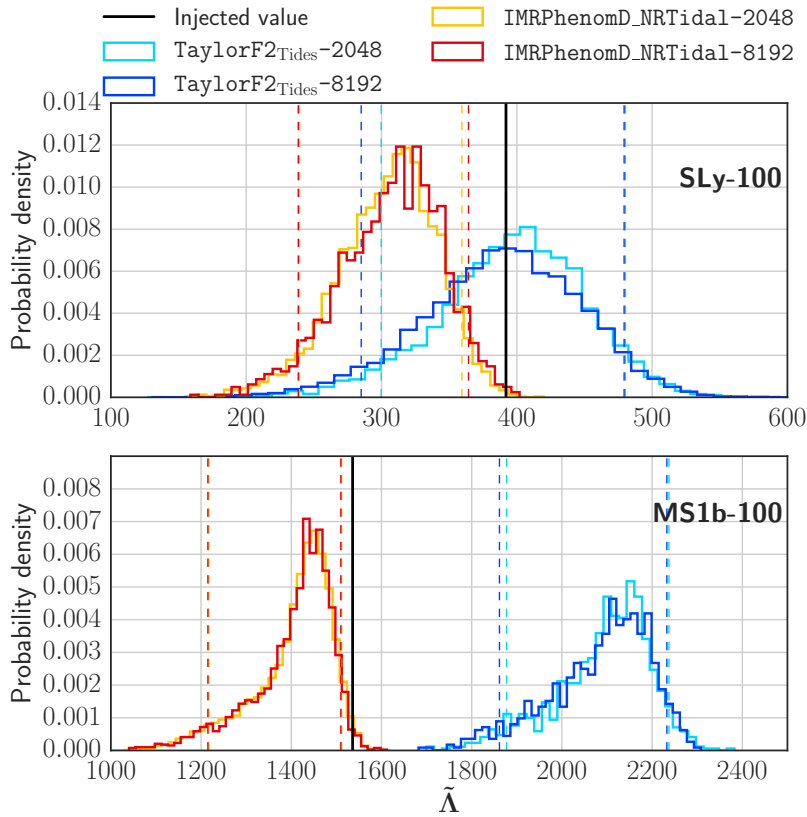


Figure 5.5: Tidal deformability posterior distributions found when injecting the SLy EOS (*top panel*) and the MS1b EOS (*bottom panel*) BNS hybrids at SNR 100. The recovery is performed the $\text{IMRPhenomD_NRTidal}$ and $\text{TaylorF2}_{\text{Tides}}$ approximants with sampling rates 16384 Hz and 4096 Hz. Vertical dashed lines indicate 90% credible intervals, while the black solid lines mark the injected values. The plot is taken from [Dudi1].

5.2 GW170817- systematics study

We briefly summarize some additional results that are part of the study of systematic effects presented in the Appendix B of Ref. [Collab2]. This study was a collaborative effort and here we only present the results for which parameter estimations runs were carried out by the author of this thesis. The motive of this study is twofold. First, in the presence of a true signal, it is necessary to verify the reliability of the parameter estimation techniques and waveform models. Second, to understand the systematic differences among different waveform models with a focus on tidal deformability ($\tilde{\Lambda}$). In order to verify the reliability of the parameter estimation techniques and employed waveform models; for the first GW detection event, GW150914, state-of-the-art numerical waveforms were injected in the data stream, and reliable values of the parameters were recovered by the waveform templates [114], which were also used to interpret the detected signal. Similarly, for GW170817, we employ the time domain aligned spin SEOBNRv4T (discussed in Sec.3.2) model to generate the waveforms for injection. We note that these injected waveforms lacked a post-merger part, and also the employed version does not include spin induced quadrupole moment. We employ the parameter estimation methods (discussed in Section 2.3) to infer the source properties of the signal. The SEOBNRv4T model was injected into zero-noise data with a network SNR of 32. We employ the noise PSD of GW170817.

Injection	$(M_A, M_B) [M_\odot]$	(χ_A, χ_B)	EOS	(Λ_1, Λ_2)	$\tilde{\Lambda}$
APR-0-0	(1.38, 1.37)	(0, 0)	APR4	(275, 309)	292
APR-1-0	(1.68, 1.13)	(0, 0)	APR4	(77, 973)	303
APR-0-1	(1.38, 1.37)	(0.04, 0)	APR4	(275, 309)	292
APR-0-5	(1.38, 1.37)	(-0.4, -0.4)	APR4	(275, 309)	292
H-0-0	(1.38, 1.37)	(0, 0)	H	(1018, 1063)	1040
2H-0-0	(1.38, 1.37)	(0, 0)	2H	(1018, 1063)	1040
BBH-0-0	(1.38, 1.37)	(0, 0)	-	(0, 0)	0
BBH-1-0	(1.68, 1.13)	(0, 0)	-	(0, 0)	0
BBH-0-2	(1.38, 1.37)	(-0.03, -0.03)	-	(0, 0)	0
BBH-1-2	(1.68, 1.13)	(-0.03, -0.03)	-	(0, 0)	0

Table 5.2: Parameters used for the injected SEOBNRv4T waveform. The table lists the name of the injection (column 1), masses of the two stars (column 2), dimensionless individual spin magnitudes (column 3), employed EOS (column 4), individual and combined tidal deformability (column 5 and 6). The chosen masses and spins are consistent with the measured posteriors for GW170817. The tidal parameters are calculated from the mass and chosen EOS. The bottom panel gives the parameter for the injected BBH waveforms. The table is adopted from [Collab2].

We choose three different EOS, namely, APR4, H, and 2H, for the injections. APR4 is chosen as it is near the peak of the $\tilde{\Lambda}$ posteriors, as shown in Fig. 2.2. H

[125] is a stiffer EOS which is at the allowed maximum limit of $\tilde{\Lambda}$ posteriors, again given in the Fig. 2.2. We also employ 2H, which is very stiff and outside the allowed maximum limit of $\tilde{\Lambda}$ posteriors, as shown in Fig. 2.2. For APR4 EOS, we employ four injection scenarios and are listed in the Tab. 5.2. (i) APR-0-0: an approximate equal mass system with no spins. (ii) APR-1-0: unequal mass system ($q = 0.67$) with no spins. (iii) APR-0-1: an approximate equal mass system with small spin ($\chi_A = 0.04$) on the primary mass. (iv) APR-0-5: an approximate equal mass system with large anti-aligned spin ($\chi_{A,B} = -0.4$) on both stars. Approximate equal mass systems with no spins and with stiffer EOS, H and 2H are also injected and are given as H-0-0 and 2H-0-0 in the Tab. 5.2. Injections with BBH waveforms that are constructed using SEOBNRv4, are given in the bottom panel in the Tab. 5.2. They are, BBH-0-0: approximate equal mass systems without spins and BBH-0-2: approximate equal mass system with small spins ($\chi_{A,B} = -0.03$); BBH-1-2: unequal mass systems with small spins ($\chi_{A,B} = -0.03$) and BBH-1-0: approximate equal mass system without spins. The various injection scenarios are motivated from the measured posteriors of GW170817.

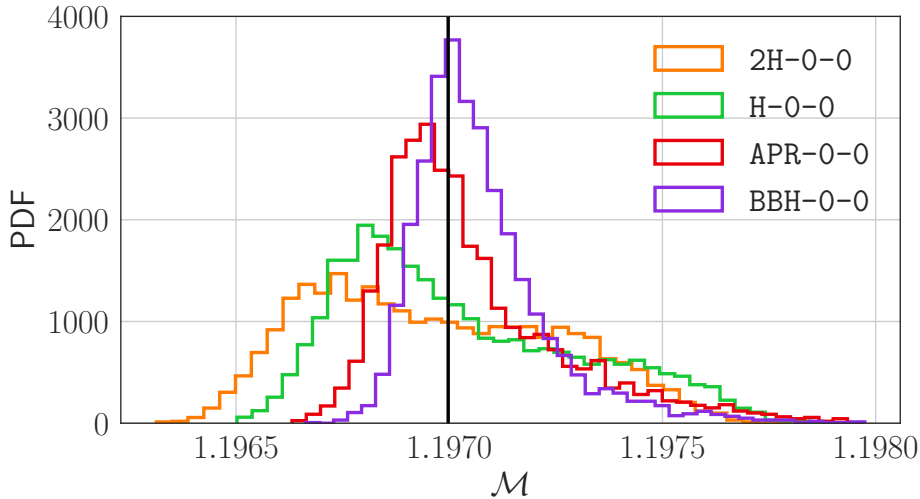


Figure 5.6: Posteriors of the chirp mass \mathcal{M} recovered using IMRPhenomPv2 model for injections with approximate equal mass non-spinning system with EOS APR4, H and 2H, and BBH waveform. These scenarios are listed in Tab. 5.2 as APR-0-0, H-0-0, 2H-0-0 and BBH-0-0. The solid vertical line represents injected value.

We use high spin prior $|\chi| \leq 0.89$ and the same PSD as used for GW170817. We also inject the waveform at an SNR of 32. As in Ref. [Dudi1], here, we also inject the waveforms in the zero-noise realization of the data. We employ three aligned-spin waveform models, namely, TaylorF2_{Tides}, IMRPhenomD_{NRTidal}, SEOBNRv4_{ROM_{NRTidal}}, and one precessing BBH model IMRPhenomPv2 to infer the properties of the injected waveforms. The main results with respect to tidal deformability $\tilde{\Lambda}$ have already been discussed in Appendix B of Ref. [Collab2], which we refer the reader for further details. Here we present a subset of the results which were

not presented earlier. We discuss results for all the injected scenarios as listed in Tab. 5.2 employing the IMRPhenomPv2 model only for estimating parameters, which is a BBH precessing model. We show posteriors of chirp mass \mathcal{M} that are recovered by the IMRPhenomPv2 model in Fig. 5.6, for injections with the approximate equal mass system with no spins and EOS APR4, H and 2H, as well as BBH waveform. The black solid vertical line indicates the injected value. The injected values lie within the 90% credible interval for all three EOS and BBH injection. However, it is to note that the peak of the posteriors shifts towards lower value as the EOS of the injected system gets stiffer. In Fig. 5.7, the marginalized posteriors of chirp mass \mathcal{M} for injection with the equal mass system with spins are shown. The recovered chirp mass for APR-0-1 injection, which is approximately equal mass system with small aligned spin ($\chi_A = 0.04$) on the primary mass, is shifted towards a smaller value, while for injection APR-0-5, which has anti-aligned spin ($\chi_{A,B} = -0.4$) on both stars, the posteriors are shifted towards high value. Although for BBH injection with spin ($\chi_{A,B} = -0.03$), the peak of the posterior is in agreement with the injected value. Therefore for signals like GW170817, it is crucial to employ waveform models with tidal effects otherwise, as it is visible in Fig. 5.7, that the recovered mass parameter might get biased.

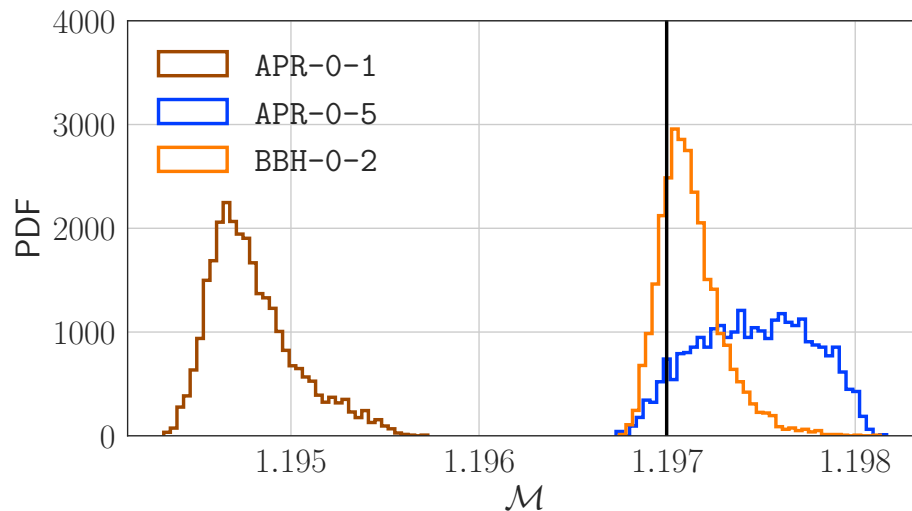


Figure 5.7: Posteriors of the chirp mass \mathcal{M} recovered using IMRPhenomPv2 model for injections with equal mass and spinning system with EOS APR4 and BBH model. These scenarios are listed in Tab. 5.2 as APR-0-1, APR-0-5 and BBH-0-2. The solid vertical line represents the injected value.

We show marginalized posteriors of the mass ratio q in the top panel and χ_{eff} in the bottom panel in the Fig. 5.8 for different injected scenarios as listed in Tab. 5.2. We compare posteriors for various cases for injections with BBH model and with soft EOS APR4 obtained by employing the IMRPhenomPv2 model. In the left panel of the figure, we compare posteriors obtained for injection with the approximate equal

mass non-spinning system, namely, APR-0-0 and BBH-0-0. In the middle panel: approximate equal mass but different spin configurations, namely APR-0-1, APR-0-5, and BBH-0-2 injection scenario as given in Tab. 5.2. For injection with the unequal mass non-spinning system, APR-1-0 and BBH-1-0 scenarios are compared in the right panel. The solid vertical lines indicate the injected value for the respective case. As already stated that there is a degeneracy among spin, mass, and tidal parameters, it is more evident in the following results. The posteriors obtained for injections with equal mass and non-spinning systems for BBH as well as soft EOS APR4 are in agreement with each other and with the injected value (left panel of Fig. 5.7). However, for injections with approximate equal mass and spins for BBH and EOS APR4, the posteriors for spin and mass ratio are biased (middle panel of Fig. 5.7). For low spin injections, namely, BBH-0-2 and APR4-0-1, the χ_{eff} is in agreement with the injected value, but for high spin injection APR4-0-5, the injected value is not in the 90% credible region, and the recovered values are biased towards small anti-aligned values. The recovery of mass ratio, for the same injection, is also biased. For equal mass injection, high unequal mass value has recovered, which highlights the effect of the degeneracy between mass, spin, and tidal parameters and shows the importance of employing tidal models even for soft EOS injection at SNR 32. For injection with the unequal mass system with no spin, the posteriors of spin parameter χ_{eff} are shifted towards high value for the injection with EOS APR4 while towards a lower value for BBH injection (right panel of Fig. 5.7). The results are broadly consistent with the earlier findings that we discussed in Sec. 5.1.

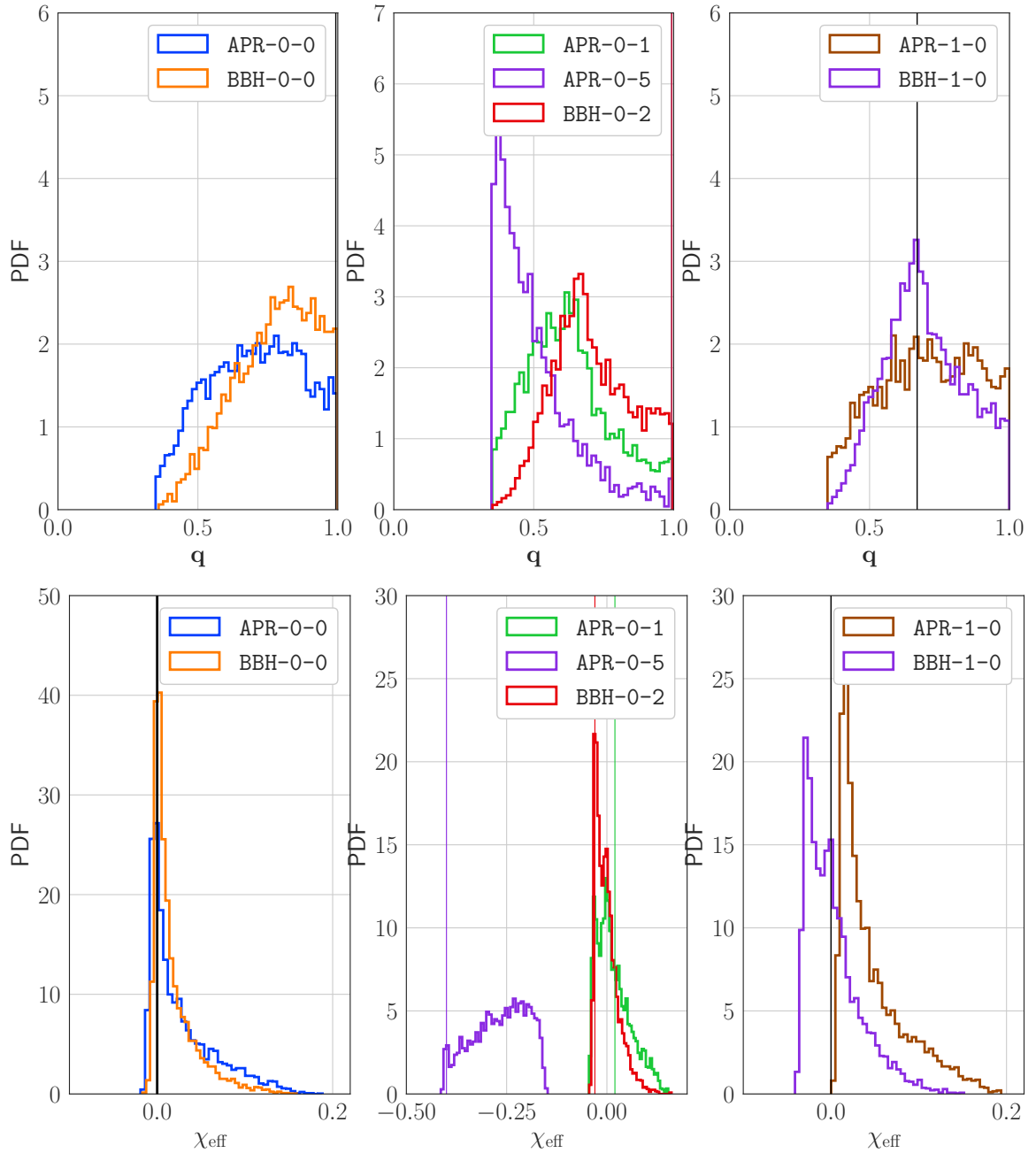


Figure 5.8: Marginalized PDF of q in top panel and χ_{eff} in bottom panel for IMRPhenomPv2 model using the high-spin prior $|\chi| \leq 0.89$. The injected parameter shown by the solid vertical line. Left panel: Approximately equal mass and non-spinning system, injection APR-0-0 and BBH-0-0 as listed in the Tab. 5.2 . Middle panel: Approximately equal mass and spinning system APR-0-1, APR-05 and BBH-0-2 injection scenarios. Right panel: Unequal mass and non-spinning system, APR-1-0 and BBH-1-0.

Chapter 6

Improving the waveform models

In the last chapter, we discussed the systematic differences among the various waveform models. We found out that few of these models are giving biased results for some particular injection scenarios due to differences in the physics included in these models. In this chapter, we present improvements in some of these models based on our earlier investigations. We review the findings of [Dudi2] and discuss the improved point-mass baseline of the `TaylorF2` model at quasi 5.5 PN order; we abbreviate this approximant as `TaylorF2pseudo5.5PN`. We analyze its accuracy by comparing gauge-invariant dimensionless quantity \mathcal{Q}_ω with EOB models. We also employ this model for GW parameter estimation and compare the results with other generally used waveform models like `TaylorF2Tides`, `IMRPhenomD_NRTidal` for the same setup. We also briefly comment upon the improved `NRTidal` model, `NRTidalv2`, introduced in Ref. [Dudi4]. In the later section, we review the surrogate modeling techniques that could be employed to construct a fast, compact, and accurate waveform model in the place of accurate but slow models. We present the results for the same in the context of the multipolar `TEOBResum` model [Dudi7].

6.1 TaylorF2 at quasi 5.5 post Newtonian

As we have already discussed in Chapter 5 [Dudi1] and also other systematics studies such as [26] have stressed the fact how $\tilde{\Lambda}$ estimates can be biased due to approximate treatment of physics in different waveform models and how important is to have more precise and fast to compute waveform models. Particularly, Favata et al. [25] investigated that how the bias incurs in the measurement of tidal deformability due to the truncation of the PN series, neglecting spins of the NS and orbital eccentricity. All these studies impress upon the fact that the tidal deformability, masses, and spin measurements will be biased if the systematics are not adequately addressed. After the `NRTidal` models became available, the most common practice to generate BNS inspiral is to augment the standard point-mass model with an additional tidal phasing. Thus, one primary source of systematics in BNS inspiral wave-

forms resides in the description of the non-tidal part, i.e., in the point-mass model (see, e.g., [126]). Therefore, a natural step is to improve the accuracy of the BNS inspiral the point-mass PN approximant beyond the current available. A point-mass (non-spinning) frequency-domain `TaylorF2` phasing approximant at quasi- 5.5 PN accuracy for the GWs from coalescing compact binaries is given in Ref. [127] [Dudi2] and also discussed in Appendix A. The new approximant, `TaylorF2pseudo5.5PN`, is obtained by Taylor-expanding the EOB resummed energy and angular momentum flux along circular orbits with all the known test-particle information up to 5.5 PN. The -yet uncalculated- terms at 4 PN order and beyond entering both the energy flux and the energy are taken into account as free parameters and then set to zero. It delivers a phasing representation that improves the currently known 3.5 PN one. We show that, in parameter estimation studies, the new phasing description allows one to strongly reduce the biases in the recovery of the tidal parameters that are usually present with the 3.5 PN `TaylorF2` point-mass (Sec. 6.1.2).

6.1.1 Q_ω analysis

We investigate the performance of `TaylorF2` at quasi 5.5 PN by comparing the Q_ω functions with the full EOB phasing and taking the differences, similarly to what was done in Ref. [Dudi3] for isolating the tidal part of the EOB phasing. The dimensionless quantity Q_ω is given by:

$$\frac{d^2\Psi}{d^2\hat{f}} = \frac{Q_\omega(\hat{f})}{\hat{f}^2}, \quad (6.1)$$

where Ψ is the GW phase and $\hat{f} \equiv Mf \equiv \Omega/2\pi$. This quantity is useful for comparing models as its inverse provides a measure which tells up to what extent stationary phase approximation (SPA) holds and gives a good approximation to the exact Fourier transform of the complete inspiral waveform. Moreover, it is independent of an arbitrary shift of time and phase that affects the GW phase. In Fig. 6.1, we compare point-particle (non-spinning) orbital phasing for the EOB and the PN curves for the $q = 1$ case. We show the differences between the EOB and PN ($Q_\omega^{\text{EOB}} - Q_\omega^{\text{PN}}$) at quasi 5.5 PN (*red curve*) and 3.5 PN (*blue curve*). The top panel of the figure illustrates the full phasing acceleration evolution, up to the peak of the EOB orbital frequency that is identified with the merger. The bottom panel is a close up on the inspiral part. The vertical lines corresponds (from left to right) to 10 Hz, 20 Hz, 718 Hz and 1024 Hz for a fiducial equal-mass BNS system with $(1.35 + 1.35)M_\odot$. The 718 Hz line corresponds to $\hat{\omega} = 0.06$, (where $\hat{\omega}$ is the dimensionless GW orbital frequency) that roughly corresponds to the NR contact frequency [81].

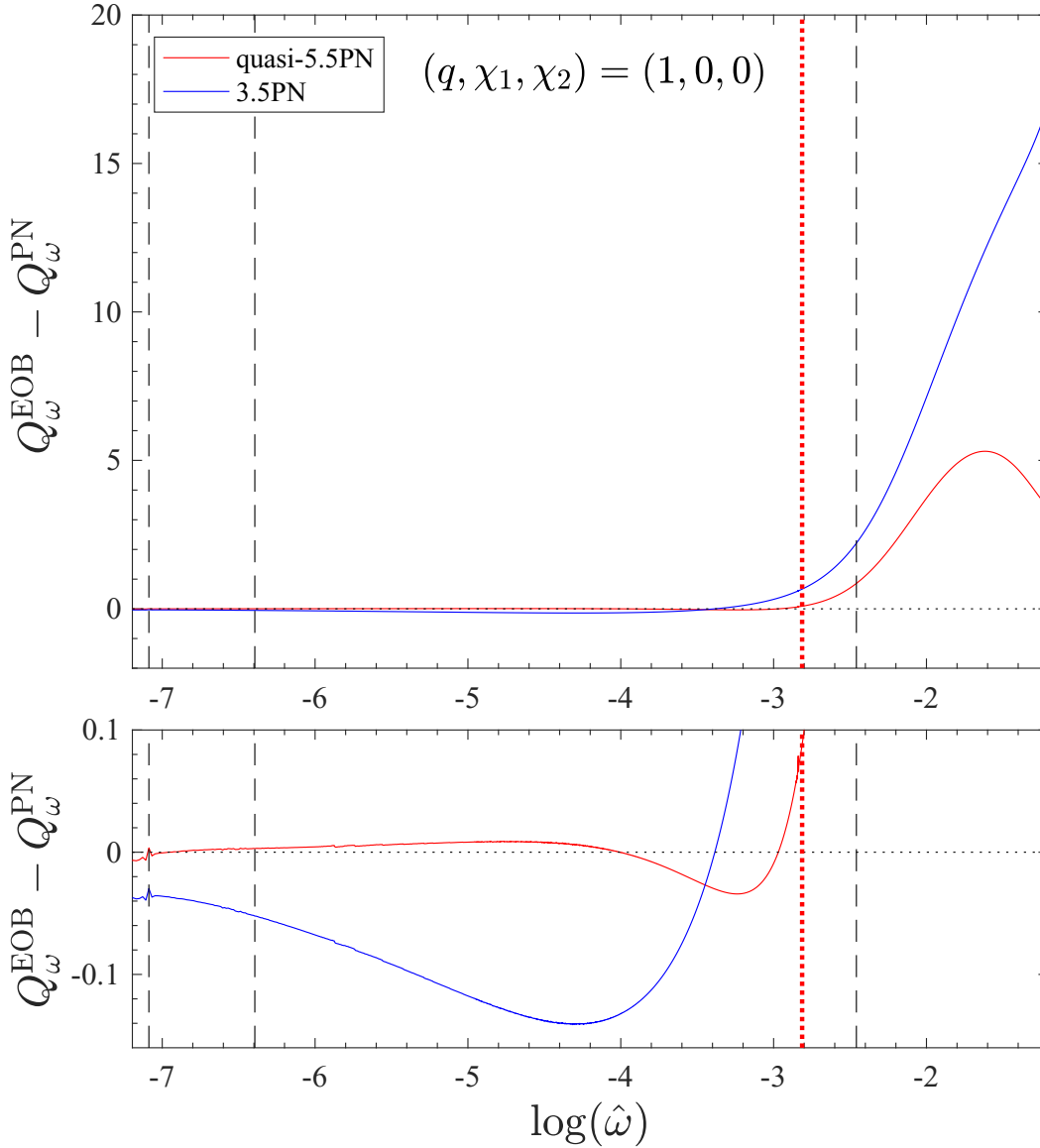


Figure 6.1: Figure depicts the difference between Q_{ω} quantity for EOB and PN at quasi 5.5 PN and 3.5 PN for $q = 1$ case, up to (approximate) merger time. The vertical lines mark the 10 Hz, 20 Hz, 718 Hz or 1024 Hz for a $(1.35 + 1.35)M_{\odot}$ binary. The differences in EOB and quasi-5.5 PN curve is always much closer to the zero than the standard 3.5 PN approximant. The plot is taken from [Dudi2].

The figure highlights that the quasi-5.5 PN approximant delivers a rather good representation of the point-mass EOB phasing precisely up to $\hat{\omega} = 0.06$. Tab. 6.1 reports the phase difference

$$\Delta\phi_{(\hat{\omega}_0, \hat{\omega}_1)} = \int_{\hat{\omega}_0}^{\hat{\omega}_1} \Delta Q_{\omega} d \log \hat{\omega} , \quad (6.2)$$

accumulated between the frequencies $[\hat{\omega}_0, \hat{\omega}_1]$ (or equivalently $[f_0, f_1]$ in physical units) marked by vertical lines in the plots. The numbers in the table illustrate quantitatively how the 5.5 PN phasing approximant delivers a phasing description that is, by itself, more EOB compatible than the standardly used 3.5 PN one. Note that this is

Table 6.1: EOB/PN phase difference accumulated between $[f_0, f_1]$. It is obtained by integrating the $\Delta Q_\omega^{\text{EOBPN}}$ s in Fig. 6.1 between the corresponding values of $\log(\hat{\omega})$. The limits of integration are denoted in Hz as we want to ideally refer to the fiducial $(1.35 + 1.35)M_\odot$ binary system. The table is taken from [Dudi2].

$\hat{\omega}_0 \times 10^4$	$\hat{\omega}_1$	f_0 [Hz]	f_1 [Hz]	$\Delta\phi_{3.5\text{PN}}^{\text{EOBPN}}$	$\Delta\phi_{5.5\text{PN}}^{\text{EOBPN}}$
8.35	0.086	10	1024	0.2718	0.1364
8.35	0.060	10	718	-0.1916	1.45×10^{-3}
16.7	0.086	20	1024	0.3009	0.1354
16.7	0.060	20	718	-0.1625	4.54×10^{-4}
20.0	0.086	24	1024	0.3110	0.1348

achieved even if the EOB incorporates the effective, NR-informed, $a_c^6(\nu)$ parameter, that is not included in the TaylorF2 approximant.

6.1.2 Effect on $\tilde{\Lambda}$ inference

To study the implication of changing the PN-accuracy of the point-mass baseline on the estimate of the tidal deformability parameter $\tilde{\Lambda}$, we inject full BNS waveform and recover it using TaylorF2pseudo5.5PN. We construct equal-mass EOBNR hybrid BNS waveforms by matching the TEOBResumS EOB tidal model [77] to state-of-the-art NR simulations of the CoRe collaboration [Collab3] as discussed in Chapter 4. Note that the version of TEOBResumS used here does not incorporate the analytical developments of Refs. [128, 129]. Two fiducial waveforms are considered here corresponding to two non-spinning, equal-mass $(1.35M_\odot + 1.35M_\odot)$ BNS models described by the SLy and H4 EOS. The corresponding values of the tidal parameters are $\tilde{\Lambda} = 392.231$ (SLy EOS) and $\tilde{\Lambda} = 1110.5$ (H4 EOS). The waveforms are injected at SNR of 30 and 100 into a fiducial data stream of the LIGO detectors [15]. We assume the projected noise curve for the Advanced LIGO detectors in the zero-detuned high-power configuration (ZDHP) [130] and no actual noise is added to the data. Rest setup for parameter estimation was identical to the Ref. [Dudi1]. The injected waveform is recovered with three approximants: (i) IMRPhenomD_NRTidal, where the point-mass orbital phasing is obtained by a suitable representation of hybridized EOB/NR BBH waveforms, the PhenomD approximant [87]; (ii) TaylorF2Tides where the 3.5 PN orbital phase is augmented by the 6 PN (next-to-leading) tidal phase [90]; (iii) the same as above where the 3.5 PN orbital, non-spinning, phase is replaced by the quasi-5.5 PN one. The models are described in detail in Chapter 3. The LALInference package [45]) is then employed to extract the binary properties from the signal. We use a uniform prior distribution in the interval $[1M_\odot, 3M_\odot]$ for the component masses, and a uniform prior between -1 and 1 for both dimensionless aligned spins. We also pick a uniform prior distribution for the individual tidal parameters $\Lambda^{A,B}$ between 0 and 5000. The posteriors obtained for two injections from three waveform models are presented in the left panel for the SLy EOS and right

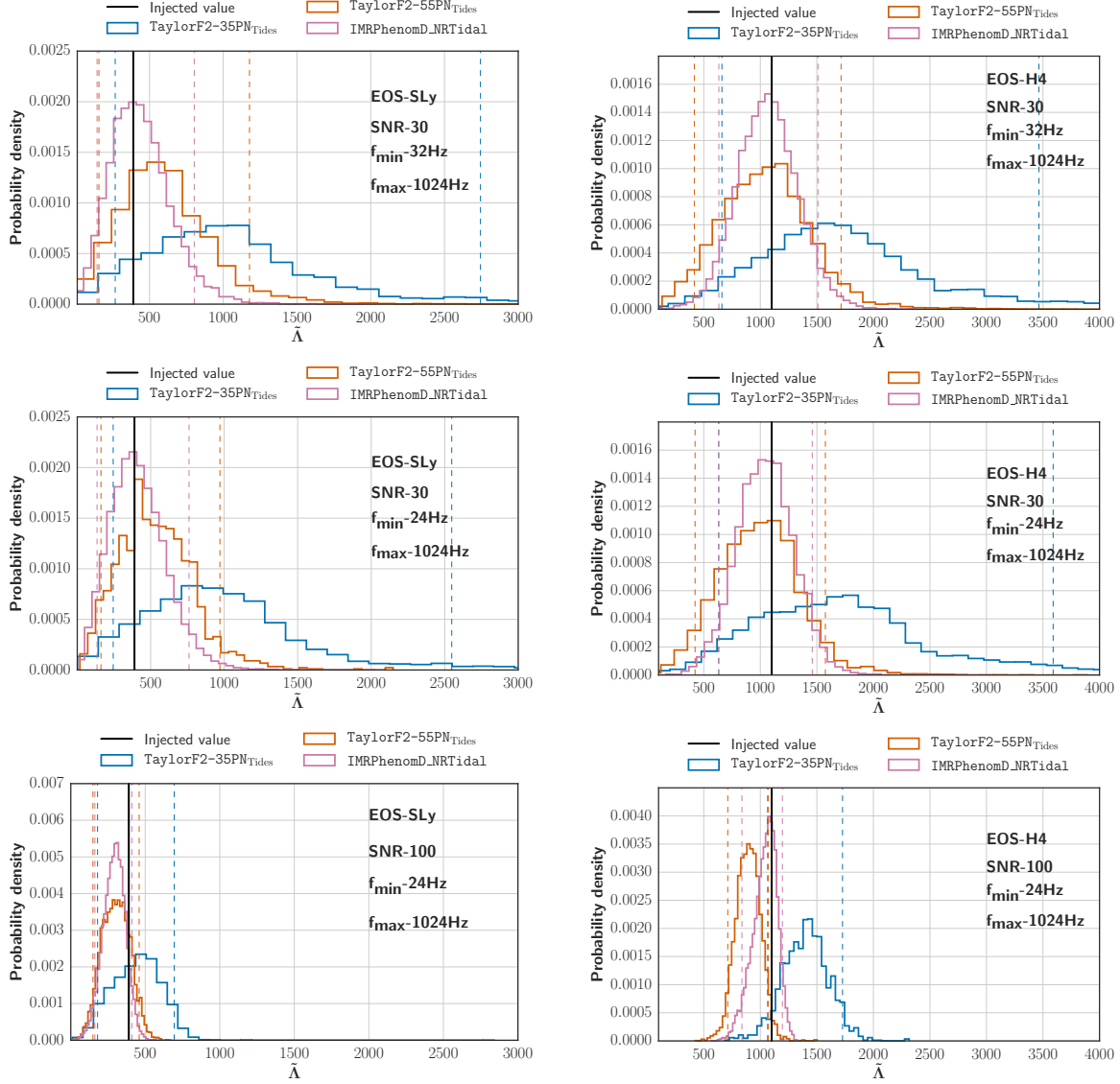


Figure 6.2: Posteriors obtained for tidal deformability $\tilde{\Lambda}$ from different waveform model on different frequency intervals $[f_{\min}, f_{\max}]$ with different SNR. The injected waveforms have $1.35M_{\odot} + 1.35M_{\odot}$ binary with SLy EOS (*left panel*) and with H4 EOS (*right panel*). The vertical line corresponds to the injected value $\tilde{\Lambda}^{\text{SLy}} = 392.2$ (*left*) and $\tilde{\Lambda}^{\text{H4}} = 1110.5$ (*right*). Irrespectively of the value of SNR, the 3.5 PN baseline introduces a strong bias (and spread) in the measure of $\tilde{\Lambda}$. By contrast, this is practically reabsorbed when using the quasi-5.5PN point-mass baseline. The dashed vertical lines correspond to a 90% confidence level. The plot is taken from [Dudi2].

Table 6.2: Data behind Fig. 6.2. For each measured quantity, chirp mass \mathcal{M} , symmetric mass ratio ν and tidal polarizability $\tilde{\Lambda}$, the columns report: the injected value; the minimum value of frequency considered, either 24Hz or 32Hz; the combination EOS-SNR; finally, the last three columns list the median values measured with the three different waveform approximants with the 90% credible interval. The last row of the table shows the average waveform generation time for each approximant, assuming starting frequency of 24Hz. The table is taken from [Dudi2].

	Injected Value	f_{\min}	EOS	SNR	TaylorF2 3.5PN	TaylorF2 5.5PN	IMRPhenomD_NRTidal
\mathcal{M}	1.1752	24 Hz	Sly	30	1.1753 ^{1.1755} _{1.1752}	1.1753 ^{1.1755} _{1.1752}	1.1753 ^{1.1755} _{1.1752}
			H4	30	1.1753 ^{1.1755} _{1.1752}	1.1753 ^{1.1755} _{1.1752}	1.1753 ^{1.1755} _{1.1752}
			Sly	100	1.1753 ^{1.1754} _{1.1752}	1.1753 ^{1.1754} _{1.1752}	1.1753 ^{1.1754} _{1.1752}
			H4	100	1.1753 ^{1.1754} _{1.1752}	1.1753 ^{1.1754} _{1.1752}	1.1753 ^{1.1754} _{1.1752}
		32 Hz	Sly	30	1.1754 ^{1.1757} _{1.1752}	1.1754 ^{1.1757} _{1.1752}	1.1754 ^{1.1756} _{1.1752}
			H4	30	1.1754 ^{1.1756} _{1.1751}	1.1754 ^{1.1757} _{1.1751}	1.1753 ^{1.1756} _{1.1751}
			Sly	30	0.24640 ^{0.24996} _{0.23147}	0.24558 ^{0.24995} _{0.23135}	0.24636 ^{0.24997} _{0.23105}
			H4	30	0.24729 ^{0.24997} _{0.2338}	0.24581 ^{0.24995} _{0.23162}	0.24590 ^{0.24996} _{0.23079}
ν	0.25	24 Hz	Sly	100	0.24857 ^{0.24998} _{0.23744}	0.24738 ^{0.24995} _{0.23691}	0.24703 ^{0.24998} _{0.23292}
			H4	100	0.24877 ^{0.24997} _{0.24083}	0.24735 ^{0.24995} _{0.23694}	0.24702 ^{0.24997} _{0.23307}
			Sly	30	0.24658 ^{0.24996} _{0.23107}	0.24670 ^{0.24997} _{0.23247}	0.24592 ^{0.24997} _{0.23054}
			H4	30	0.24684 ^{0.24997} _{0.23282}	0.24605 ^{0.24995} _{0.23194}	0.24576 ^{0.24996} _{0.23051}
		32 Hz	Sly	30	935.91 ^{2547.71} _{245.40}	517.88 ^{971.32} _{162.29}	400.47 ^{761.30} _{135.47}
			H4	30	1690.56 ^{3589.6} _{832.12}	987.29 ^{1575.33} _{422.78}	1044.27 ^{1459.18} _{630.88}
			Sly	100	452.24 ^{694.52} _{180.44}	301.87 ^{459.52} _{149.57}	295.21 ^{410.31} _{162.62}
			H4	100	1405.42 ^{1726.90} _{1065.20}	894.93 ^{1069.01} _{711.92}	1051.61 ^{1195.12} _{837.18}
$\tilde{\Lambda}$	392	24 Hz	Sly	30	1007.47 ^{2743.87} _{267.25}	572.29 ^{1177.84} _{156.79}	419.89 ^{803.14} _{144.15}
			H4	30	1675.67 ^{3464.08} _{660.31}	1042.61 ^{1713.99} _{416.23}	1060.44 ^{1509.45} _{633.25}
		32 Hz	Sly	30	1007.47 ^{2743.87} _{267.25}	572.29 ^{1177.84} _{156.79}	419.89 ^{803.14} _{144.15}
			H4	30	1675.67 ^{3464.08} _{660.31}	1042.61 ^{1713.99} _{416.23}	1060.44 ^{1509.45} _{633.25}
Average Time					22.9 ms	32.68 ms	60.13 ms

panel for the H4 EOS of Fig. 6.2. We compare the inference of the tidal parameter done on two frequency intervals, [24, 1024] Hz and [32, 1024] Hz. Note that we do not extend the analysis interval to higher frequencies because of we know that the orbital part of the TaylorF2 approximants becomes largely inaccurate at such frequencies. For SNR = 30, one finds that the 3.5 PN orbital baseline induces a clear bias in $\tilde{\Lambda}$, while the quasi-5.5 PN one agrees much better with the IMRPhenomD model as well as the injected value (vertical line in the plots). Incrementing the SNR to 100, the statement only holds for the softer EOS, since for the H4 case also the 5.5 PN approximant is biased, although still less than the 3.5 PN one. The two figures are complemented by Tab. 6.2, that, for each choice of configuration and SNR, lists the recovered values with their 90% credible interval. The last row of the table also reports the time needed to generate a single waveform: interestingly, the timing of the quasi-5.5PN TaylorF2 is comparable to the one of the 3.5 PN approximant, i.e., it remains approximately *two times faster* than IMRPhenomD_NRTidal being consistent with this latter at SNR $\lesssim 30$. This suggests that, for events similar to GW170817 or quieter, the quasi-5.5 PN TaylorF2 can effectively be used in place of IMRPhenomD_NRTidal to get an even faster, yet accurate, estimate of the parameters.

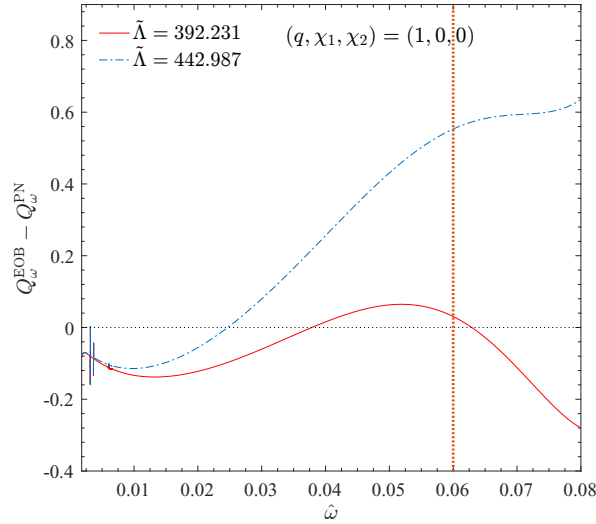


Figure 6.3: Heuristic explanation of the bias on $\tilde{\Lambda}$: $1.35M_{\odot} + 1.35M_{\odot}$ binary, Sly EOS, $\tilde{\Lambda} = 392.231$. Shown is the gauge-invariant difference $\Delta Q_{\omega}^{\text{EOBPN}} \equiv Q_{\omega}^{\text{EOB}} - Q_{\omega}^{\text{PN}}$ between the EOB Q_{ω} and the PN Q_{ω} with the 3.5 PN orbital baseline augmented by the 6 PN-accurate tidal phase. Increasing the value of the tidal parameter to $\tilde{\Lambda} = 442.987$ is very effective in reducing the phase difference accumulated between in the interval $\omega \in [0.02, 0.06]$ (dotted vertical line) to a negligible value. Such $\hat{\omega}$ interval corresponds to $f \in [24, 718]$ Hz for this binary. The upper frequency limit corresponds to 957.4 Hz. The plot is taken from Ref. [Dudi2].

Understanding waveform systematics of the injections via the Q_{ω} analysis

Here, we try to heuristically explain why the effect of the 3.5 PN-accurate orbital baseline is to bias the value of $\tilde{\Lambda}$ towards values that are larger than the theoretical expectation as can be seen in Figs. (6.2, 5.3). Assessing Fig. 6.1, one can notice that the $Q_{\omega}^{\text{EOB}} - Q_{\omega}^{\text{3.5PN}}$ is negative. This indicates that the PN phase accelerates *less* than the EOB one, i.e., the inspiral occurs *more slowly* in the 3.5 PN phasing description than in the EOB. We could think of it as that the gravitational interaction behind the 3.5 PN-accurate orbital phasing is *less attractive* as compared to what predicted by the EOB model. This effect might be compensated by an additional part in the total PN phasing that stems from a part of the dynamics that is intrinsically *attractive*, and that could compensate for the inaccurate behavior of the 3.5 PN. Since eventually, the phase difference is given by an integral, two effects of the opposite sign can mutually compensate and thus generate a PN-based frequency phase that is compatible with the EOB. Since tidal interactions are attractive, the corresponding part of the phasing is naturally able to compensate for the repulsive character of the orbital phasing. For this compensation to be adequate, it may happen that $\tilde{\Lambda}$ has to be *larger* than the theoretically correct one that accounts for the tidal interaction (at leading order) in the EOB waveform.

Such intuitive explanation can be tested by performing Q_ω analysis. Fig. 6.3 shows the comparison between two EOB-PN Q_ω differences $\Delta Q_\omega^{\text{EOBPN}} \equiv Q_\omega^{\text{EOB}} - Q_\omega^{\text{PN}}$, where the Q_ω^{EOB} is the complete function, while Q_ω^{PN} is obtained by summing together the 3.5 PN orbital phase and the 6 PN-accurate tidal phase [32]. When we use the theoretically correct value of $\tilde{\Lambda} = \Lambda_1 = \Lambda_2 = 392.231$ for the SLy model with masses $1.35M_\odot$ each, the phase difference in the interval $\hat{\omega} \in [\hat{\omega}_0, \hat{\omega}_1] = [0.002, 0.06]$, corresponding to $f \in [20, 718]$ Hz (dotted vertical line in the figure) for this binary, is $\Delta\phi_{(\hat{\omega}_0, \hat{\omega}_1)} \simeq -0.276$ radian. By contrast, if the value of $\tilde{\Lambda}$ is progressively increased, the accumulated phase difference between $[\hat{\omega}_0, \hat{\omega}_1]$ gets reduced up to $\Delta\phi_{(\hat{\omega}_0, \hat{\omega}_1)} \simeq 2.429 \times 10^{-4}$ for $\tilde{\Lambda} = 442.987$. Note however that such analytically predicted “bias” in $\tilde{\Lambda}$ depends on the frequency interval considered: if we extended the integration up to $\hat{\omega}_1 \simeq 0.08$ (corresponding to 957.4 Hz) one finds that a similarly small accumulated phase difference $\Delta\phi_{0.002, 0.08} \simeq 5.0 \times 10^{-5}$ is obtained for $\tilde{\Lambda} = 424.08$, i.e. the analytical bias is *reduced*. This fact looks counterintuitive: a result obtained with a PN approximant is not, a priori, expected to improve when including higher frequencies. By contrast, the fact that the analytic bias is (slightly) reduced increasing $\hat{\omega}_1$ illustrates the *lack of robustness* as well as the *lack of predictive power* of the approximant in the strong-field regime. Generally speaking, one sees that the combination of 3.5 PN orbital phase with 6 PN tidal phase may result in a waveform that is *effectual* with respect to the EOB one, in the sense that the noise-weighted scalar product will be of the order of unity, but with an incorrect value of the tidal parameter. This simple example is helpful to intuitively understand how the incorrect behavior of the point-mass non-spinning phasing can eventually result in a bias towards larger values of $\tilde{\Lambda}$. Interestingly, this value is close to the value obtained with SNR=100 (see left-bottom panel of Fig. 6.2). Although the analysis of Fig. 6.3 certainly cannot replace an injection-recovery study; it should be kept in mind as a complementary tool to interpret its outcome within a simple, intuitive, but a quantitative framework.

In summary, we introduce a new approximant `TaylorF2pseudo5.5PN` and check its faithfulness by comparing it with EOB model (`TEOBResumS`) via Q_ω analysis and by performing parameter estimation analysis. We also try to intuitively explain the behavior of `TaylorF2Tides` model that deviates from the expected value and provides an upper bound on $\tilde{\Lambda}$ estimates as found in Refs. [Dudi1, Collab1]. We have also compared various truncation of 5.5 PN approximants such as (3.5, 4, 4.5, 5, 5.5)-PN with complete EOB point mass phasing via Q_ω analysis and found that the 5.5 PN phasing is remarkably close to the EOB phasing. Therefore, we recommend the use of the quasi 5.5 PN approximant in searches as well as in parameter estimation of GWs. This approximant could be further improved at higher frequencies by tuning some of the free parameters (given in Appendix A), which are set to zero for the time being. For further details, we refer to Ref. [Dudi2].

6.2 NRTidalv2 model

NRTidal model is a frequency as well time domain model of tidal phase that can be augmented to any point-mass baseline. The NRTidal model is based on the idea discussed in Section 3.4. The phase of the GW is approximated as a sum of the various contribution from point-mass baseline, spin, tides, etc., given in Eq. (6.3). The tidal phase then parametrized by effective tidal coupling constant κ_{eff} , given in Eq. (3.22) and fitted over the known NLO tidal contribution at low frequencies Eq. (3.23) and tuned to EOB and NR data at high frequencies. However, studies in Refs. [Dudi1, Dudi3] (discussed in Sec. 4.1 and 5.1) showed that the NRTidal model might overestimate the tidal effects and underestimate the $\tilde{\Lambda}$ at large SNRs and/or for stiff EOS. Therefore, it is crucial to improve this model so that a fast and accurate waveform remains available for upcoming detections. We call the improved model NRTidalv2. We describe the improvements that are made in NRTidalv2 [Dudi4], with respect to the old NRTidal approximant.

- The closed-form phenomenological tidal description has been recalibrated using higher-order analytical knowledge and improved NR data. This approximant is based on the following assumption for GW phase:

$$\psi(\hat{\omega}) \approx \psi_{PP}(\hat{\omega}) + \psi_{SO}(\hat{\omega}) + \psi_{SS}(\hat{\omega}) + \psi_T(\hat{\omega}), \quad (6.3)$$

where $\psi(\hat{\omega})$ denotes the point particle contribution to the phase, $\psi_{SO}(\hat{\omega})$ and $\psi_{SS}(\hat{\omega})$ denotes spin-orbit and spin-spin contribution respectively and contribution from the tidal effects is denoted by $\psi_T(\hat{\omega})$ in frequency domain. Similarly like NRTidal, the $\psi_T(\hat{\omega})$ is based on Eq. (3.25). Although, here we employ the known analytical knowledge upto 7.5 PN instead 6 PN. Thus, the improved version of Eq. (3.25):

$$\phi_T(x) = -\kappa_{\text{eff}}^T \frac{13}{8\nu} x^{5/2} P_{\text{NRTidalv2}}(x), \quad (6.4)$$

where ϕ_T is the time domain phase. Now, with the Padé approximant

$$P_{\text{NRTidalv2}}(x) = \frac{1 + n_1 x + n_{3/2} x^{3/2} + n_2 x^2 + n_{5/2} x^{5/2} + n_3 x^3}{1 + d_1 x + d_{3/2} x^{3/2} + d_2 x^2}. \quad (6.5)$$

Then SPA, discussed in, e.g., [131], is employed to derive the tidal phase contribution ψ_T in the frequency domain:

$$\psi_T(x) = -\kappa_{\text{eff}}^T \frac{39}{16\nu} x^{5/2} \tilde{P}_{\text{NRTidalv2}}(x), \quad (6.6)$$

with

$$\tilde{P}_{\text{NRTidalv2}}(x) = \frac{1 + \tilde{n}_1 x + \tilde{n}_{3/2} x^{3/2} + \tilde{n}_2 x^2 + \tilde{n}_{5/2} x^{5/2} + \tilde{n}_3 x^3}{1 + \tilde{d}_1 x + \tilde{d}_{3/2} x^{3/2} + \tilde{d}_2 x^2}, \quad (6.7)$$

We refer the reader to the Ref. [Dudi4] for the details about the coefficients.

- As another improvement, in NRTidalv2 tidal GW amplitude A^{NRTidal} correction to the model has been added. Using the 6 PN tidal correction to amplitude as a starting point:

$$\tilde{A}_T^{6\text{PN}} = \sqrt{\frac{160\pi\nu}{27}} \frac{M^2}{D_L} \kappa_{\text{eff}}^T x^{-7/4} \left(-\frac{27}{16} x^5 - \frac{449}{64} x^6 \right), \quad (6.8)$$

where D_L is the luminosity distance.

The amplitude correction is:

$$\tilde{A}_T^{\text{NRTidalv2}} = -\sqrt{\frac{5\pi\nu}{24}} \frac{9M^2}{D_L} \kappa_{\text{eff}}^T x^{13/4} \frac{1 + \frac{449}{108} x + \frac{22672}{9} x^{2.89}}{1 + d x^4}. \quad (6.9)$$

where $d = 13477.8$ is the fitting coefficient.

- EOS dependent 3.5 PN spin-spin effects and 3 PN cubic in spin effects which are proportional to the quadrupole and octopole moment of the NS are also incorporated.

Table 6.3: The non-spinning BNS and BBH hybrids employed in the construction of the NRTidal model. The columns refer to the name, the employed EOS, the individual masses of the stars M_A , M_B , the tidal deformabilities Λ^A, Λ^B , the tidal coupling constant κ_{eff}^T [Eq.3.22], and the ID in the CoRe and SXS databases. The table is taken from Ref. [Dudi4].

Name	EOS	M_A	M_B	Λ_A	Λ_B	κ_{eff}^T	ID
SLy	SLy	1.350	1.350	392.1	392.1	73.5	CoRe:BAM:0095 ¹
H4	H4	1.372	1.372	1013.4	1013.4	190.0	CoRe:BAM:0037
MS1b	MS1b	1.350	1.350	1389.4	1389.4	288.1	CoRe:BAM:0064
BBH	-	1.350	1.350	0	0	0	SXS:BBH:0066

For NRTidal model, PN, EOB, and NR approximants have been separately used in different frequency intervals for calibration. Here, we fit the coefficients using hybrid waveforms, starting at the frequency 20 Hz, constructed by employing a time-domain tidal EOB model (TEOBResumS) to cover inspiral regime [77] connected to a high resolution NR simulation. The hybridization is done, as discussed in Chapter 4. In addition to the BNS hybrid waveforms, we also create a hybrid between the non-tidal version of the TEOBResumS model and a binary black hole waveform computed with the SpEC code [132]; setup SXS:BBH:0066 of the public SXS catalog [133, 134]. The phase evolution of the time domain hybrid waveforms, listed in Tab. 6.3, are shown in Fig. 6.4 in the top panel. We also present the phase difference between the

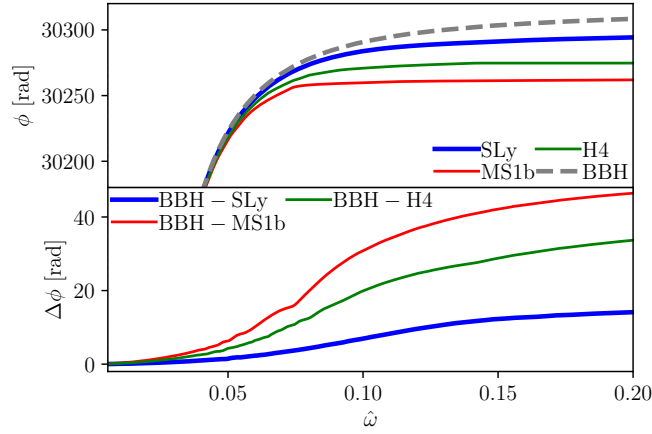


Figure 6.4: Time domain phase of the hybrid waveforms employed to develop NRTidal. The bottom panel shows the phase difference caused by tidal effects. The plot is taken from Ref. [Dudi4].

BBH hybrid and BNS hybrids in the bottom panel. To compute the phase difference, we first align the hybrid waveforms at ~ 22 Hz. We find that in the last ~ 5000 GW cycles (3×10^4 rad) the phase difference caused by tidal effects is only ~ 12 rad at the merger frequency of our BNS setup. Again, we emphasize that only the four hybrid waveforms listed in Tab. 4.1 are used for calibration of the NRTidalv2 model, where the dataset we are going to fit is

$$\begin{aligned}
 \phi_T^{\text{NR}} &= \frac{1}{320 + 192 + 192} \left[320(\phi_{\text{SLy}} - \phi_{\text{BBH}}) + 192(\phi_{\text{H4}} - \phi_{\text{BBH}}) \right. \\
 &\quad \left. + 192(\phi_{\text{MS1b}} - \phi_{\text{BBH}}) \right] \\
 &= \frac{1}{11} \left(5\phi_{\text{SLy}} + 3\phi_{\text{H4}} + 3\phi_{\text{MS1b}} - 11\phi_{\text{BBH}} \right).
 \end{aligned} \tag{6.10}$$

The factors are obtained by linearly weighting the resolutions of the individual NR data, i.e., 320 points across the star for the SLy setup and 192 for H4 and MS1b setups. We decided to use this minimal dataset since these are the available data with the highest accuracy. Note that a simple restriction to the highest resolution, i.e., the SLy data, leads to a phase description which does not accurately characterize binaries with large tidal deformabilities. Thus, it would be preferable to include in the future a larger number of NR simulations with varying masses, spins, mass ratios, and EOSs once these are available. However, while there are a small number of high-quality waveforms [135], these waveforms do not span a sufficiently large region of the parameter space to incorporate additional mass ratio, EOS, or mass dependencies in our phenomenological ansatz. For assessing the accuracy of the NRTidalv2 model, we used 18 hybrids listed in Tab. 4.1. We used IMRPhenomPv2 augmented to NRTidalv2 as a full waveform for the assessment. We compute the mismatch between the IMRPhenomPv2_NRtidalv2 model and hybrids. We used the Advanced LIGO zero-detuning high-power (ZDHP) noise curve for our analysis with

$f_{\min} = 30$ Hz and a variable f_{\max} ranging from 500 Hz to merger frequency f_{mrg} and found the mismatches are below 5×10^{-3} for all cases. We also compute the time domain phase difference of IMRPhenomPv2NRtidalv2 with NR data from the CoRe database and found agreement within the estimated uncertainty. Overall, we found that the performance of the NRTidalv2 model is comparable to the state-of-the-art tidal EOB model.

6.3 Surrogate Model

We have emphasized the importance of accurate and fast to evaluate waveform models, e.g. in Sec. 2.3, in the context of extracting the source properties of the signal. Waveform models employ for parameter estimations are discussed in chapter 3. The PN based models which are fast-to-evaluate than any other models, unfortunately, are not accurate upto the merger and could potentially bias the measured parameters [Dudi1]. On the other hand, waveforms constructed under EOB formalism (discussed in Sec. 3.2) are able to precisely describe the compact binaries upto the merger and beyond for black hole binaries. However, they are slow to be used for parameter estimation. A possible solution to this problem was introduced in Ref. [136] and is called reduced-order modeling or surrogate modeling. These methods provides a compact, accurate and fast-to-evaluate model in place of an accurate but slow to evaluate model. First, we briefly review the reduced-order-modeling techniques introduced in Ref. [83, 136] and refer these articles for detailed discussion. Then, we present their implementation for the time domain tidal EOB model -TEOBResum and show results for higher-multipoles upto ($\ell = 4, m = 4$). Later we briefly discuss how these techniques can be used for spin-tidal EOB model - TEOBResumS [77]. The publication is in preparation, and results are not fully matured yet. The TEOBResum waveform is described by 7 input parameters (θ), namely, mass-ratio q , and the tidal deformability of the two satrs, upto ($\ell = 2, 3$, and 4) tidal multipole moments. i.e., $\theta = (q, \Lambda_2^A, \Lambda_2^B, \Lambda_3^A, \Lambda_3^B, \Lambda_4^A, \Lambda_4^B)$. We work in total mass rescaled units here. These 7 dimensional space can be reduced to 3 dimensions by using Yagi fits that correlates $\ell = 2$ tidal parameter to $\ell = 3, 4$ tidal parameters [137]. Systematic uncertainty due to the fits has been studied in the Appendix A of Ref. [83] for few cases. First, for building a surrogate model, one requires a set of precomputed waveforms (training set). These data set has to be preconditioned such that it varies as smoothly as possible with parameters. For constructing the training set for multipolar TEOBResum model, we follow Ref. [83] and choose the waveform parameters as:

$$\theta := (q, \Lambda_A, \Lambda_B), \quad (6.11)$$

and the parameters are in range $q \in [0.5, 1]$ and $\Lambda_2^{A,B} = [50, 5000]$. We build the surrogate model for amplitude A and phase ϕ independently, but over the same training

set as amplitude and phase vary less with parameters and time, than strain, and that results in a more accurate and compact model at the end. We choose the waveform parameter θ to discretize the parameter space at Chebyshev-Gauss-Lobatto nodes, as in later steps, we would like to perform the interpolation. For each parameter, we choose 16 nodes in the given range such that in total $16 \times 16 \times 16 = 4096$ waveforms are required to generate the training set. As mentioned above, preconditioning is needed for amplitude and phase to be a smooth function of the waveform parameter θ . For the same, we align all the waveforms at the peak amplitude, i.e., at the merger and shift the waveforms such that $t = 0$ corresponds to the merger time. We make them equal length by chopping off the beginning portions and then set the initial phase of all waveforms to zero. Then, we downsample the data to reduce the physical memory size. First we sample amplitude and phase in phase ϕ with a spacing $\Delta\phi = \pi$ before $t = -10^3 M$. Also, after that, in time with a spacing $\Delta t = 0.1M$ to get the complicate behavior near merger. After generating the training set, the next step is to build reduced basis to compress the data in time (or frequency) and parameters. We employ greedy algorithm to construct reduced basis. For details we refer the reader to Ref. [136] and the algorithm is discussed in Appendix B. The key idea is that if the amplitude $A(t, \theta)$ and phase $\phi(t, \theta)$ are given at a discrete set of training points (N , here $N = 4096$) or parameters, then greedy algorithm selects a smaller number ($n < N$) of parameters and corresponding amplitude and phase which constitutes the basis. Then, we use Gram-Schmidt process to get the orthogonal basis vectors $\{\mathbf{e}\}_i^n$. Once we have the basis then any amplitude and phase can be written in a linear combination of the basis vectors:

$$A(t, \theta) \approx \sum_i^{n_A} c_i^A(t) \mathbf{e}_i^A(t), \quad (6.12)$$

$$\phi(t, \theta) \approx \sum_i^{n_\phi} c_i^\phi(t) \mathbf{e}_i^\phi(t). \quad (6.13)$$

where the coefficients $c_i^A(t)$ and $c_i^\phi(t)$ are inner product of reduced basis and the amplitude and phase ². n_A and n_ϕ are number of basis, $\mathbf{e}_i^A(t)$ and $\mathbf{e}_i^\phi(t)$ are reduced basis for amplitude and phase respectively. Now, the next step is to reduce the data in time for that we build an *empirical interpolant* and choose few time nodes τ , defined uniquely for a reduced basis. Such that, if the waveform is known at those time nodes, it can be generated at any time by using the interpolant. This algorithm is also discussed in the Appendix B. The first time node τ_1 is a seed for the greedy algorithm and we choose the first time node as the time at which the first reduced basis is maximum in its absolute value: $\tau_1 = \arg \max_t |\mathbf{e}_1|(t)$. We use $\mathcal{I}_n[A](t, \theta)$ notation for the interpolant which indicates that the interpolant is a linear combination of first n reduced basis and its a function that acts on amplitude A ,

² $c_i^A(t) = \int \mathbf{e}_i^{*A}(t) A(t, \theta) dt$

similarly we can also write it for phase. The interpolant for $n = 1$ is given by:

$$\mathcal{I}_1[A](t, \theta) = C_1(\theta)\mathbf{e}_i^A(t), \quad (6.14)$$

the coefficient $C_1(\theta)$ is obtained by demanding that the interpolant generate the data at the node τ_1 i.e., $\mathcal{I}_1[A](\tau_1, \theta) = A(\tau_1, \theta)$. Then, Eq. (6.14) at τ_1 gives: $C_1(\theta) = A(\tau_1, \theta)/\mathbf{e}_1(\tau_1)$. And the interpolant is written as:

$$\mathcal{I}_1[A](t, \theta) = \mathbf{B}_1^A(\theta)A_i(\tau, \theta), \quad \text{where } \mathbf{B}_1^A = \mathbf{e}_1(t)/\mathbf{e}_1(\tau_1). \quad (6.15)$$

To compute the the second time node τ_2 , we interpolate the second reduced basis with the current interpolant and then the time sample at which it has the maximum error in absolute value will be the second time node τ_2 :

$$\tau_2 := \arg \max_t |\mathbf{e}_2(t) - \mathcal{I}_1[\mathbf{e}_2](t, \theta)| \quad (6.16)$$

Then, we write the interpolant for the next step as in Eq. (6.14),

$\mathcal{I}_2[A](t, \theta) = \sum_{i=1}^2 C_i(\theta)\mathbf{e}_i^A(t)$, and coefficients are again computed by demanding that at the second time node τ_2 the interpolant reproduce the data. Similarly, we can keep on iterating until all reduced basis are exhausted. We then have n empirical time nodes $(\tau_1, \tau_2, \dots, \tau_n)$ and the interpolant takes the final form:

$$\mathcal{I}_n[A](t, \theta) = \sum_j^n B_j(t)A(\tau_j, \theta) \quad (6.17)$$

where $B_j(t)$ is independent of θ parameter and it's computed offline, though the fast interpolation is an online step when θ is given. Notice that to give $A(t, \theta)$ for a given θ , the values at $\{A(\tau_j, \theta)\}_{j=1}^n$ has to be known. Here we show the computation of interpolant for amplitude A , similar computation for phase is also performed. Once we have reduced the problem in parameters and in time, the next step is to build a fit for parameter θ dependence at each empirical nodes. Recall that we intentionally discretize our parameter space such that we place our training set waveforms at Chebyshev-Gauss-lobatto nodes so that Chebyshev interpolation can be employed. Therefore, the amplitude and phase at each empirical node is given by:

$$A(\tau_j^A, \theta) \approx \bar{A}(\theta) := \sum_{l,m,n} a_{j,lmn} T_l(q) T_m(\Lambda_2^A) T_n(\Lambda_2^B), \quad (6.18)$$

$$\phi(\tau_j^\phi, \theta) \approx \bar{\phi}(\theta) := \sum_{l,m,n} a_{j,lmn} T_l(q) T_m(\Lambda_2^A) T_n(\Lambda_2^B). \quad (6.19)$$

We use Clenshaw summation techniques to do the summations. The computation of coefficients $a_{j,lmn}$ and $b_{j,lmn}$ of the Chebyshev series is an offline step and they are precomputed from the known amplitudes and phases on the training set grid using

Gaussian quadrature. The surrogate model is then given by evaluating the empirical interpolant at the parameteric fit to predict value at any new parameter θ :

$$A_S(t, \theta) := \sum_j^n B_j^A(t) \bar{A}(\theta), \quad (6.20)$$

$$\phi_S(t, \theta) := \sum_j^n B_j^\phi(t) \bar{\phi}(\theta). \quad (6.21)$$

Once a set of parameters are given $\theta := (q, \Lambda_A, \Lambda_B)$, the surrogate is evaluated online. From amplitude and phase we construct the strain h as given in Eq. 28 of Ref. [83].

6.3.1 Results

Here we extend the model given in Ref. [83] and construct the surrogate model for higher multipoles ($\ell = 2, 3, 4$ and $m = 2, 4$). We apply the above discussed method on tidal EOB model `TEOBResum` (discussed in Sec. 3.2) (Note: we work in dimensionless units rescaled by total mass M). The GW strain $h = h_+ - ih_\times$, is decomposed into spin weighted -2 spherical harmonics is given in Eq. (3.17). We can write separate multipoles as:

$$h_{\ell m} = A_{\ell m} \exp^{-i\phi_{\ell m}} \quad (6.22)$$

(ℓ, m) mode	n_ϕ	$\nabla\phi$	n_A	$\nabla A/A$
(2, 2)	9	0.0012	15	5.27×10^{-7}
(3, 2)	9	0.0011	11	0.00253
(4, 2)	8	0.0013	8	0.00348
(4, 4)	8	0.0031	11	9.19×10^{-5}

Table 6.4: We list the number of basis required for phase (column 2) and amplitude (column 4) for different modes (column 1). The error in phase $\nabla\phi$ (in column 3) maximized over the whole training set and maximum fractional error in amplitude $\nabla A/A =$ (column 5) over the whole training set and over all time samples.

We construct surrogate for each $\{A_{\ell m}\}$ and $\{\phi_{\ell m}\}$, starting at a frequency of 24 Hz and reconstruct the strain by applying Eq. (6.22) followed by Eq. (3.17). As seen from the Fig. (6.4) the typical phase difference between BNS and BBH is of the order ~ 12 radians, this is due to the tidal effects. Therefore, we would like to model the tidal interaction effectively such that the phase error is much smaller than 12 radians. We first assess the accuracy of each mode by comparing the phase and amplitude, computed at each grid point with the training set data. We list the maximum error in phase ($\Delta\phi = \max_{set} |\phi_S - \phi_{\text{EOB}}|$) and maximum fractional error in amplitude ($\Delta A/A = \max_{set} |A_S/A_{\text{EOB}} - 1|$) over the whole training set for different multipoles, maximized over all time samples, in Tab. (6.4). Note that the contribution from $m = 3$ modes is very small, therefore we do not model that and

also note that the error in amplitude for (3, 2) and (4, 2) modes looks high in the table is because this is fractional error and the amplitude for these modes are of the order of 10^{-3} or smaller. We compare in Fig. (6.5) the waveforms h_{lm} individually, for parameters $\theta = \{q = 0.5, \Lambda_2^A = 400, \Lambda_2^B = 80\}$, generated using the TEOBResum code and the surrogate model (h_{lm}^S) for the last 11 cycles before merger. These parameters are not from 4096 training waveforms which we use to sample the parameter space. We present the error in phase and amplitude in reconstructing all 4096 waveforms of training set in Fig. (6.6) for the dominant (2, 2) mode. One can notice that the error is higher for low mass ratio q and low Λ_2^A values cases.

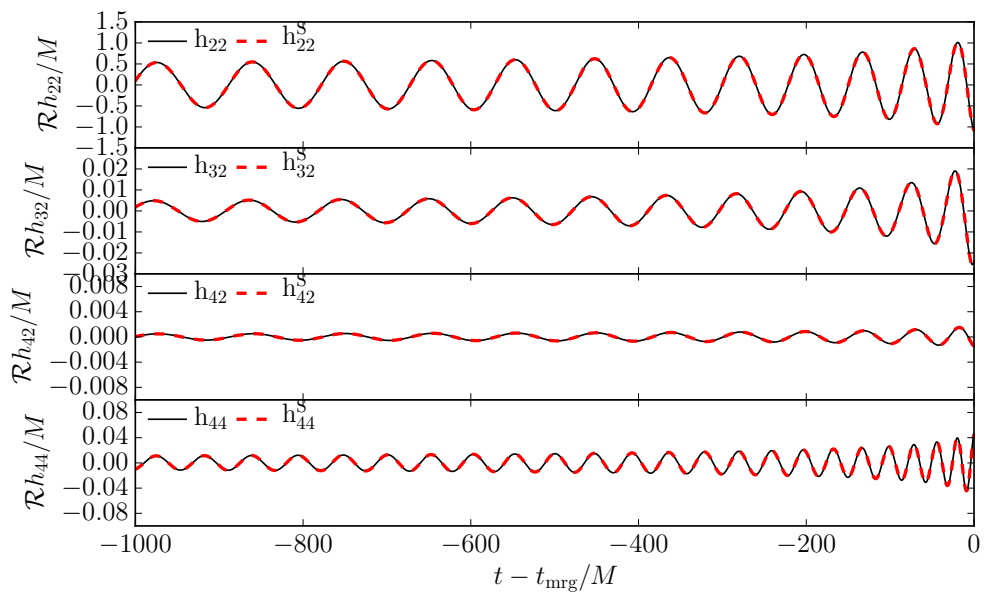


Figure 6.5: Fig. shows the waveform for a BNS system with parameters $q = 0.5$, $\Lambda_2^A = 400$, $\Lambda = 80$, for $(\ell = 2, 3, 4, m = 2, 4)$ mode generated using the TEOBResum code (black line) and the surrogate (h_{lm}^S) (dotted red line) generated for the same set of parameters for the final cycles before merger.

The maximum error in phase $\Delta\phi$ is 0.0012 radian and maximum fractional error in amplitude $\Delta A/A$ is 5.6×10^{-7} for the dominant (2, 2) mode. These error estimate are in agreement with the findings of Ref. [83]. In order to determine the accuracy of our multipolar surrogate model in computing a generic waveform, we compute the error in phase and amplitude at 1000 randomly chosen parameters (θ) in the given range. We present the result for the same in Fig. 6.7. The maximum error in phase is $\Delta\phi = 0.073$ radian and maximum fractional error in amplitude is $\Delta A/A = 0.0105$ in the multipolar waveform strain h (constructed using Eq. 3.17). The major advantage of employing surrogate modeling techniques is that it delivers a fast to evaluate model. We find that the time to generate a generic multipolar waveform starting

from 24 Hz is 12 sec while the original code which takes about 10 minutes on a single core of quad core intel core i7 machine. A parallelized version of this code could potentially speed up the evaluation further. At the moment, the code is written in MATLAB. (We have not implemented the code in LALSuite yet).

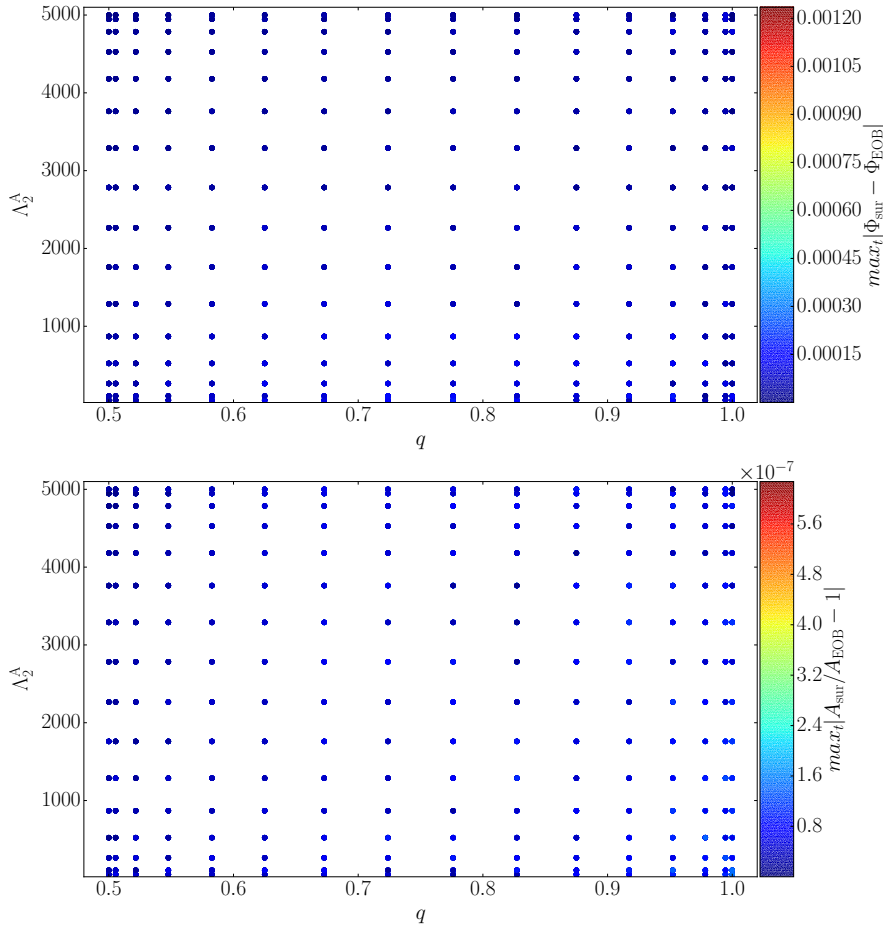


Figure 6.6: Fig. shows error in phase (top panel) and fractional error in amplitude (bottom panel) between 16^3 training set waveforms used to construct the reduced basis and waveforms generated using the surrogate model for (2, 2) mode.

TEOBResumS

TEOBResumS is an analytical waveform model with tides and spin and is described by five parameters, i.e., in addition to three parameters which describe TEOBResum, two more spin parameters, $\chi_{A,B}$ which are dimensionless spin of the stars. Parameters which defines this models are:

$$\theta = \{q, \tilde{\Lambda}_2^A, \tilde{\Lambda}_2^B, \chi_A, \chi_B\}. \quad (6.23)$$

Thus, it is a five-dimensional problem, and it computationally too expensive to solve with the direct reduced-order modeling techniques, as we discussed.

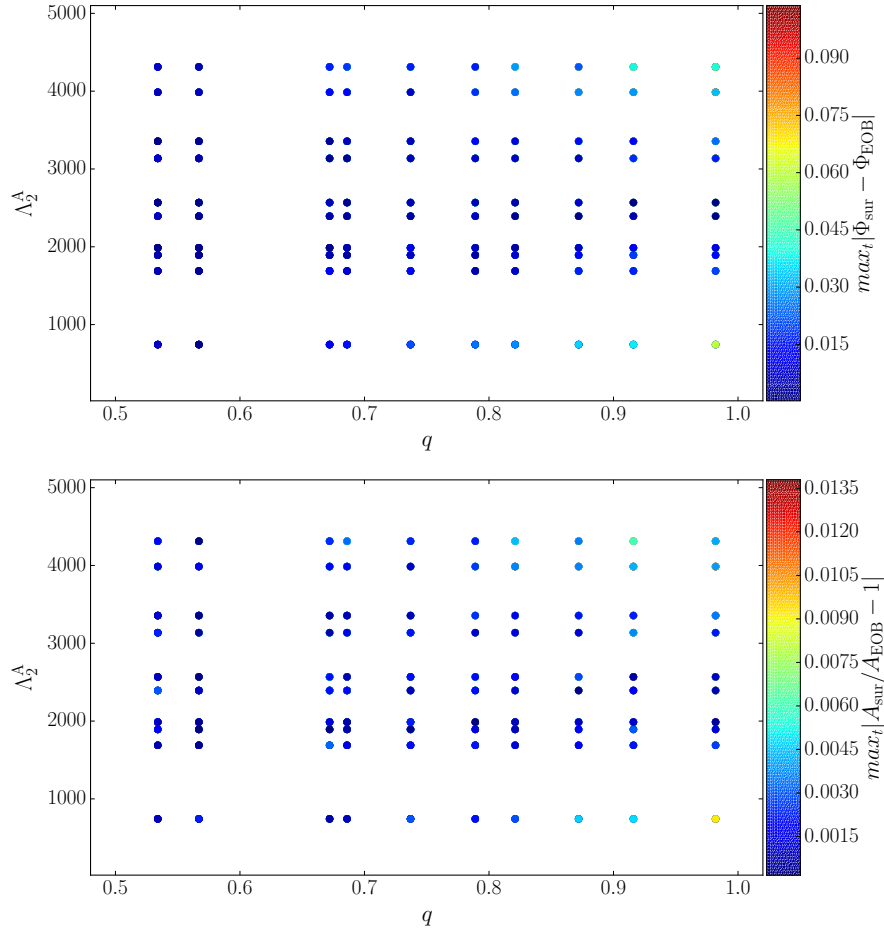


Figure 6.7: Fig. shows error in phase (top panel) and fractional error in amplitude (bottom panel) between 10^3 random generated multipolar waveforms and waveforms generated using the surrogate model.

To get required accuracy one requires, 16 nodes in each direction/parameter, thus 16^5 waveforms to construct a training set which is not feasible both in handling and preconditioning such large data set. Therefore, here, we suggest another method to make a surrogate model for TEObResumS. We can decompose the phase of GW into the contribution from point-baseline, spin, and tidal contribution as done for NRTidal models. Using the phase expression given, in Eq. (6.6) :

$$\phi(\theta) = \phi_{pm}(q, \hat{S}, \dots) + \phi_{tides}(q, \Lambda_A, \Lambda_B) + \phi_{ss}(\hat{a}_Q^2, \dots) \quad (6.24)$$

where $\phi_{pm}(q, \hat{S}, \dots)$ is the contribution to the phase due to the point-baseline with spin. $\phi_{tides}(q, \Lambda_A, \Lambda_B)$ phase comes from the difference of non-spinning tidal BNS waveform and non-spinning BBH waveform. $\phi_{ss}(\hat{a}_Q^2, \dots)$ phase corresponds to self spin interactions. Each part needs to carefully calculated for the same range of parameters. Once the training set for each part is generated, one can employ the same steps to generate the surrogate model for each part, as we have already discussed. Carefully adding the phases together would result in a compact and fast-to-evaluate model. This work is in progress [Dudi7].

Chapter 7

Numerical simulations

Numerical relativity simulations are inevitable to probe the last few orbits of BNS mergers and the post-mergers dynamics. Merger properties like ejecta, emission of GWs, mass transfer, the end state of the remnant, etc. can be studied through numerical simulations with full general relativistic hydrodynamics (GRHD). The NR framework comprises of solving the full set of Einstein's equations coupled to GRHD using numerical methods [138], [Collab3].

In this chapter, we study the numerical simulations of BNS coalescence. The SGRID code has been used to generate constraint solved and consistent initial data for the simulations. Our collaborations (Tichy et al. [Dudi5]) upgraded the SGRID code recently. We call the improved version *new SGRID* code throughout this thesis. In Sec. 7.2, we discuss a few tests to check the performance of the *new* version of the code as compared to the *old* code. We find that in the parameter space where both codes are valid, their performance is comparable. Nevertheless, the *new* code with modifications can reach more extreme regions of the BNS parameter space, e.g., it is capable of producing initial data for stars with very high spin close to break-up, high compactness and high mass-ratio binary systems [Dudi5]. In section 7.3, we discuss the evolution of the initial data in the context of highly spinning BNS [Dudi6].

7.1 Numerical relativity

We discuss some of the basics of NR, however, for a detailed description of underlying principles of NR, we refer the reader to Refs. [139–142]. Throughout this work, we have used SGRID code (both versions) to produce the initial data and the BAM code for the dynamic evolution of the initial data, but no changes in the codes have been made as a part of the thesis.

The Einstein equations are given in Eq. (2.1) in a fully covariant way. In order to solve Eq. (2.1) for very generic scenarios, e.g., BNS mergers, one has to write those equations in a form suitable for obtaining numerical solutions. One of the approaches to obtain that is 3+1 decomposition, which allows us to slice the four-

dimensional spacetime into three-dimensional spacelike surfaces (hypersurfaces) along a timelike curve. For a given n -dimension Manifold \mathcal{M} , we can foliate \mathcal{M} by $(n-1)$ dimensional hypersurfaces Σ , if there exist a scalar field t on \mathcal{M} , whose gradient never vanishes such that all level surfaces are hypersurfaces. The parameter t can be understood as coordinate time on the hypersurface $\Sigma_t = \Sigma(t)$. The timelike, future directed unit vector n which is normal to the slice Σ_t is given by:

$$n_\mu = -\alpha \nabla_\mu t \quad (7.1)$$

where α is called lapse function. The normalization condition of timelike vector leads to $n^\mu = -1/g^{tt}$. The induced 3 metric on Σ_t is given by:

$$\gamma_{\mu\nu} = g_{\mu\nu} + n_\mu n_\nu \quad (7.2)$$

Another quantity of interest is the shift vector β^μ , defined as the difference between the normal vector n^μ and ∂_t at each point (x^μ) on the hypersurface. The extrinsic curvature $K_{\mu\nu}$ characterizes the bending of Σ in \mathcal{M} :

$$K_{\mu\nu} = -P_\mu^\sigma \nabla_\sigma n_\nu \quad (7.3)$$

where $P_\mu^\nu = \delta_\mu^\nu + n_\mu n^\nu$ is the spatial projection operator. For the evolution of lapse and shift, we employ the 1+log slicing condition along with the gamma driver shift condition, see Ref. [143] for details. The slicing conditions are indispensable for a stable numerical setup, and with an evolution system, they provide a well-posed partial differential equation (PDE) problem. The Einstein Eq. (2.1) are projected onto Σ_t and perpendicular to Σ_t , which splits the equations into 3+1 form and gives a system of evolution and constraint equations. The Hamiltonian and momentum constraint equations are

$$R + K^2 - K_{\alpha\beta} K^{\alpha\beta} = 16\pi E, \quad (7.4)$$

$$D_j K^{ij} - D^i K = 8\pi S^i, \quad (7.5)$$

where $S = S^\mu S_\mu$ is the spatial part of $T_{\mu\nu}$, E denotes the energy density measured by the Eulerian observer with the four velocity n^ν . R is the three dimensional Riemann tensor and D_μ is the three dimensional covariant derivative after projection of standard covariant derivative onto the space orthogonal to n^α . The constraint equations are required to be solved at all time slices and, thus, also for constructing initial data. The evolution equation of the induced metric is given by:

$$\partial_t \gamma_{ij} = -2\alpha K_{ij} + D_i \beta_j + D_j \beta_i, \quad (7.6)$$

and the evolution equation of the extrinsic curvature:

$$\begin{aligned} \partial_t K_{ij} = & -D_i D_j \alpha + \beta^k \delta_k K_{ij} + K_{ik} \partial_j \beta^k + K_{kj} \partial_i \beta^k \\ & + \alpha({}^3R_{ij} + K K_{ij} - 2K_{ik} K_j^k) + 4\pi\alpha(\gamma_{ij}(S - E) - 2S_{ij}). \end{aligned} \quad (7.7)$$

The equations (7.4, 7.5, 7.6, 7.7) are called ADM equations, named after Arnowitt, Deser and Misner [144]. Since the ADM equations are only weakly hyperbolic, they are not suitable for long stable numerical simulation. The formulation we used in this thesis is derived by YORK [145] as it is more stable and thus suitable for long numerical simulations. BSSN or BSSNOK [146–148] is the improved reformulation of the ADM equation which provides the necessary well-posedness of the evolution equation. In BAM code, we have BSSN implemented as well as Z4c [149, 150] which is a more recent evolution system. Advantages of Z4c scheme are constraint damping property and no zero speed characteristics. The code employs also constraint preserving boundary condition. In this thesis, we have used the Z4c evolution scheme. We refer the reader to [142] for thorough details about the evolution schemes and the equations.

EOS	$\rho_{crust}/10^{-4}$	Γ_1	Γ_2	Γ_3	M_{max}	M_{max}^b	C_{max}	c_S^{max}
SLy	2.36953	3.005	2.988	2.851	2.06	2.46	0.31	1.0
ALF2	3.15606	4.070	2.411	1.890	1.99	2.32	0.26	0.65
H4	1.43830	2.909	2.246	2.144	2.03	2.33	0.26	0.72
$\Gamma 2\kappa 124$	$\Gamma = 2$		$\kappa = 123.6489$		1.82	2.00	0.21	0.62

Table 7.1: Table shows the properties of the EOS employed in this work. The column refers to name of the EOS, the maximum density in the crust, the three polytropic exponents for the individual pieces, and the maximum supported gravitational mass M_{max} , baryonic mass M_{max}^b , compactness of the isolated nonrotating star C_{max} , and maximum adiabatic speed of sound within the maximum stable neutron star configuration respectively. This table is adopted from Ref. [142].

The evolution formulation like BSSN and Z4c requires initial data for the dynamical evolution. We use SGRID code (Section 7.2) to generate constraint solved initial data which employs conformal thin sandwich equations [151–153] along with the constant rotational velocity (CRV) approach [154, 155] to solve the constraint equations. For the evolution equation of the matter variables, we use a 3+1 Eulerian formulation of GRHD [156, 157] along with “Valencia formulation” [158]. We do not directly evolve the primitive variables but convert them first into conservative variables and then evolve them. We close the evolution system finally by choosing an EOS of the form $p = P(\rho, \epsilon)$ for the stars. In this thesis, we employ polytropic EOS $P = \kappa\rho^\Gamma$ and piecewise polytropic EOS $P = \kappa_i\rho^{\Gamma_i}$. Several zero-temperature EOS like ALF2, SLy, H4, MS1b etc. can be fit with piecewise polytropes [159]. The EOSs we have used in this Chapter, are given in the Tab. (7.1). We define the compactness

by $C_i := M_i/R_i$, where R_i is the radius of i^{th} star (in Schwarzschild coordinates) and M_i is its gravitational mass. BAM employs the method of lines approach to solve the evolution equation along with matter equation. The spatial dimensions are discretized using finite differencing method which provide ODE's at each grid point. For the time integration fourth order Runge Kutta method is employed and Courant-Friedrichs-Lewy condition of 0.25 is used. For the computation of numerical flux with an approximate Riemann solver, the code employs the Local Lax-Friedrich flux. We employ adaptive mesh refinement techniques in BAM for properly resolving near field region and a far-field region.

7.2 Initial data

Initial data are a prerequisite for any evolution code like BAM. There are many BNS initial data generating codes developed by the numerical community over the past years, e.g., LORENE [160], BAM's multigrid solver [161], COCAL code [162], and SpEC's spectral solver SPELLS [102, 163], and spectral code SGRID [99, 164, 165]. These codes have been employed to construct the initial data for various regions of the parameter space. However, there are still scenarios that have not been studied, e.g., highly spinning systems close to break-up or BNS systems with high compactness or very high mass-ratio¹. These scenarios will be of importance as, with the advance of GW detectors, events with such extreme properties are likely to be observed. The *new* SGRID code is capable of generating initial data for such scenarios. This code is a pseudospectral code, i.e., it uses spectral methods to compute spatial derivatives, described in Refs. [99, 154]. It solves the coupled elliptic constraint equations along with matter equations to compute quasi-equilibrium initial data for the BNS system. The code employs several domains to cover the stars and space around the stars, such that domain boundaries coincide with the star surface and each domain described by their coordinates. This is crucial as at the surface, where the specific enthalpy (h) becomes $h = 1$, the pressure P , internal energy density ϵ , and mass density ρ_0 becomes non-differentiable though the matter inside is smooth. In the *old* SGRID, this problem was handled using Ansorg's coordinate (A, B, ϕ) , described in Ref. [99] and depicted in Fig. 1 of Ref. [99]. Only 6 computational domains were needed to cover all of the space. The coordinate transformation contains freely specifiable functions $\sigma \pm (B, \phi)$ that can be chosen such that the domain boundaries adapt the star surface. Unfortunately, the coordinate transformation from Ansorg's coordinate (A, B, ϕ) to Cartesian coordinates (x, y, z) is not straightforward, which makes it difficult to adjust $\sigma \pm (B, \phi)$ functions such that the domain boundaries coincide with the star's surfaces. Moreover, coordinate singularity arises while solving the elliptic equations which give rise to numerical

¹Here by mass-ratio, we mean $Q = M_A/M_B > 1$

inaccuracies.

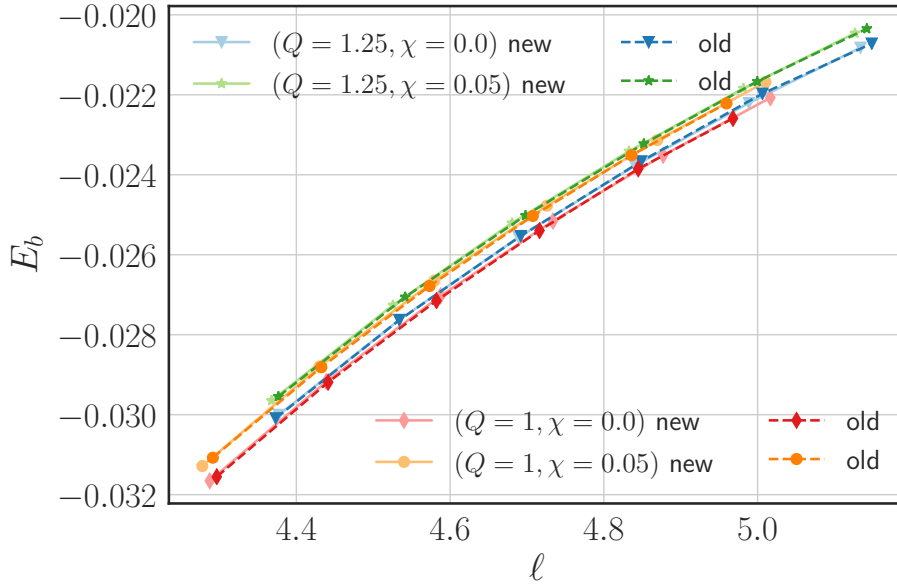


Figure 7.1: Binding energy as function of the reduced orbital angular momentum for binary systems with $M_A = M_B = 1.375$ and $M_A = 1.445, M_B = 1.156$, $\chi_{A,B} = 0.0$ and $\chi_{A,B} = 0.05$ and SLy EOS.

Therefore, to mitigate these issues Tichy et al. [Dudi5] have upgraded the *old* SGRID code to the *new* SGRID code. In the *new* SGRID, we use surface fitted cubed sphere coordinates (λ, A, B) which have no singularities. Here, we use several domains to cover the star and its surrounding, e.g., the star is covered by cube in the center, which is surrounded by cubed sphere wedges as shown in Fig. C.1a in Appendix C. The surroundings are covered by multiple domains, which together cover a large cube. Additionally, the conformal factor ψ has been linearized, and a rescaled density ρ has been employed in order to guarantee the uniqueness of the solution. Moreover, the velocity potential ϕ equation has been modified on the star surface such that the kinks which developed in the first derivative of ϕ now vanishes. At the star center the velocity potential ϕ equation remains unchanged and by imposing the boundary condition on the star surface, the changes in ϕ are small. We list the main equations needs to be solved to generate the initial data in Appendix C, however details about the modifications in the *new* SGRID code are beyond the scope of this thesis and thus we refer to the Ref. [Dudi5].

Numerical results

As the first check of the *new* SGRID code, we perform following tests and compare the results with the *old* SGRID code.

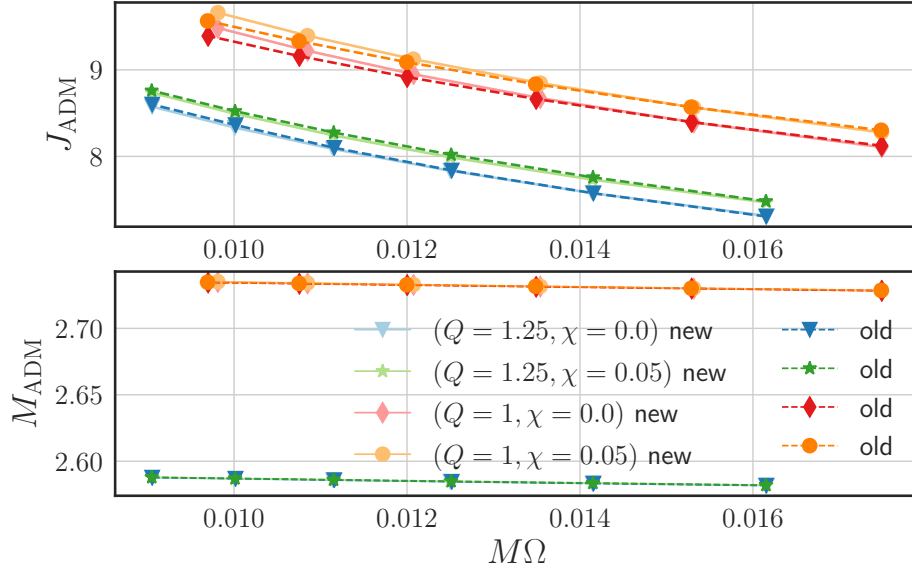


Figure 7.2: J_{ADM} spacetime's ADM angular momentum and M_{ADM} ADM mass as a function of the angular orbital velocity ($M\Omega$). The employed binary systems have masses $M_A = M_B = 1.375$ and $M_A = 1.445, M_B = 1.156$, and spins $\chi_{A,B} = 0.0$ and $\chi_{A,B} = 0.05$, and SLy EOS. The label new denotes initial data constructed using *new* SGRID code and label old denotes same configuration constructed using *old* SGRID code.

We compute initial data sequences for four different configuration of binary parameters with the *old* and the *new* version of the code. The four set of configurations have a piecewise-polytropic fit of SLy EOS with gravitational masses $M_A = M_B = 1.375M_\odot$, i.e., mass ratio $Q = 1$ and $M_A = 1.445M_\odot, M_B = 1.156M_\odot$, i.e., mass ratio $Q = 1.25$ and dimensionless spins $\chi_{A,B} = 0$ and $\chi_{A,B} = 0.05$. The initial data are computed at six different initial separation $b = (18, 20, 22, 24, 26, 28)^2$.

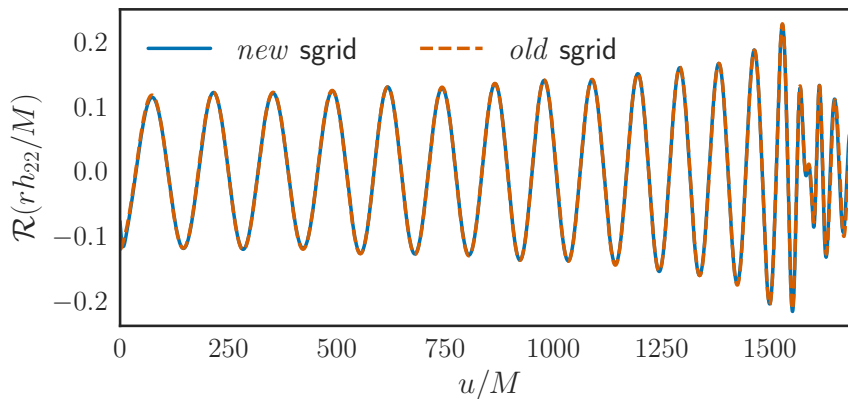


Figure 7.3: Comparing the waveforms computed for the configuration discussed in text, where the initial data is computed using *old* (orange curve) and *new* (blue curve) SGRID code. BAM code is used to evolve the initial data.

² b is the initial separation between the two stars in SGRID's coordinate system, see e.g. Eq. 2.34b of Ref. [99]

In Fig. 7.1, we compare binding energy E_b versus the reduced orbital angular momentum ℓ for all the configurations mentioned. The binding energy E_b is given by:

$$E_b = \frac{1}{\nu} \left(\frac{M_{ADM}}{M} - 1 \right), \quad (7.8)$$

and the reduced orbital angular momentum:

$$\ell = \frac{L}{\nu M^2} = \frac{J_{ADM} - S_A - S_B}{\nu M^2}. \quad (7.9)$$

where $\nu = M_A M_B / M^2$ is the symmetric mass ratio and M is the total mass. $S_{A,B}$ are individual spin magnitudes. In Fig. 7.1, the solid lines represents the *new* SGRID data while the dashed curve represents the *old* SGRID data. Fig. 7.2 shows the ADM angular momentum (J_{ADM}) *top panel* and ADM mass (M_{ADM}) *bottom panel* as a function of the angular orbital velocity ($M\Omega$) for both versions of SGRID. We found that the results from the two versions of SGRID are in good agreement with each other, and the differences are within numerical accuracy. As a second test, we compute initial data, again using both *old* and *new* SGRID code, for a polytropic EOS i.e, $\kappa = 123.6489$ and $n = 1$, and equal mass binary with baryonic mass $M_A^b = M_B^b = 1.625$ and two stars placed at a distance of 68.8 km. We evolve the two initial data with BAM code with 6 levels³ of refinement and use 96 points to cover the stars. The GWs are extracted at a distance of $900M_\odot$. Hamiltonian and momentum constraints for the evolution are computed in level $l = 1$ i.e, at the second outermost Cartesian box of the numerical domain. We show GWs in Fig. 7.3 and the Hamiltonian and Momentum constraints in Fig. 7.4 for both versions of SGRID.

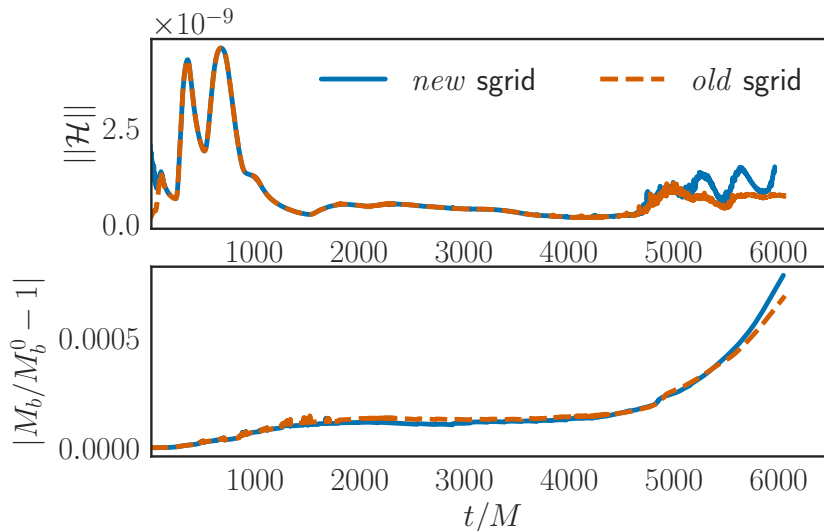


Figure 7.4: Absolute value of Hamiltonian constraint (top panel) and the baryonic mass conservation (bottom panel) is shown for the same setup shown in Fig. 7.3 for both versions of SGRID.

³levels are described in Sec. 7.3

Empirical $\omega - \chi$ relation

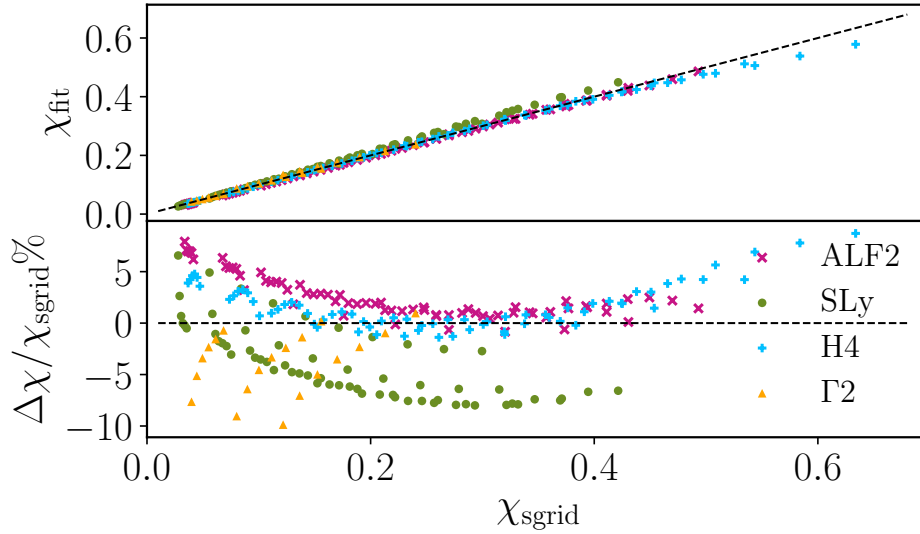


Figure 7.5: The dimensionless spin computed according to Eq. 7.10 as a function of spin computed in *new* SGRID for different EOSs (top panel). The fraction residuals are shown in the bottom panel. The black dash curve represents $\chi_{\text{sgrid}} = \chi_{\text{fit}}$ scenario.

One can construct initial data with arbitrary spin [99, 164, 165] using SGRID code. However, the spinning motion is defined by the rotational part of the velocity in terms of the angular velocity of the fluid ω^z in CRV approach. And, one can only specify the ω^z , masses and EOS as the input in SGRID code and not the “spin” of a star directly⁴. Though, *new* SGRID outputs a spin estimate χ_{SGRID} at the end. Therefore we need to find an ansatz for spin in terms of SGRID’s input parameter, in order to reduce the computational cost of finding particular configurations of initial data. One such phenomenological fit is given in Appendix C.2 of Ref. [99]. However, we found that it might give large errors at high spin. Therefore, building upon that, we fit the following data generated for single stars to output χ_{fit} . We use 4 EOS, namely SLy, ALF2, H4 and $\Gamma 2$ (given in the Tab. 7.1) with baryonic masses $M_b/M_\odot \in [1.1, 1.7]$ in steps of 0.1 and compactnesses in the range of $\mathcal{C} \in [0.09, 0.20]$. We find the following phenomenological fit for the dimensionless spin magnitude χ of a single NS via numerical experiments:

$$\chi_{\text{fit}} = a_1(1 + m_1 M_b)(1 + c_1 \mathcal{C} + c_2 \mathcal{C}^2 + c_3 \mathcal{C}^3 + c_4 \mathcal{C}^4)(1 + d_1 \omega^z) \omega^z, \quad (7.10)$$

where the coefficients $a_1 = 59.329$, $m_1 = 1.9267$, $c_1 = -17.1537$, $c_2 = 122.8986$, $c_3 = -401.3542$, $c_4 = 483.0869$, and $d_1 = 10.2497$ are computed by fitting the data,

⁴Methods to estimate the spin magnitude of a single star in a binary has been proposed in Sec. II.C of Ref. [166]

shown in Fig. 7.5. Specifically, we employ for all combinations of the NS mass and EOS, ten different values of $\omega^z \in [0.000, 0.02]$ in steps of $\Delta\omega^z = 0.002$, for all $M_b \in [1.1, 1.2, 1.3, 1.4, 1.5, 1.6, 1.7]$. The fractional residuals for each configuration is shown in the bottom panel of the Fig. 7.5. We found the new fit gives maximum 10% error for some extreme cases otherwise the error in the estimate is below 7% .

7.3 Spinning BNS mergers

There has been a number of observations of fast spinning NSs such as PSRJ1748 – 2446ad [167], which is the fastest spinning NS with a spin period of 1.4 ms, i.e. frequency of 716 Hz⁵, PSRJ1807 – 2500B [168], which is the fastest spinning NS in a binary with a frequency of 239 Hz, and PSRJ1946 + 2052 [169], which is the fastest spinning NS in a BNS system with frequency 59 Hz. Moreover, it has been shown in recent studies [25, 124, 170] that even if small spins are neglected, this leads to biases in the measurement of the source properties. These two facts stress that it is crucial to model the spin effects accurately. In this regard, we report our numerical simulations of spinning BNS upto $\chi = 0.29$. These are intermediate results, and other numerical simulations with high resolution and different spin configurations are undergoing.

Initial configurations: We employ the *new* SGRID code to construct initial data with the fixed initial separation of 73.5 km between two stars for all setups. We employ Eq. (7.10) to obtain an estimate of the four-velocity corresponding to a given dimensionless spin χ as given in fifth and sixth column of Tab. 7.2.

Evolutions: We use the BAM code to evolve the initial data [171–173]. We use the 3+1 decomposition of the Einstein equations using the Z4c scheme [149, 150]. For the evolutions of lapse and shift, 1+log and gamma-driver conditions are employed [159, 174, 175]. Further details are described in Sec. 7.1. We employ a hierarchy of cell-centered nested Cartesian grids to discretize the numerical domain. We have L levels of refinement, labeled as $l = 0, \dots, L - 1$, in the hierarchy. There is constant grid spacing h_l in each level of refinement with n (or n^{mv}) points in each direction. Each inner level is twice refined than the outer one, i.e., $h_l = h_0/2^l$. The grids are nested such that any grid at level l , ($l > 0$, as $l = 0$ is the outermost level) is covered by the grids at level $l - 1$. We also have some dynamically moving levels $l > l^{mv}$ by employing the technique of "moving boxes". For this work we set $l^{mv} = 2$ and use on total seven refinement levels for all the configurations listed in Tab. 7.2. The grid spacing in the coarsest level is $h_0 = 10.8M_\odot$ and the grid spacing in the finest level is $h_6 = 0.168M_\odot$ are for all the setups with EOS ALF2; $h_0 = 12M_\odot$ and $h_6 = 0.188M_\odot$ are for all setups with EOS H4; and $h_0 = 10M_\odot$ and $h_6 = 0.156M_\odot$ are

⁵This corresponds to a dimensionless spin $\chi \in [0.3, 0.6]$ and the large range is due to uncertainty in the measurement of EOS and mass.

for all setups with EOS SLy. We employ $n = 192$ points in the non-moving boxes and $n^{mv} = 96$ points in the moving boxes. We perform eccentricity reduction procedure for all the configurations to reduce residual oscillations. The procedure has been described in Refs. [99, 176] and shown that eccentricity reduced initial data delivers better quality numerical waveforms. The number of iterations performed to reduce the eccentricity below $< 10^{-3}$ is listed in the last column of Tab. 7.2. We consider BNS configurations for equal mass system, i.e., $Q = 1$, ($M_A = M_B$), and vary EOS and spins. Recall that the dimensionless spin is given by ($\chi_{A,B} = S_z/M_{A,B}^2$)⁶. We use three EOSs, namely, SLy, ALF2, and H4. Recall that SLy and ALF2 are soft EOSs, and both are within the constraint imposed by GW170817. However, H4 is a stiff EOS and is on the edge of posteriors obtained for GW170817 [Fig. 2.2] and ruled out by source property article Ref. [Collab2]. Though, we believe that using H4 EOS will help in modeling the spin effects better. All the BNS configurations employed are listed in Tab. 7.2. For each EOS, we have a (00) case meaning none of the stars are spinning. We have two spinning cases with SLy EOS, (i) SLy₁₀^(↑↑)⁷ has both stars with $\chi_A = 0.1545$ spin aligned with the orbital angular momentum. (ii) SLy₁₅^(↑↑) has both stars with aligned spin $\chi_{A,B} = 0.2379$. For ALF2 EOS, (i) ALF2₁₀^(↑↑) is an aligned spin setup with $\chi_{A,B} = 0.187$, and (ii) ALF2₁₅^(↑↑) is one of the highest spinning numerical simulations to date, has both stars spinning with aligned spin $\chi_{A,B} = 0.2903$. For H4 EOS, H4₁₀^(↑↑) setup has aligned spins of both stars with $\chi_{A,B} = 0.2086$ ⁸.

7.3.1 Analysis

Our analysis tools were discussed in Refs. [177, 178] to which we refer the reader for details. This includes the computation of the ejecta properties, merger remnant characterizations, and the extraction of GWs.

Our simulations span $N_{\text{orb}} \sim 14 - 17$ orbits until the merger as the initial distance between the stars is 73.5 km. One finds that the number of orbits increases for cases with spin aligned to the orbital angular momentum due to the “orbital hang-up” effect [99, 100, 166, 179]. We find that this effect is comparable to the variation in EOS, i.e., simulations with stiffer EOS take fewer orbits to merge starting at a fixed initial distance between the stars, e.g., SLy⁽⁰⁰⁾ takes approximately 16 orbits to merge while H4⁽⁰⁰⁾ takes approximately 14 orbits.

⁶for aligned spin

⁷Naming convention follows: name of the EOS with superscript shows arrows aligned or anti aligned to the angular momentum and subscript shows the ω^z quantity as given in seventh column of Tab. 7.2.

⁸H4₁₅^(↑↑) setup is in progress and has a very high spin $\chi_{A,B} = 0.34$ and thus, it is challenging to simulate

Name	EOS	$M_{A,B}[M_{\odot}]$	$S_{A,B}$	χ_A	χ_B	ω^z	$\tilde{\Lambda}$	κ_{eff}^T	iteration
SLy ⁽⁰⁰⁾	SLy	1.3500	0	0.0	0.0	0.0	392.08	73.51	2
ALF2 ⁽⁰⁰⁾	ALF2	1.3557	0	0.0	0.0	0.0	715.92	134.23	2
H4 ⁽⁰⁰⁾	H4	1.3717	0	0.0	0.0	0	1013.7	198.06	1
SLy ₁₀ ^(††)	SLy	1.3500	0.284, 0.283	0.1545	0.1545	0.010	392.08	73.51	2
ALF2 ₁₀ ^(††)	ALF2	1.3557	0.346	0.1869	0.1869	0.010	715.92	134.23	1
H4 ₁₀ ^(††)	H4	1.3717	0.395	0.2087	0.2087	0.010	1013.7	198.06	1
SLy ₁₅ ^(††)	SLy	1.3500	0.437	0.2379	0.2379	0.015	392.08	73.51	2
ALF2 ₁₅ ^(††)	ALF2	1.3557	0.537	0.2903	0.2903	0.015	715.92	134.23	2

Table 7.2: BNS configurations for equal mass systems ($M_A = M_B$) with baryonic mass ($M^b = 1.494607$). The first column refers to the name of the configuration. EOS in the second column, the gravitational mass of star A (M_A) in the third column, the stars' spin ($S_{A,B}$) in the fourth column, the dimensionless spins ($\chi_{A,B}$) in the fifth column, rotational part of the fluid velocity in terms of the angular velocity (ω^z) in the sixth column, tidal deformability ($\tilde{\Lambda}$) in the seventh and tidal coupling constant (κ_{eff}^T) in the eighth column and number of iterations performed for reducing eccentricity in the ninth column are given.

At the later stage of the evolution, a fraction of matter ejected during merger. The ejecta is shown for irrotational cases in left panel and for spinning cases in right panel in Fig. 7.16 at the merger. After the merger, the remnants are HMNS⁹ [Sec. 2.2] for all the BNS simulations, listed in Tab. 7.2, which are supported for a longer time by differential rotation for spinning configurations.

Energetics

We investigate the BNS dynamics via the gauge-invariant binding energy (E_b) and specific angular momentum (ℓ), $E_b(\ell)$ -curves [180]. The specific binding energy as given in Eq. (7.8), can be generalized for the dynamical evolution as

$$E_b = \frac{1}{\nu} \left[\frac{M_{\text{ADM}}(t=0) - \mathcal{E}_{\text{rad}}}{M} - 1 \right], \quad (7.11)$$

where \mathcal{E}_{rad} denotes the energy emitted by GWs and M is the total gravitational mass of the system. The specific orbital angular momentum (in dimensionless units) for the dynamical evolution is

$$\ell = \frac{L(t=0) - \mathcal{J}_{\text{rad}}}{\nu M^2} = \frac{J_{\text{ADM}}(t=0) - S^A - S^B - \mathcal{J}_{\text{rad}}}{\nu M^2}, \quad (7.12)$$

where \mathcal{J}_{rad} is the angular momentum emitted via GWs. J_{ADM} and $S^{A,B}$ are the inputs from the initial data.

⁹hypermassive neutron stars (HMNS)

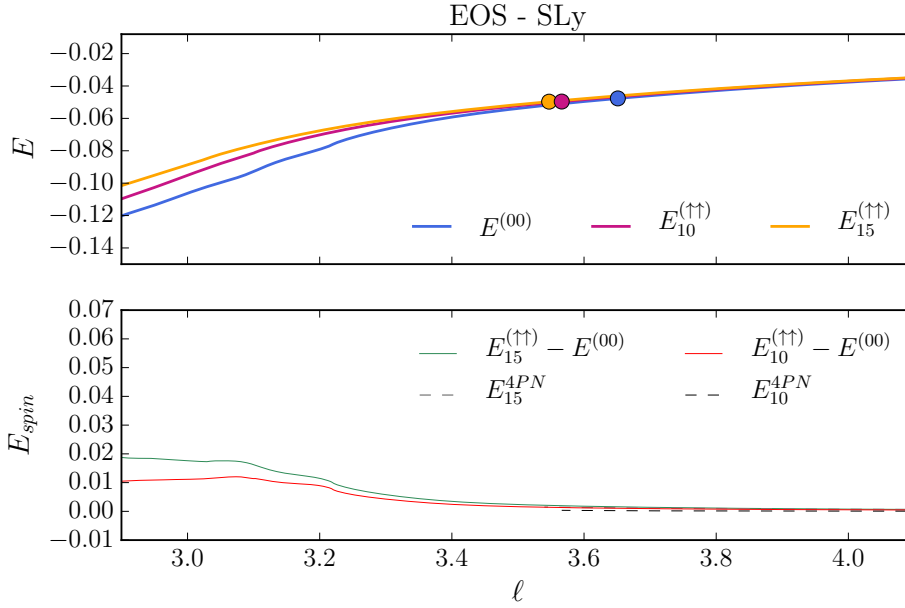


Figure 7.6: Top panel: Binding energy as a function of specific angular momentum for the configuration with SLy EOS. The markers refer to the moment of merger for all configurations. The bottom panel shows the spin contribution to the binding energy for the setups with spin using SLy EOS as well as the 4 PN estimates as dashed lines.

This equation follows the assumption that the spin magnitude remains approximately constant during the evolution [102].

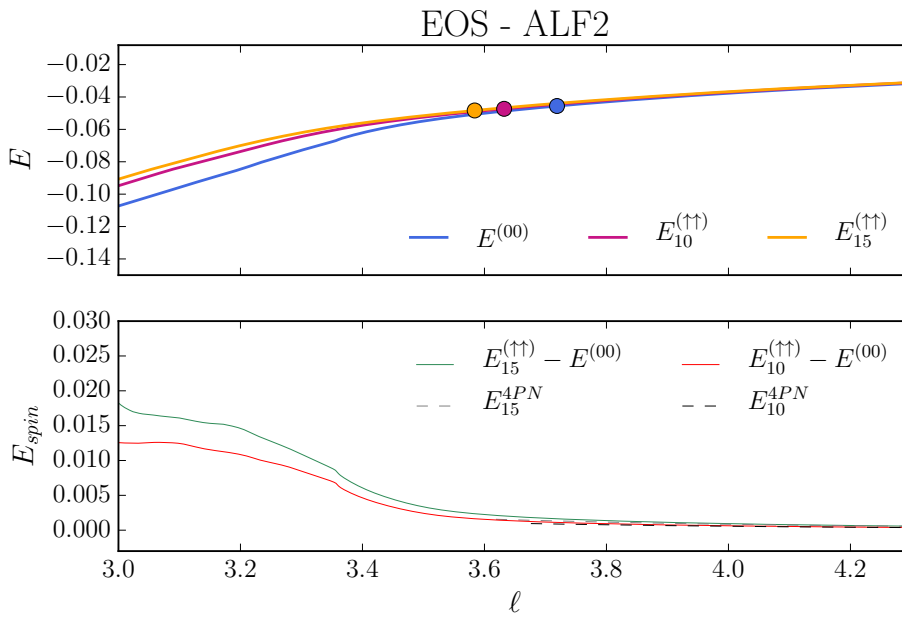


Figure 7.7: Top panel: Binding energy as a function of specific angular momentum for the configuration with ALF2 EOS. The markers refer to the moment of merger for all configurations. The bottom panel shows the spin contribution to the binding energy for the setups with spins as well as the 4 PN estimates as dashed lines.

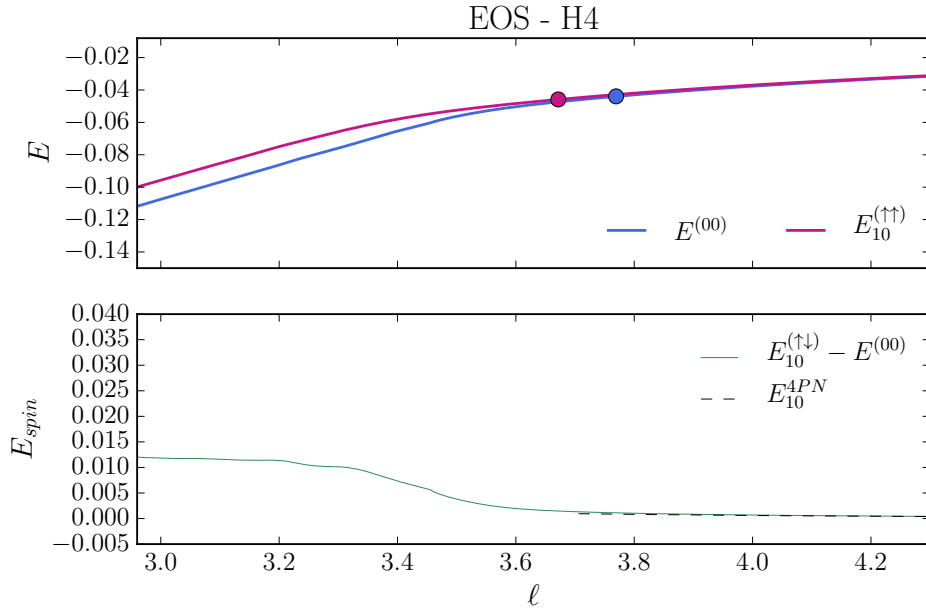


Figure 7.8: Top panel: Binding energy as a function of specific angular momentum for the configuration with H4 EOS. The markers refer to the moment of merger for all configurations. The bottom panel shows the spin contribution to the binding energy for the setups with spins as well as the 4 PN estimates as dashed lines.

We investigate the effects of spin on $E_b(\ell)$ curves and therefore on the dynamics for different EOS. We analyze $E_{spin} = E_{\omega^z}^{(\uparrow\uparrow)} - E^{(00)}$, [hereafter we drop the subscript "b"], where $E^{(00)}$ is the binding energy of the non-spinning configuration and $E_{\omega^z}^{(\uparrow\uparrow)}$ is the binding energy of the spinning configuration. Our results are presented in Figs. (7.6, 7.7 and 7.8), which show the specific binding energy for all the setups listed in Tab. 7.2. For example, configurations with SLy EOS are shown in Fig. 7.6 (top panel) and the respective contributions due to the spin E_{spin} is shown in the bottom panel¹⁰ Fig. 7.7 shows the $E_b(\ell)$ -curves (*top panel*) and E_{spin} (*bottom panel*) for the setups with ALF2 EOS. The binding energy E for aligned spin systems are larger than for non-spinning system, i.e. $E_{spin} > 0$, which shows the repulsive nature of spins aligned to the orbital angular momentum. Also, $E_{15}^{\uparrow\uparrow} > E_{10}^{\uparrow\uparrow}$ which further illustrate that the higher spinning systems are more unbound. At the merger, the ℓ decreases as spins increase in the configurations, which illustrates the impact of the “hang up” effect. As the systems with high spins have more orbits to emit the angular momentum, therefore they have low specific angular momentum at the merger. Similar behavior of the $E_b(\ell)$ curves can be noticed for the configurations with H4 EOS in Fig. 7.8. We plot 4 PN estimates as dashed curves to compare with our numerical results upto the merger. We notice significant deviations at $\ell \leq 3.8$ which show that PN estimates are inaccurate for the last few orbits. The 3.5 PN and 4 PN expressions for binding energy can be found in Ref. [178] (and references

¹⁰Note: The plot reads from right to left, i.e., from high specific angular momentum ℓ to lower, as the angular momentum gets emitted via GWs, the orbit shrinks.

therein), and Refs. [181, 182], respectively. $E_b(\ell)$ curves can be used to study the individual effects like spin-orbit, spin-spin, self-spin and tidal effects for which we require to have more setups with ($\downarrow\downarrow$) anti-aligned spins as well as setups with only one spinning star ($\uparrow 0$) and ($\downarrow 0$) [178]. These configurations are under progress.

Ejecta

We characterize matter as unbound if it follows

$$u_t < -1 \text{ and } \bar{v}_r = v^i x_i > 0, \quad (7.13)$$

where the time component of the fluid 4-velocity $u_t = -W(\alpha - \beta_i v^i)$ with a lower index, α denotes the lapse, β^i denotes the shift vector, W represents the Lorentz factor and $x^i = (x, y, z)$. Eq. (7.13) is based on the assumption that the fluid elements follow geodesics and the orbit is unbound and has an outward pointing velocity, cf. [183]. We compute the ejecta mass as the following integral, which is performed on the region where the material is unbound as given by Eq. (7.13),

$$M_{ej} = \int_{\mathcal{U}} d^3x q^{(D)} \quad (7.14)$$

where $q^{(D)} = \sqrt{\gamma} D$, D denotes fluid's rest frame baryonic mass, γ denotes the determinant of the 3-metric. The region of integration is given by

$$\mathcal{U} = \{x^i = (x, y, z) : u_t < -1 \text{ and } \bar{v}_r > 0\}. \quad (7.15)$$

The ejected masses for all the configurations are listed in the sixth column of Tab. 7.3. We notice that the ejection of mass decreases with increasing spins aligned to the orbital angular momentum for the systems we considered here [Tab. 7.2]. This is consistent with the recent findings [184]; however, we do not add neutrino-cooling effects or magnetic fields. A possible explanation could be that the high spin configurations have more angular momenta at the merger; therefore, the merger would be less impactful, and possibly this leads to less ejecta. We show the rest-mass density and unbound rest-mass density (ejecta) in the $x - y$ plane in Fig. 7.16 around merger time. The left panel shows the irrotational cases for different EOS SLy, ALF2, and H4, from top to bottom, respectively, and the right panel shows corresponding spinning configurations. The figure shows the mass ejection that originates from the tidal tail. We do not find any significant mass ejection due to core collision; such ejecta is mostly shock driven and happens in a perpendicular direction to the orbital plane. One possible reason for the less shock driven ejecta is that the system mergers with considerable angular momentum.

Name	M_{ADM}	J_{ADM}	N_{orb}	$M\omega_{22}$	$M_{ej} [M_{\odot}]$	$M\omega_{\text{mrg}}$	$f_{\text{mrg}} [\text{Hz}]$	$f_2 [\text{Hz}]$
SLy ⁽⁰⁰⁾	2.68	8.02	≈ 16	0.0320	8.8×10^{-3}	0.157	1886	3384
ALF2 ⁽⁰⁰⁾	2.69	8.08	≈ 15	0.0322	2.4×10^{-3}	0.142	1692	2760
H4 ⁽⁰⁰⁾	2.72	8.23	≈ 14	0.0327	1.4×10^{-3}	0.132	1565	2552
SLy ₁₀ ^(↑↑)	2.68	8.55	≈ 16	0.0320	2.2×10^{-4}	0.169	2030	3328
ALF2 ₁₀ ^(↑↑)	2.69	8.72	≈ 16	0.0322	1.3×10^{-3}	0.146	1743	2680
H4 ₁₀ ^(↑↑)	2.73	8.97	≈ 15	0.0327	1.2×10^{-3}	0.134	1579	2504
SLy ₁₅ ^(↑↑)	2.68	8.85	≈ 17	0.0318	8.7×10^{-4}	0.170	2035	3272
ALF2 ₁₅ ^(↑↑)	2.69	9.09	≈ 16	0.0319	4.9×10^{-4}	0.147	1751	2688

Table 7.3: Properties of the BNS mergers. The table lists: name of the configuration, ADM mass M_{ADM} and angular momentum J_{ADM} , the number of orbits N_{orb} , the dimensionless initial GW frequency ($M\omega_{22}$), the mass of the ejecta (M_{ej}), the dimensionless gravitational merger frequency $M\omega_{\text{mrg}}$, merger frequency (f_{mrg}) in Hz and the postmerger peak frequency (f_2) in Hz.

Gravitational waves

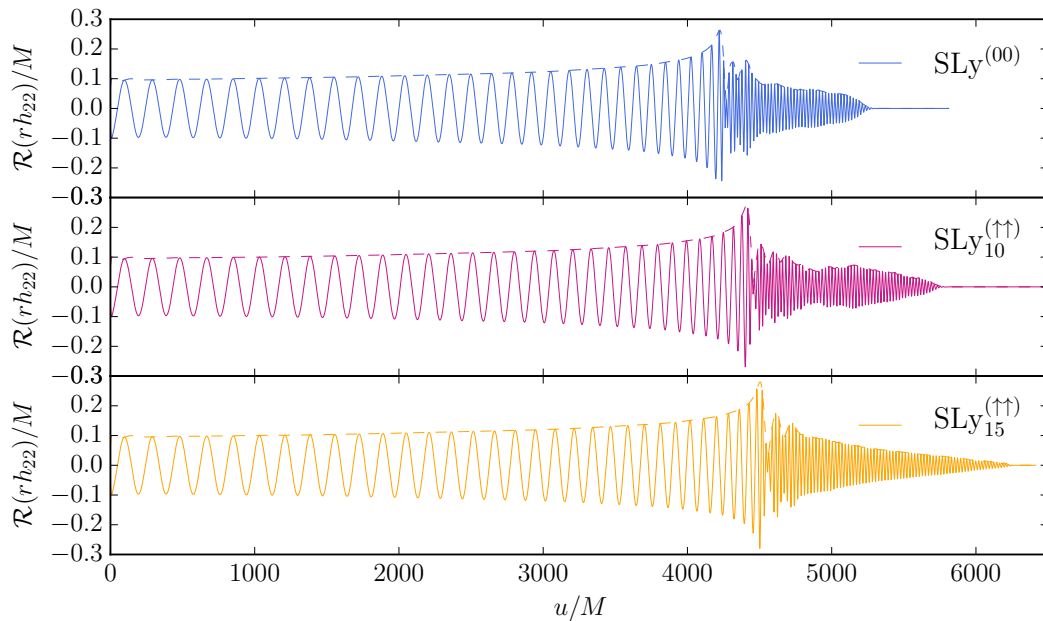


Figure 7.9: Real part of the (2, 2) mode of the GW strain (rh_{22}) versus retarded time u/M rescaled by total mass for SLy⁽⁰⁰⁾ (blue), SLy₁₀^(↑↑) (pink) and SLy₁₅^(↑↑) (orange) configurations.

To investigate the effects of spin on the GWs, we compute GWs signal following the Ref. [172]. We extract GWs at $r = 900M_{\odot}$ and present our results for ($l = m = 2$) multipole in Figs. (7.9, 7.10 and 7.11) for all the configurations listed in Tab. 7.2.

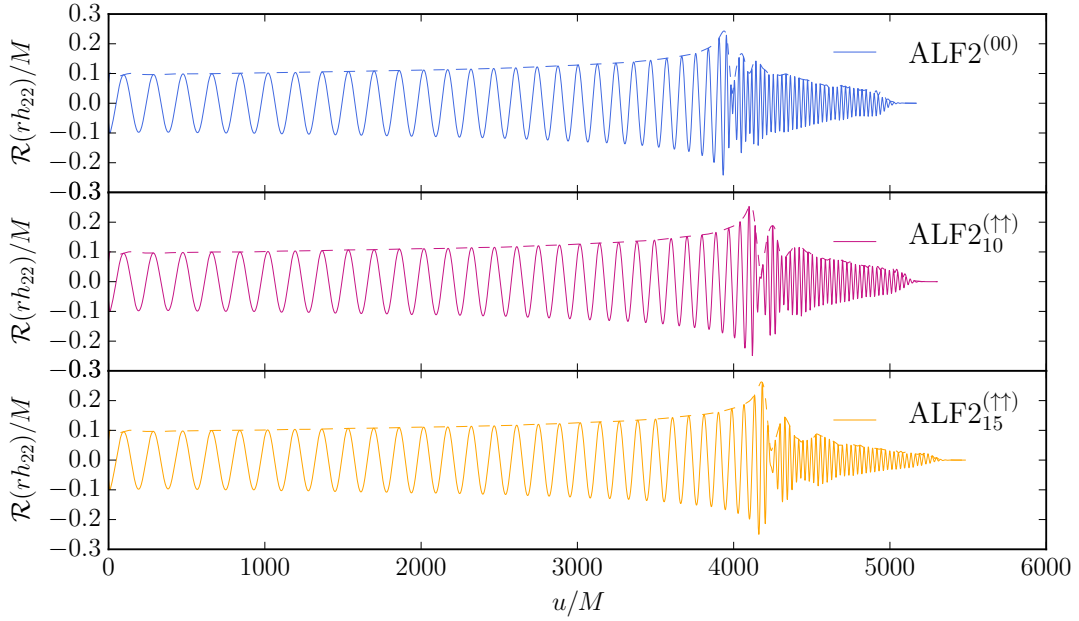


Figure 7.10: Real part of the (2, 2) mode of the GW strain (rh_{22}) versus retarded time u/M rescaled by total mass for $\text{ALF2}^{(00)}$ (blue), $\text{ALF2}_{10}^{(\uparrow\uparrow)}$ (pink) and $\text{ALF2}_{15}^{(\uparrow\uparrow)}$ (orange) configurations.

The figures show the real part of the GW strain for the (2, 2) mode and its amplitude as a function of retarded time u rescaled by total mass M . We observe that the number of orbit before merger increase as the spin (aligned to the orbital angular momentum) given in Tab. 7.3. Particularly, the configuration $\text{SLy}_{15}^{(\uparrow\uparrow)}$ with $\chi_{A,B} = 0.238$, has ~ 6 additional GW cycles and $\text{SLy}_{10}^{(\uparrow\uparrow)}$ has three additional cycles as compared to the irrotational case ($\text{SLy}^{(00)}$). The high spin configuration ($\text{ALF2}_{15}^{(\uparrow\uparrow)}$) with $\chi_{A,B} = 0.29$ also has three additional GW cycle than $\text{ALF2}_{10}^{(\uparrow\uparrow)}$ setup which has spin $\chi_{A,B} = 0.187$. As compared to the irrotational case for ALF2 EOS ($\text{ALF2}^{(00)}$), the spinning system $\text{ALF2}_{10}^{(\uparrow\uparrow)}$ has ~ 2 additional GW cycles. For configurations with stiff EOS, $\text{H4}_{10}^{(\uparrow\uparrow)}$ has ~ 4 additional GW cycle as compared to the irrotational case $\text{H4}^{(00)}$. We find that the configuration with stiff EOS has less GW cycle before merger than setups with soft EOSs. We compare the NR waveforms with the EOB waveforms for (2, 2) mode. We employ TEOBResumS^{11} waveform model for generating the EOB waveform. We show comparison for the spinning configurations in Fig. 7.12, where the blue curve is NR data, pink dashed curve is the EOB data and orange curve is the phase difference in the NR and EOB. We align both waveforms in early inspiral, i.e., before $u \leq 1500M$ for comparison. We found that the phase difference is getting higher around 2–3 orbits before the merger and it is about 1–2 radian at the merger

We investigate the post-merger spectrum of the GWs using Fourier transformation. Figs. (7.13, 7.14 and 7.15) show the PSD of all signals with markers for the merger and peak postmerger frequencies¹². We list some of the important quantities

¹¹We use version v1.0 of the TEOBResumS code.

¹²Here, we only report the f_2 which is the dominant frequency in (2,2) mode after the merger

like merger frequency in Hz (f_{mrg}), and in dimensionless and mass rescaled units ($M\omega_{\text{mrg}}$), and peak postmerger frequency (f_2) in Hz in Tab. 7.3.

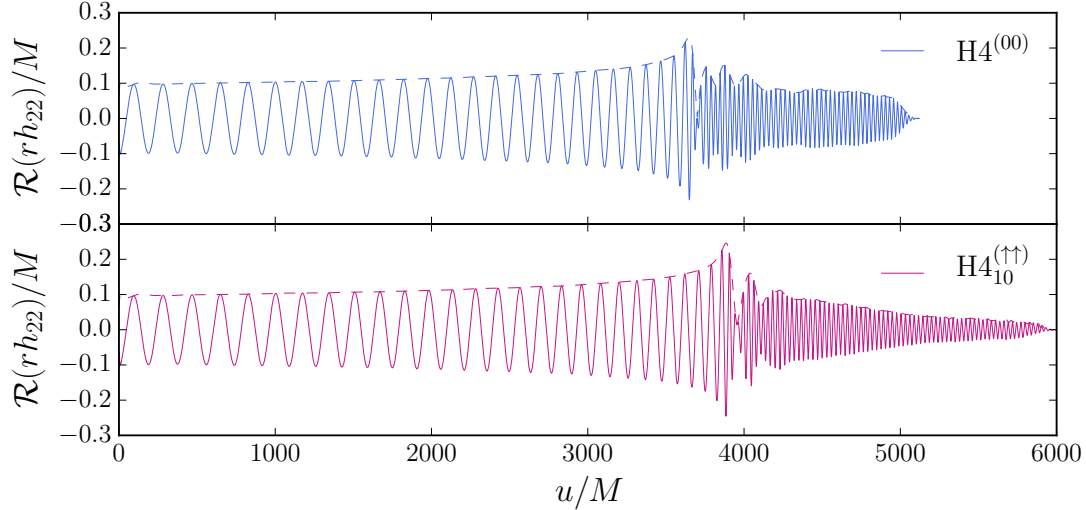


Figure 7.11: Real part of the (2, 2) mode of the GW strain (rh_{22}) versus retarded time u/M rescaled by total mass for $H4^{(00)}$ (blue) and $H4_{10}^{(\uparrow\uparrow)}$ (pink) configurations.

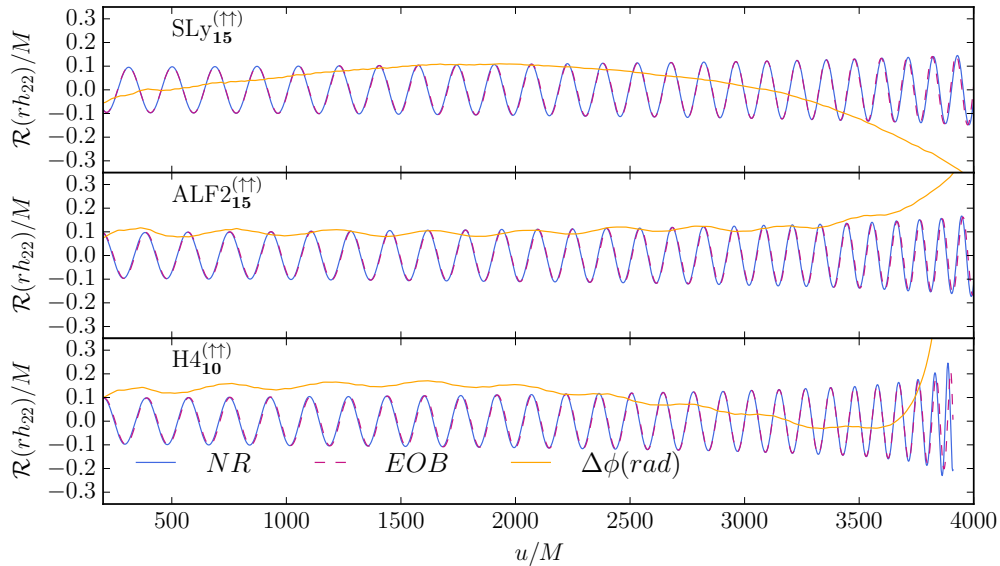


Figure 7.12: Comparison between real part of (2, 2) mode of the GW strain rh_{22} with TEOBResumS waveforms for the spinning configurations listed in Tab. 7.2. The EOB and NR waveforms are aligned during the early inspiral. The phase difference is shown as orange curve. The difference is larger around 3-4 cycles before the merger. The phase difference is larger for the stiff EOS H4 setup than for soft EOS setups at the merger.

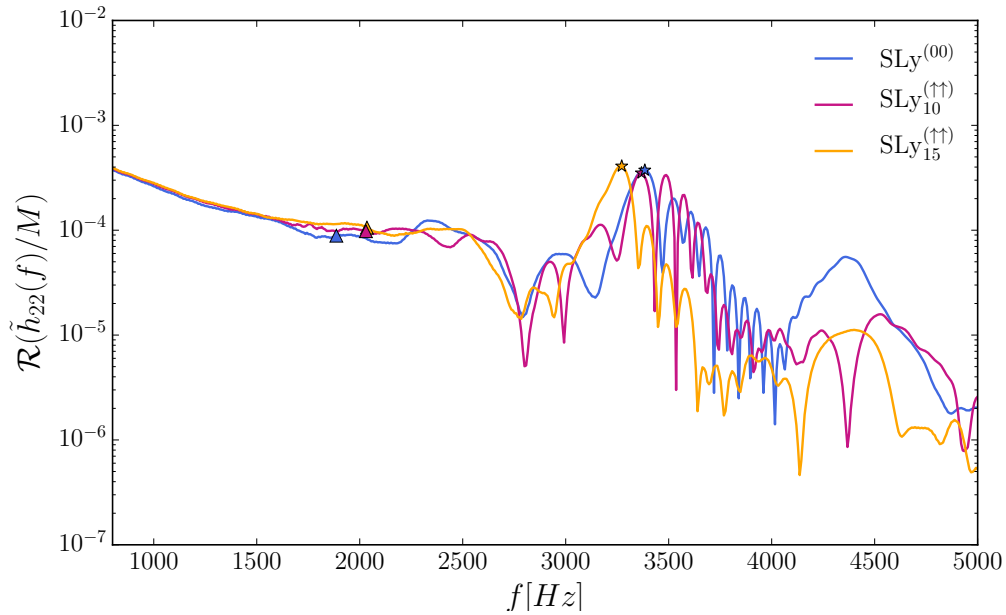


Figure 7.13: Fourier transform of time domain waveforms of $\text{SLy}^{(00)}$ (blue), $\text{SLy}_{10}^{(\uparrow\uparrow)}$ (pink) and $\text{SLy}_{15}^{(\uparrow\uparrow)}$ (orange) configurations. The markers for merger frequency (f_{mrg}) are triangles and postmerger peak frequency (f_2) are stars.

We find that the merger frequency moves to higher value as spin (aligned) increases. The configurations with soft EOS have higher merger frequency as compared to the setups with stiff EOS. The shift in the merger frequency $M\omega_{\text{mrg}}$ is about ± 0.01 where the exact value depends on the EOS and spin [166]. The irrotational cases have a faster phase evolution, i.e. merger at lower frequency as compared to the spinning configurations, this happens due to the *spin orbit* effect [185]. However, the observation for f_2 is opposite, i.e., it moves to lower value with aligned spins which is in agreement with the findings of Refs. [166, 178]. We find that the configurations with aligned spin have remnant with a longer lifetime, therefore collapse to a final BH would be delayed in such scenarios. We also find that the stiff EOS, namely, H4, supports the remnant for an even longer time as compared to configurations with soft EOS. Although, the system with stiff EOS has smaller merger frequency f_{mrg} .

In summary, we evaluated the performance of the *new* SGRID code by comparing initial data sequences computed for equal and unequal mass systems with and without spins using *new* and *old* SGRID code. We employed $E_b(\ell)$ - curves to study the initial data sequences. We also dynamically evolved the initial data for the same configuration computed using both SGRID codes and compared their GW, Hamiltonian, and momentum constraints. We found that the performance of the *new* SGRID code is comparable to the *old* code. With the new improvement in the SGRID code, now it is possible to compute initial data for high compactness, high mass-ratios, and high spins configurations.

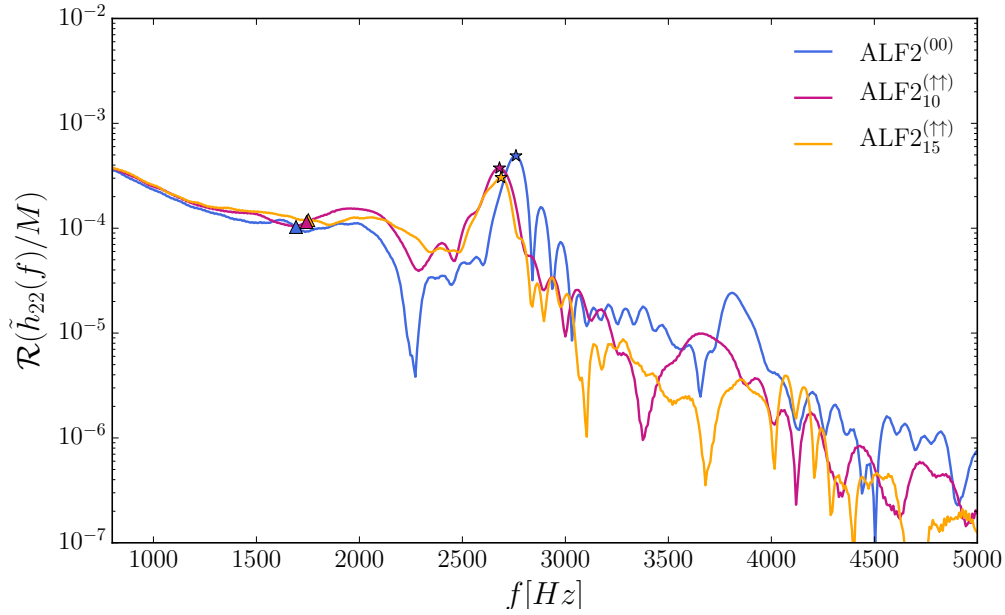


Figure 7.14: Fourier transform of time domain waveforms of ALF2⁽⁰⁰⁾ (blue), ALF2₁₀^($\uparrow\uparrow$) (pink) and ALF2₁₅^($\uparrow\uparrow$) (orange) configurations. The markers for merger frequency (f_{mrg}) are triangles and postmerger peak frequency (f_2) are stars.

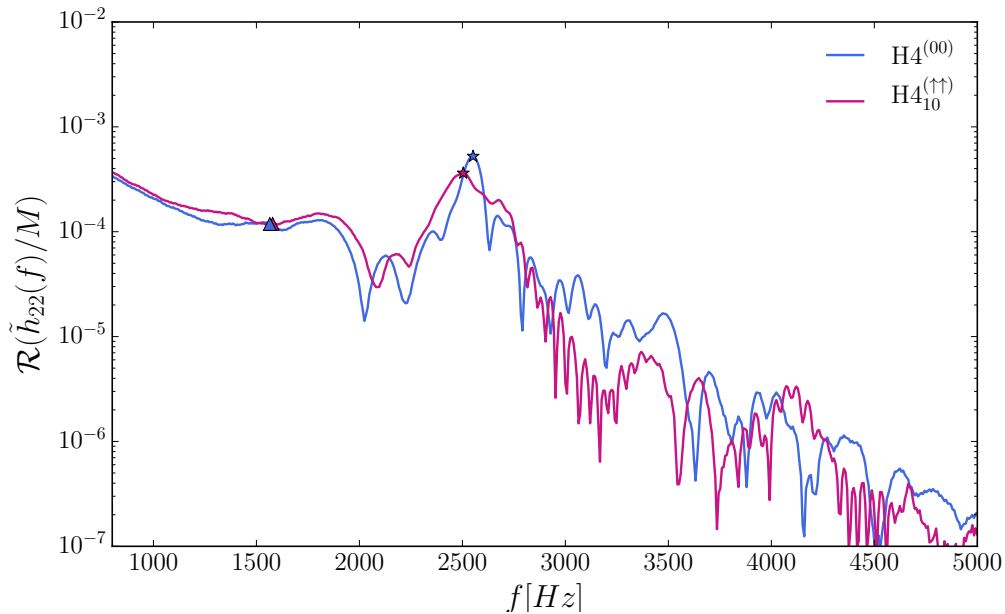


Figure 7.15: Fourier transform of time domain waveforms of H4⁽⁰⁰⁾ (blue) and H4₁₀^($\uparrow\uparrow$) (pink) configurations. The markers for merger frequency (f_{mrg}) are triangles and postmerger peak frequency (f_2) are stars.

We also show intermediate results for highly spinning BNS merger simulations. We analyzed the simulated data using $E_b(\ell)$ -curves. We report ejecta properties, GWs and post-merger spectrum. We compare these properties of spinning setups with irrotational cases to infer the effects of spin on dynamics. These results are

part of a study where we want to decouple all the spin effects and understand the effect of spins and EOS on the dynamics. In the near future, we plan to perform more simulations with one star has aligned and another star has anti-aligned spin with respect to the orbital angular momentum ($\uparrow\downarrow$), and both stars have anti-aligned spins with respect to the orbital angular momentum ($\downarrow\downarrow$) in order to decouple all the spin effects like spin-spin interactions, spin-orbit, and self-spin effects. For placing the error bars, more simulations with different resolutions are required. Therefore, numerical simulations with very high spinning NSs aligned and anti-aligned to the orbital angular momentum with different resolutions are undergoing [Dudi6].

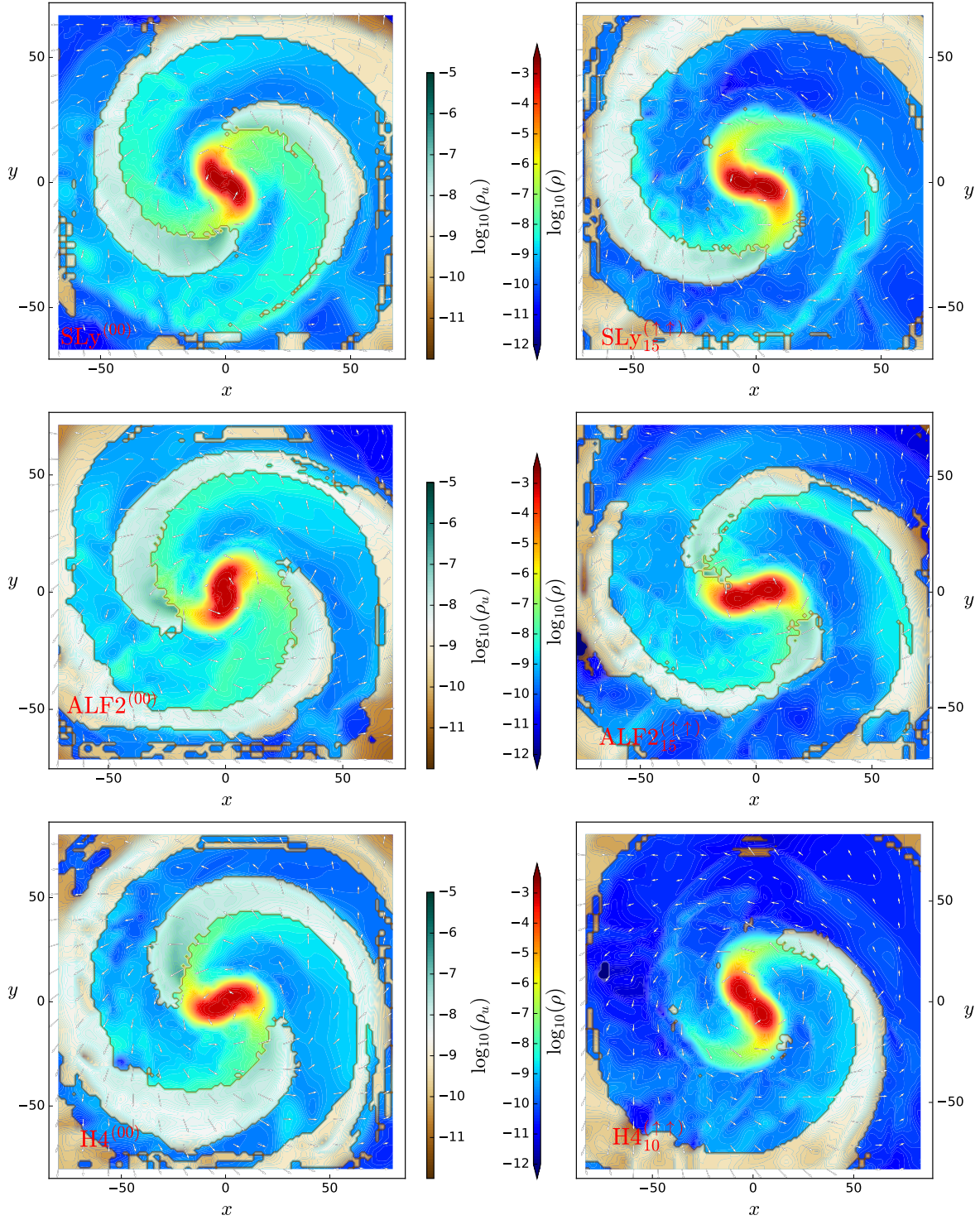


Figure 7.16: Snapshots of bound rest-mass density ($\log_{10}(\rho)$), unbound rest-mass density ($\log_{10}(\rho_u)$) and fluid's velocity (v^x, v^y) across the orbital plane around the merger. For configurations: Left panel (from top to bottom): SLy⁽⁰⁰⁾, ALF2⁽⁰⁰⁾, H4⁽⁰⁰⁾. Right panel (from top to bottom): SLy₁₅^(↑↑), ALF2₁₅^(↑↑), H4₁₀^(↑↑).

Chapter 8

Conclusion

In this thesis, we investigated gravitational waveform models and incorporated improvements to some models. We provided hybrid waveforms for BNS by stitching an inspiral regime waveform to a NR simulation waveform for the same parameters, available publicly on the CoRe database. The hybrids are constructed for a range of parameters; equal and unequal mass systems with spinning and non-spinning cases, which help in validating the waveform models. The major applications of hybrid waveforms are in assessing the accuracy of models via performing mismatch calculations. To further test the waveform models, parameter estimation can be performed where hybrid waveforms can be injected in place of a real signal in the fiducial data stream. We presented examples of all these applications in different chapters. With the use of hybrid waveforms, we also studied systematics among various waveform models generally employed for parameter estimation purposes. Before the detection of GW170817, the first BNS merger, we wanted to explore the following two questions in the presence of a true BNS signal:

(i) *What is the impact of neglecting tidal effects in the analysis of the inspiral GW signal?*

(ii) *Does the use of inspiral-only waveforms lead to a significant loss of information, or possibly to biases in the estimation of the source properties?*

We injected hybrid waveforms as a full BNS signal in the data stream of LIGO observatory and estimated parameters for eight injection scenarios, which covers two different EOS, two different injected SNR, different sampling rate, and two different noise PSD. We employed six different waveform models with and without tidal interactions to estimate the parameters in order to understand the systematic differences in models. We found that for a typical observation, i.e., $\text{SNR} \sim 25$ and a fairly soft EOS ($\tilde{\Lambda} \sim 400$) even the usage of BBH models does not bias the measurement of mass and spin parameter. Though, as the EOS gets stiffer and SNR gets higher, there will be significant bias in the measured value. We also found that $\text{TaylorF2}_{\text{Tides}}$ is estimating a higher value of tidal parameter than expected and thus

can be used to place an upper bound on tidal deformability. Later, we also tried to explain this behavior of $\text{TaylorF2}_{\text{Tides}}$ using Q_ω -analysis intuitively. We also found that NRTidal models, which are used to convert any BBH model into BNS model, underestimate the tidal deformability at high SNR. These investigations suggested that there is an immediate need to improve these waveform models as we do not have sufficient command on waveforms at high SNRs and with upcoming advanced detectors and 3G detectors we expect to have BNS observations with high SNR and high mass ratios and high spins possibly. We then worked on the improvement of these models, namely, TaylorF2 and NRTidal . We tested the improved point-mass baseline of TaylorF2 from 3.5 PN to quasi 5.5 PN. We performed Q_ω -analysis to compare both and found that the phase evolution of TaylorF2 at quasi 5.5 PN is closer to the state-of-the-art EOB model. We also performed the parameter estimation study, again by injecting hybrid waveforms in the LIGO data stream and recovering using $\text{IMRPhenomD_NRTidal}$, $\text{TaylorF2}_{\text{Tides}}$ at 3.5 PN baseline and quasi 5.5 PN. We found that the results obtained with $\text{IMRPhenomD_NRTidal}$ and $\text{TaylorF2}_{\text{Tides}}$ at quasi 5.5 PN are in agreement with each other and with the injected value, and that $\text{TaylorF2}_{\text{Tides}}$ at quasi 5.5 PN is twice as fast as $\text{IMRPhenomD_NRTidal}$ while there were some biases in $\text{TaylorF2}_{\text{Tides}}$ at 3.5 PN results. Hence we recommend the use of $\text{TaylorF2}_{\text{Tides}}$ at quasi 5.5 PN model for searches as well as parameter estimation purposes. This new model is getting reviewed at the time of writing this thesis. For improved NRTidalv2 model, we supplied the hybrid waveforms, which are used for improving the fit and computing the fitting coefficients, validating the model, and also evaluating its performance by performing mismatch calculations.

We then reviewed surrogate modeling techniques in the context of delivering a compact, accurate, and fast-to-evaluate waveform model. We applied the method on multipolar tidal EOB model TEOBResum and showed that the final surrogate model is 300 times faster than the original model with negligible loss of accuracy. We also tried to apply the same methods for the TEOBResumS model, which includes tidal and spin effects. Due to dimensionality issues, we found that the techniques cannot be directly applied. Nevertheless, we proposed a possible solution to this problem.

Furthermore, we had a preliminary study of high spin BNS systems using NR simulations. In order to probe the late inspiral, merger, and post-merger dynamics of a BNS merger with high spins. We perform numerical simulations of highly spinning BNS by employing BAM code to evolve the initial data. Our colleagues have developed a formalism (*new* SGRID) to construct BNS initial data, in principle, with arbitrary masses, spins, and eccentricities. We construct initial data using the *new* SGRID code, for which the performance was also checked by evaluating the results computed with the *old* and *new* code. We analyzed the numerical simulations via $E_b(\ell)$ - curves as they are gauge-invariant quantity. We investigated the ejecta properties, post-merger properties, and GWs for high spin BNS mergers. We

presented results of the evolution of highly spinning BNS (up to dimensionless spin $\chi_{A,B} = 0.29$) with full (3+1)D numerical relativity simulations using consistent initial conditions. These are among the highest spinning numerical evolutions of BNS to date. These waveforms with high resolution can be used as a testbed to extract the spin effects in the GW phase evolution and to test other semi-analytical waveform models.

Future work

We want to propose the next steps to undertake in the near future:

- A detailed waveform systematics study needs to be done in order to understand the degeneracy among spins, tides, and mass parameters with new models and injections with different mass ratios and spins.
- Apply the proposed reduced-order modeling techniques in the context of a surrogate model for `TEOBResumS`, such that it can be employed for the parameter estimation purposes.
- Perform more numerical simulations with high resolutions and different spin values in order to understand and separate the spin-spin effects, spin-tide effects in order to provide a testbed for modeling these effects.

With the motivation to contribute to future BNS detections, we propose a full BNS waveform model, including inspiral, merger, and post-merger regime. The idea is to generate enough hybrid waveforms and make a surrogate model using hybrid waveforms as the training set. Having such a model will be essential for the data analysis of the third generation (and advance LIGO) detectors as we expect to observe all the regimes of the waveforms in the future.

Appendix

Appendix A

Quasi-5.5PN-accurate orbital phasing

Building upon Damour et al. [131], Ref. [127] illustrated how to formally obtain a high-order PN approximant by PN-expanding the EOB energy E_{EOB} and energy flux \mathcal{F}_{EOB} along circular orbits. Stopping the expansion at 4.5 PN, allowed one to obtain a consistent 4.5 PN approximant with a few parameters needed to formally take into account the yet uncalculated ν -dependent terms in the waveform amplitudes at 4 PN. Here we follow precisely that approach, but we extend it to 5.5 PN accuracy. To get the waveform phase in the frequency domain along circular orbits, we start with the gauge-invariant¹ description of the adiabatic phasing and is given by the function

$$Q_\omega \equiv E_{\text{EOB}}(x) \left(\frac{d\mathcal{F}_{\text{EOB}}}{dx} \right)^{-1}, \quad (\text{A.1})$$

where $x \equiv (M\Omega)^{2/3}$, with Ω the orbital frequency along circular orbits. The high-order phasing approximant is obtained by Taylor-expanding the above equation and then by solving the equation

$$\frac{d^2\Psi_{5.5\text{PN}}}{d^2\hat{f}} = \frac{Q_\omega(\hat{f})}{\hat{f}^2}, \quad (\text{A.2})$$

where $\hat{f} \equiv Mf \equiv \Omega/2\pi$. The double integration of Eq. (A.2) delivers $\Psi_{5.5\text{PN}}(\hat{f})$ modulo an affine part of the form $p + q\hat{f}$, where (p, q) are two arbitrary integration constants that are fixed to be consistent with the usual conventions adopted in the literature for the 3.5 PN approximant [186].

We consider here only *nonspinning* binaries (the reader is referred to Appendix B of the Ref. [187] for the discussion of the spin case). The corresponding, circularized, EOB Hamiltonian reads $H_0^{\text{EOB}} = M\sqrt{1 + 2\nu(\hat{H}_{\text{eff}} - 1)}$ where $\hat{H}_{\text{eff}} \equiv H_{\text{eff}}/\mu = \sqrt{A(u)(1 + u^2j^2)}$, where j is the orbital angular momentum along circular orbits, $u \equiv M/R$ the inverse radial separation and $A(u)$ is the EOB interaction potential kept with a 5 PN term $\nu(a_6^c + a_6^{\text{ln}} \ln u)u^6$ with a_6^c an analytically unknown coefficient.

¹In the sense that it is independent of time and phase arbitrary shifts.

The orbital angular momentum along circular orbits j is obtained solving $\partial_u \hat{H}_{\text{eff}} = 0$. By PN-expanding one of Hamilton's equations, $M\Omega = \partial_\varphi H^{\text{EOB}}$, one obtains $x(u)$ as a 5 PN truncated series in u , that, once inverted, allows to obtain the (formal) 5.5 PN accurate energy flux as function of x by PN-expanding its general EOB expression $\mathcal{F} = \sum_{\ell=2}^{\infty} \sum_{\ell=-m}^m F_{\ell m}^{\text{Newt}} \hat{F}_{\ell m}$, where $F_{\ell m}^{\text{Newt}}$ is the Newtonian (leading-order) contribution and $\hat{F}_{\ell m}$ is the relativistic correction. Each multipolar contribution within the EOB formalism comes written in factorized and resummed form as

$$\hat{F}_{\ell m} = \left(\hat{S}_{\text{eff}}^{(\epsilon)} \right)^2 |T_{\ell m}|^2 (\rho_{\ell m})^{2\ell}. \quad (\text{A.3})$$

Here, $\hat{S}_{\text{eff}}^{(\epsilon)}$ is the effective source, that is the effective EOB energy $\hat{E}_{\text{eff}}(x) \equiv E_{\text{eff}}/\mu$ when $\epsilon = 0$ ($\ell + m = \text{even}$) or the Newton-normalized orbital angular momentum when $\epsilon = 1$ ($\ell + m = \text{odd}$). The squared modulus of the tail factor $T_{\ell m}$ resumes an infinite number of PN hereditary logarithms [188, 189]. We use the relativistic residual amplitude ($\rho_{\ell m}$) information reported in Eqs (7)-(18) of Ref. [127], where the unknown high PN coefficients (polynomials in ν) have been parameterized by some coefficients $c_{\ell m}$. We include for consistency all the coefficients to go up to the $\ell = 7$, $m = \text{even}$ multipoles.

From Eq. (A.1) one obtains the following PN-expanded expression

$$\begin{aligned} \hat{Q}_\omega^{\text{PN}} = & 1 + b_2 x + b_3 x^{3/2} + b_4 x^2 + b_5 x^{5/2} \\ & + b_6 x^3 + b_7 x^{7/2} + b_8 x^4 + b_9 x^{9/2} + b_{10} x^5 + b_{11} x^{11/2}. \end{aligned} \quad (\text{A.4})$$

The coefficients of this expansion, that are reported in full in Appendix C of the Ref. [187], have the structure $b_i \equiv b_i^0 + b_i(\nu)$, where b_i^0 is the ν -independent (test-particle) part, fully known analytically, while the $b_i(\nu)$ encode the ν -dependence that is completely known at 3PN, while only partially known at 4 PN because the corresponding waveform calculation is not completed yet. The ν -dependence beyond 3PN is formally incorporated by extending the analytically known $\rho_{\ell m}$ function with additional ν -dependent coefficients and then reflects in the coefficients $b_i(\nu)$. Among these coefficients, those that depend on the parameters that we have introduced in the computation are

$$b_8 = b_8(c_{21}^{3\text{PN}}, c_{22}^{4\text{PN}}) \quad (\text{A.5})$$

$$b_{10} = b_{10}(c_{21}^{3\text{PN}}, c_{22}^{4\text{PN}}, c_{22}^{5\text{PN}}) \quad (\text{A.6})$$

$$b_{11} = b_{11}(c_{21}^{3\text{PN}}, c_{22}^{4\text{PN}}). \quad (\text{A.7})$$

In the following analysis, we fix to zero a_6^c as well as all the yet uncalculated, ν -dependent, PN waveform coefficients entering Eq. (A.4) above. This entitles us to use the definition of *quasi-5.5 PN* approximant (this PN-order choice is discussed

in Appendix A and resumed in Fig. 7 of Ref. [187]). Note however that in the NR-informed EOB model, that we shall use to check the reliability of this quasi-5.5 PN approximant, all the waveform coefficients are equally fixed to be zero; on the contrary, a_6^c is informed by NR simulations and, as such, effectively takes into account, to some extent, all this missing analytical information. The importance of the ν -dependent waveform coefficients is, a priori, expected to be low, as suggested in Tab. II of [190]. This is in accord with the fact that an eventual tuning of some free parameters is better when they tend to be small.

Appendix B

Algorithms for Surrogate model

Greedy algorithm to construct a reduced basis

1. **Input** $Y(\cdot; \theta)$, θ , ϵ
 2. Set $i = 0$ and define $\sigma_0 = 1$
 3. **Seed choice** (arbitrary): $\mu_1 \in \mathcal{T}$, $e_1 = Y(\cdot, \mu_1)$
 4. $\text{RB} = e_1$
 5. **while** $\sigma_0 \geq \epsilon$
 6. $i = i+1$;
 7. $\sigma_i = \max_{\theta \in \mathcal{T}} \|Y(\cdot; \theta) - \mathcal{P}_i Y(\cdot; \theta)\|^2$
 8. $\mu_{i+1} = \operatorname{argmax}_{\theta \in \mathcal{T}} \|Y(\cdot; \theta) - \mathcal{P}_i Y(\cdot; \theta)\|^2$
 9. $e_{i+1} = Y(\cdot; \mu_{i+1}) - \mathcal{P}_i Y(\cdot; \mu_{i+1})$
 10. $e_{i+1} = e_{i+1} / \|e_{i+1}\|$
 11. $\text{RB} = \text{RB} \cup e_{i+1}$
 12. **end while**
 13. Set $n=i$
 14. Output $\text{RB} = \{e_i\}_{i=1}^n$ and greedy points $\{\mu_i\}_{i=1}^n$
-

Table B.1: The table is taken from Ref. [83].

Greedy algorithm to construct a reduced basis:

We do not work with the real and imaginary part of the GW strain h , rather with the amplitude and phase, as already explained in the text, they vary less with parameters (θ) and time (t). Therefore, we build a reduced basis as well as empirical interpolant separately for amplitude and phase and then combine both using Eq. (6.22). Assuming all the training set amplitudes/phases are functions in the given parameter space. Then, we would like to construct a basis such that any function in the parameter space is a linear combination of this reduced basis. We specify a tolerance (ϵ) such that upto this tolerance, only the projection \mathcal{P} of any function onto the reduced basis will be different from the original function. The algorithm is sketched in Tab. B.1, which terminates after n iterations when the projection error is smaller than the specified tolerance. We use $\|\cdot\|^2$ notation for L_2 norm. We employ iterated

and modified Gram Schmidt process to construct an orthonormal basis vector. We choose the first function as our first reduced basis (any function in the training set can be chosen). Then, we project all functions on this basis and compute the projection error (line 7 in Tab. B.1). The function with the maximum projection error is our next basis. We then iterate and calculate the projection error using two basis vector. We keep on iterating until the projection error is smaller than the specified tolerance. More details about the greedy algorithm are discussed in Ref. [136]. The algorithm outputs n reduced basis $\{e_i\}_{i=1}^n$ and greedy points $\{\mu_i\}_{i=1}^n$.

Greedy algorithm for constructing Empirical interpolant:

Once we have reduced the data in parameters (θ), then we reduce it in time (t), by building empirical interpolant $\mathcal{I}_n[\cdot]$. As already described in the text, the interpolant is uniquely defined for the particular reduced basis and will reproduce the function on all-time samples when its value is given on the specified empirical nodes τ_j . The empirical node τ_1 is the time point at which the absolute value of the first basis is the highest. The key idea is that the interpolant is a linear combination of the first n basis, then for the first basis, the interpolant is given by Eq. (6.14), and then we demand that at the empirical node τ the interpolant reproduce the data. Then, using Eq. (6.15), we obtain the coefficient and interpolant for generating the first basis. We try to interpolate the second basis with this interpolant and the time sample with the maximum error, will be our next empirical node τ_2 , Eq. (6.16). Similarly, as described in the text, we keep on iterating until all the reduced basis is exhausted. The algorithm is given in Tab. B.2 and discussed in detailed in Ref. [136]. The algorithm outputs empirical nodes $\{\tau_i\}_{i=1}^n$ and interpolant \mathcal{I}_n .

Algorithm for constructing Empirical Interpolant

1. **Input** $\{e_i\}_{i=1}^n, t := \{t_i\}_i^L$
 2. $i = \mathit{argmax}|e_1(t)|$ (it returns the largest value over all time samples)
 3. **Set** $\tau_1 = t_i$
 4. **for** $j = 2 \rightarrow n$ **do**
 5. **Build** $\mathcal{I}_{j-1}[e_j](t)$ **from**
 6. $\vec{r} = \mathcal{I}_{j-1}[e_j](t) - e_j(t)$
 7. $i = \mathit{argmax}|\vec{r}|$
 8. $\tau_j = t_i$
 9. **end for**
 13. **Set** $n=i$
 14. **Output** EI nodes = $\{T_i\}_{i=1}^n$ and interpolant operator \mathcal{I}_n
-

Table B.2: The table is taken from Ref. [83].

Appendix C

SGRID

We assume the matter inside the stars to be perfect fluid and the stress energy tensor is given by:

$$T^{\mu\nu} = [\rho_0(1 + \epsilon) + P]u^\mu u^\nu + P g^{\mu\nu}. \quad (\text{C.1})$$

where ρ_0 is the mass density, P denotes pressure, u^μ is 4-velocity and ϵ denotes the internal energy density divided by ρ_0 . For the polytropic EOS:

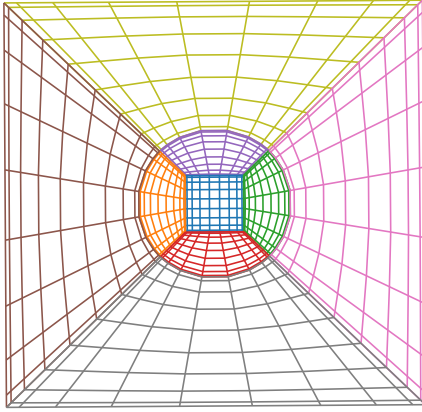
$$P = \kappa \rho_0^{1+1/n}, \quad (\text{C.2})$$

where n is the polytropic index and κ is a constant; the pressure, mass density, which is proportional to baryon number density and the internal energy can be written in terms of specific enthalpy h .

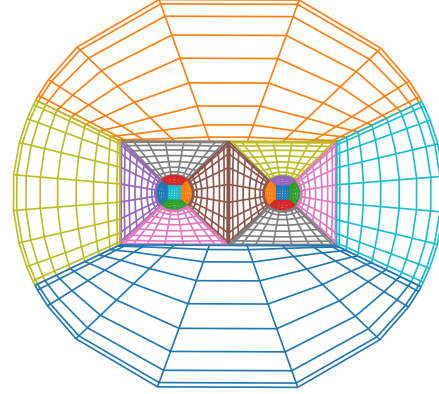
$$h = 1 + \epsilon + P/\rho_0. \quad (\text{C.3})$$

We use several domains to cover the stars and space around the stars, such that domains boundaries coincide with the star surface. Each domain described by its own coordinates. This is crucial as at the surface, where ($h = 1$), the pressure, ϵ and ρ_0 becomes non-differentiable though the matter inside is smooth. In the *old* SGRID, this problem was handled using Ansorg's coordinate (A, B, ϕ) described in Ref. [99] and depicted in Fig. 1 of the Ref. [99]. Only six computational domains were needed to cover all of the space. The coordinate transformation contains freely specifiable functions $\sigma_\pm(B, \phi)$ that can be chosen such that the domain boundaries adapt the star surface. Tichy et al. [Dudi5] have upgraded the SGRID code such that it is capable of constructing initial data for BNS with extreme properties. In the *new* SGRID, we use surface fitted cubed sphere coordinates (λ, A, B) , which has no singularities anywhere. Here, we use several domains to cover the star and its surroundings, e.g., the star is covered by cube in the center, which is surrounded by cubed sphere wedges, as shown in Fig. C.1a. The surroundings are covered by multiple domains, which together cover a large cube.

Figure C.1b shows how two such larger cubes as in Fig. C.1a can be put next to



(a) The plot shows some domains and their coordinate lines in the xy -plane. Plotted are the domains inside and around neutron star 1. The star is roughly spherical and covered by a central cube and six cubed sphere wedges, four of which are shown because they intersect the xy -plane. The space around the star is covered by six more domains to form a larger cube. The plot is taken from [Dudi5].



(b) The plot shows the domains in and around both stars augmented by several more domains. The result is a large sphere that covers both stars and their surroundings. The plot is taken from [Dudi5].

each other, and in turn be surrounded by more wedges so as to cover a large sphere. The conformal thin sandwich approach [99, 164, 165] is employed to construct quasi-equilibrium constraint solved initial data for which the following assumptions are required. We write the fluid 4-velocity u^μ in terms of the 3-velocity

$${}^{(3)}\tilde{u}^i = h\gamma_\nu^i u^\nu, \quad (\text{C.4})$$

which we separate into an irrotational piece $D^i\phi$ and a rotational piece w^i

$${}^{(3)}\tilde{u}^i = D^i\phi + w^i, \quad (\text{C.5})$$

where D_i is the derivative operator compatible with the 3-metric γ_{ij} .

Assumptions: The first assumption is the existence of an approximate symmetry vector ξ^μ , such that

$$\mathcal{L}_\xi g_{\mu\nu} \approx 0. \quad (\text{C.6})$$

For a spinning star, we assume

$$\gamma_i^\nu \mathcal{L}_\xi (\nabla_\nu \phi) \approx 0, \quad (\text{C.7})$$

as $\mathcal{L}_\xi u^\mu$ is non-zero. In order to have the rotational piece of the fluid velocity con-

stant along the world line of the star center, we assume

$$\gamma_i^\nu \mathcal{L}_{\frac{\nabla_\phi}{hu^0}} w_\nu \approx 0, \quad (\text{C.8})$$

and

$${}^{(3)}\mathcal{L}_{\frac{w}{hu^0}} w_i \approx 0 \quad (\text{C.9})$$

Moreover, we assume maximal slicing

$$\gamma_{ij} K^{ij} = 0 \quad (\text{C.10})$$

and conformal flatness

$$\gamma_{ij} = \psi^4 \delta_{ij} \quad (\text{C.11})$$

This results in a coupled system of partial differential equations (PDE):

$$\bar{D}^2 \psi + \frac{\psi^5}{32\alpha^2} (\bar{L}B)^{ij} (\bar{L}B)_{ij} + 2\pi\psi^5 \rho = 0, \quad (\text{C.12})$$

$$\bar{D}_j (\bar{L}B)^{ij} - (\bar{L}B)^{ij} \bar{D}_j \ln(\alpha\psi^{-6}) - 16\pi\alpha\psi^4 j^i = 0, \quad (\text{C.13})$$

$$\bar{D}^2(\alpha\psi) - \alpha\psi \left[\frac{7\psi^4}{32\alpha^2} (\bar{L}B)^{ij} (\bar{L}B)_{ij} + 2\pi\psi^4(\rho + 2S) \right] = 0, \quad (\text{C.14})$$

$$D_i \left[\frac{\rho_0 \alpha}{h} (D^i \phi + w^i) - \rho_0 \alpha u^0 (\beta^i + \xi^i) \right] = 0, \quad (\text{C.15})$$

and

$$h = \sqrt{L^2 - (D_i \phi + w_i)(D^i \phi + w^i)}. \quad (\text{C.16})$$

Here $(\bar{L}B)^{ij} = \bar{D}^i B^j + \bar{D}^j B^i - \frac{2}{3} \delta^{ij} \bar{D}_k B^k$, $\bar{D}_i = \partial_i$. While, in general, the rotational piece of the fluid velocity w^i can be chosen freely, we will use the from

$$w^i = \epsilon^{ijk} \omega^j (x^k - x_{C_*}^k) \quad (\text{C.17})$$

which as demonstrated in [155] results in almost rigidly rotating fluid configurations with low expansion and shear. The parameter $x_{C_*}^k$ denotes the location of the star center, and ω^j is an arbitrarily chosen vector that determines the star spin. Once the equations (C.12), (C.13), (C.14), (C.15) and (C.16) are solved we know h (and thus the matter distribution) and the fluid 3-velocity ${}^{(3)}\tilde{u}^i$ via Eq. (C.5). The 3-metric is obtained from Eq. (C.11) and the extrinsic curvature is given by

$$K^{ij} = \frac{1}{2\psi^4 \alpha} (\bar{L}\beta)^{ij}. \quad (\text{C.18})$$

For further details, we refer to Ref. [Dudi5].

Publications

- [Dudi1] R. Dudi, F. Pannarale, and T. Dietrich, M. Hannam, S. Bernuzzi, F. Ohme, B. Brügmann, *Relevance of tidal effects and post-merger dynamics for binary neutron star parameter estimation* Phys. Rev. D. 98 (2018) 084061, DOI: 10.1103/PhysRevD.98.084061 arXiv:1808.09749 [gr-qc].
- [Dudi2] F. Messina, R. Dudi, A. Nagar, S. Bernuzzi, *Quasi-5.5PN TaylorF2 approximant for compact binaries: point-mass phasing and impact on the tidal polarizability inference* Phys. Rev. D. 99 (2019) 124051, DOI:10.1103/PhysRevD.99.124051 arXiv:1904.09558 [gr-qc].
- [Dudi3] T. Dietrich S. Khan, R. Dudi, and others, *Matter imprints in waveform models for neutron star binaries: Tidal and self-spin effects* Phys. Rev. D. 99.024029, DOI:10.1103/PhysRevD.99.024029, arXiv:1804.02235 [gr-qc]
- [Dudi4] T. Dietrich, A. Samajhdar, S. Khan, N.K. Johnson McDaniel, R. Dudi, W. Tichy, *Improving the NRTidal model for binary neutron star system* Phys. Rev. D 100, 044003 (2019), DOI:10.1103/PhysRevD.100.044003 arXiv:1905.06011 [gr-qc].
- [Dudi5] W. Tichy, A. Rashti, T. Dietrich, R. Dudi, B. Brügmann, *Constructing binary neutron star initial data with high spins, high compactness and high mass-ratios* arXiv:1910.09690v1 [gr-qc].

Collaboration

- [Collab1] A. Abbott, Benjamin P. Benjamin and others, LIGO/Virgo Scientific collaboration, *GW170817: Observation of Gravitational Waves from a Binary Neutron Star Inspiral*, Phys. Rev. Lett.119 (2017) 161101, DOI:10.1103/PhysRevLett.119.161101, arXiv:1710.05832 [gr-qc].
- [Collab2] A. Abbott, Benjamin P. Benjamin and others, LIGO/Virgo Scientific collaboration, *Properties of the binary neutron star merger GW170817*, Phys.Rev.X.9 (2018) 011001, DOI:10.1103/PhysRevX.9.011001 arXiv:1805.11579 [gr-qc].
- [Collab3] T. Dietrich, D. Radice, S. Bernuzzi, F. Zappa, A. Perego, B. Brügmann, S V. Chaurasia, R. Dudi, W. Tichy, M. Ujevic, *CoRe database of binary neu-*

tron star merger waveforms and its application in waveform development, *Class. Quant. Grav.*35 (2018), arXiv:1806.01625 [gr-qc].

In Preparation

[Dudi6] R. Dudi, T. Dietrich, W. Tichy, B. Brügmann (2019), *Gravitational waves from mergers of highly spinning binary neutron stars*.

[Dudi7] R. Dudi, S. Bernuzzi (2019), *Reduced-order model for TEOBResumS model for binary neutron stars mergers*

Bibliography

- [1] P. Haensel, A. Y. Potekhin, and D. G. Yakovlev. *Neutron stars 1: Equation of state and structure*. New York, USA: Springer, 2007.
- [2] S. L. Shapiro and S. A. Teukolsky. *Black holes, white dwarfs, and neutron stars: The physics of compact objects*. New York, USA: Wiley, 1983.
- [3] J. B. Hartle. *An introduction to Einstein's general relativity*. San Francisco, USA: Addison-Wesley, 2003.
- [4] B. F. Schutz. *A First Course in General Relativity*. 2009.
- [5] M. Maggiore. *Gravitational Waves. Vol. 1: Theory and Experiments*. Oxford Master Series in Physics. Oxford University Press, 2007.
- [6] B. P. Abbott et al. "Observation of Gravitational Waves from a Binary Black Hole Merger". In: *Phys. Rev. Lett.* 116.6 (2016), p. 061102. DOI: 10.1103/PhysRevLett.116.061102. arXiv: 1602.03837 [gr-qc].
- [7] B. P. Abbott et al. "Multi-messenger Observations of a Binary Neutron Star Merger". In: *Astrophys. J.* 848.2 (2017), p. L12. DOI: 10.3847/2041-8213/aa91c9. arXiv: 1710.05833 [astro-ph.HE].
- [8] E. Annala et al. "Gravitational-wave constraints on the neutron-star-matter Equation of State". In: *Phys. Rev. Lett.* 120.17 (2018), p. 172703. DOI: 10.1103/PhysRevLett.120.172703. arXiv: 1711.02644 [astro-ph.HE].
- [9] F. J. Fattoyev, J. Piekarewicz, and C. J. Horowitz. "Neutron skins and neutron stars in the multi-messenger era". In: *Phys. Rev. Lett.* 120.17 (2018), p. 172702. DOI: 10.1103/PhysRevLett.120.172702. arXiv: 1711.06615 [nucl-th].
- [10] R. Nandi and P. Char. "Hybrid stars in the light of GW170817". In: *Astrophys. J.* 857.1 (2018), p. 12. DOI: 10.3847/1538-4357/aab78c. arXiv: 1712.08094 [astro-ph.HE].
- [11] S. De et al. "Constraining the nuclear equation of state with GW170817". In: (2018). arXiv: 1804.08583 [astro-ph.HE].

- [12] B. P. Abbott et al. “GW170817: Measurements of neutron star radii and equation of state”. In: *Phys. Rev. Lett.* 121.16 (2018), p. 161101. DOI: 10.1103/PhysRevLett.121.161101. arXiv: 1805.11581 [gr-qc].
- [13] B. P. Abbott et al. “A gravitational-wave standard siren measurement of the Hubble constant”. In: *Nature* (2017). DOI: 10.1038/nature24471. arXiv: 1710.05835 [astro-ph.CO].
- [14] B. P. Abbott et al. “GWTC-1: A Gravitational-Wave Transient Catalog of Compact Binary Mergers Observed by LIGO and Virgo during the First and Second Observing Runs”. In: (2018). arXiv: 1811.12907 [astro-ph.HE].
- [15] J. Aasi et al. “Advanced LIGO”. In: *Class. Quant. Grav.* 32 (2015), p. 074001. DOI: 10.1088/0264-9381/32/7/074001. arXiv: 1411.4547 [gr-qc].
- [16] F. e. a. Acernese. “Advanced Virgo: a second-generation interferometric gravitational wave detector”. In: *Class. Quant. Grav.* 32 (2014), p. 024001. DOI: 10.1088/0264-9381/32/2/024001. arXiv: 1408.3978 [astro-ph.HE].
- [17] S. W. Hawking and W. Israel. *Three Hundred Years of Gravitation Cambridge*. 1st pbk. corrected ed. Cambridge University Press, 1989.
- [18] B. S. Sathyaprakash and B. F. Schutz. “Physics, Astrophysics and Cosmology with Gravitational Waves”. In: *Living Rev. Rel.* 12 (2009), p. 2. arXiv: 0903.0338 [gr-qc].
- [19] E. E. Flanagan and T. Hinderer. “Constraining neutron star tidal Love numbers with gravitational wave detectors”. In: *Phys. Rev.* D77 (2008), p. 021502. DOI: 10.1103/PhysRevD.77.021502. arXiv: 0709.1915 [astro-ph].
- [20] T. Hinderer et al. “Tidal deformability of neutron stars with realistic equations of state and their gravitational wave signatures in binary inspiral”. In: *Phys. Rev.* D81 (2010), p. 123016. DOI: 10.1103/PhysRevD.81.123016. arXiv: 0911.3535 [astro-ph.HE].
- [21] T. Damour and A. Nagar. “Effective One Body description of tidal effects in inspiralling compact binaries”. In: *Phys. Rev.* D81 (2010), p. 084016. DOI: 10.1103/PhysRevD.81.084016. arXiv: 0911.5041 [gr-qc].
- [22] T. Binnington and E. Poisson. “Relativistic theory of tidal Love numbers”. In: *Phys. Rev.* D80 (2009), p. 084018. DOI: 10.1103/PhysRevD.80.084018. arXiv: 0906.1366 [gr-qc].
- [23] T. Hinderer. “Tidal Love numbers of neutron stars”. In: *Astrophys. J.* 677 (2008), pp. 1216–1220. DOI: 10.1086/533487. arXiv: 0711.2420 [astro-ph].
- [24] T. Damour and A. Nagar. “Relativistic tidal properties of neutron stars”. In: *Phys. Rev.* D80 (2009), p. 084035. DOI: 10.1103/PhysRevD.80.084035. arXiv: 0906.0096 [gr-qc].

- [25] M. Favata. “Systematic parameter errors in inspiraling neutron star binaries”. In: *Phys.Rev.Lett.* 112 (2014), p. 101101. DOI: 10.1103/PhysRevLett.112.101101. arXiv: 1310.8288 [gr-qc].
- [26] L. Wade et al. “Systematic and statistical errors in a bayesian approach to the estimation of the neutron-star equation of state using advanced gravitational wave detectors”. In: *Phys. Rev. D* 89.10 (2014), p. 103012. DOI: 10.1103/PhysRevD.89.103012. arXiv: 1402.5156 [gr-qc].
- [27] T. Damour, M. Soffel, and C.-m. Xu. “General relativistic celestial mechanics. 1. Method and definition of reference systems”. In: *Phys. Rev. D* 43 (1991), pp. 3273–3307. DOI: 10.1103/PhysRevD.43.3273.
- [28] T. Damour, M. Soffel, and C.-m. Xu. “General relativistic celestial mechanics. 2. Translational equations of motion”. In: *Phys. Rev. D* 45 (1992), pp. 1017–1044. DOI: 10.1103/PhysRevD.45.1017.
- [29] T. Damour, M. Soffel, and C.-m. Xu. “General relativistic celestial mechanics. 3. Rotational equations of motion”. In: *Phys. Rev. D* 47 (1993), pp. 3124–3135. DOI: 10.1103/PhysRevD.47.3124.
- [30] T. Damour, M. Soffel, and C.-m. Xu. “General relativistic celestial mechanics. 4: Theory of satellite motion”. In: *Phys. Rev. D* 49 (1994), pp. 618–635. DOI: 10.1103/PhysRevD.49.618.
- [31] E. Racine and E. E. Flanagan. “Post-1-Newtonian equations of motion for systems of arbitrarily structured bodies”. In: *Phys. Rev. D* 71 (2005). [Erratum: *Phys. Rev. D* 88,no.8,089903(2013)], p. 044010. DOI: 10.1103/PhysRevD.71.044010, 10.1103/PhysRevD.88.089903. arXiv: gr-qc/0404101 [gr-qc].
- [32] J. Vines, E. E. Flanagan, and T. Hinderer. “Post-1-Newtonian tidal effects in the gravitational waveform from binary inspirals”. In: *Phys. Rev. D* 83 (2011), p. 084051. DOI: 10.1103/PhysRevD.83.084051. arXiv: 1101.1673 [gr-qc].
- [33] T. Dietrich et al. “Matter imprints in waveform models for neutron star binaries: Tidal and self-spin effects”. In: *Phys. Rev. D* 99.2 (2019), p. 024029. DOI: 10.1103/PhysRevD.99.024029. arXiv: 1804.02235 [gr-qc].
- [34] M. Maggiore. *Gravitational Waves: Volume 2: Astrophysics and Cosmology*. Oxford Master Series in Physics. Oxford University Press, 2018. DOI: 10.1093/oso/9780198570899.001.0001.
- [35] A. Bauswein and H.-T. Janka. “Measuring neutron-star properties via gravitational waves from binary mergers”. In: *Phys.Rev.Lett.* 108 (2012), p. 011101. DOI: 10.1103/PhysRevLett.108.011101. arXiv: 1106.1616 [astro-ph.SR].

- [36] A. Bauswein et al. “Equation-of-state dependence of the gravitational-wave signal from the ring-down phase of neutron-star mergers”. In: *Phys.Rev.* D86 (2012), p. 063001. DOI: 10.1103/PhysRevD.86.063001. arXiv: 1204.1888 [astro-ph.SR].
- [37] K. Hotokezaka et al. “Remnant massive neutron stars of binary neutron star mergers: Evolution process and gravitational waveform”. In: *Phys.Rev.* D88.4 (2013), p. 044026. DOI: 10.1103/PhysRevD.88.044026. arXiv: 1307.5888 [astro-ph.HE].
- [38] A. Bauswein, N. Stergioulas, and H.-T. Janka. “Revealing the high-density equation of state through binary neutron star mergers”. In: *Phys.Rev.* D90.2 (2014), p. 023002. DOI: 10.1103/PhysRevD.90.023002. arXiv: 1403.5301 [astro-ph.SR].
- [39] K. Takami, L. Rezzolla, and L. Baiotti. “Constraining the Equation of State of Neutron Stars from Binary Mergers”. In: *Phys.Rev.Lett.* 113 (2014), p. 091104. DOI: 10.1103/PhysRevLett.113.091104. arXiv: 1403.5672 [gr-qc].
- [40] A. Bauswein and N. Stergioulas. “Unified picture of the post-merger dynamics and gravitational wave emission in neutron star mergers”. In: *Phys. Rev.* D91.12 (2015), p. 124056. DOI: 10.1103/PhysRevD.91.124056. arXiv: 1502.03176 [astro-ph.SR].
- [41] K. Takami, L. Rezzolla, and L. Baiotti. “Spectral properties of the post-merger gravitational-wave signal from binary neutron stars”. In: *Phys. Rev.* D91.6 (2015), p. 064001. DOI: 10.1103/PhysRevD.91.064001. arXiv: 1412.3240 [gr-qc].
- [42] S. Bernuzzi, T. Dietrich, and A. Nagar. “Modeling the complete gravitational wave spectrum of neutron star mergers”. In: *Phys. Rev. Lett.* 115 (2015), p. 091101. DOI: 10.1103/PhysRevLett.115.091101. arXiv: 1504.01764 [gr-qc].
- [43] L. Rezzolla and K. Takami. “Gravitational-wave signal from binary neutron stars: a systematic analysis of the spectral properties”. In: *Phys. Rev.* D93.12 (2016), p. 124051. DOI: 10.1103/PhysRevD.93.124051. arXiv: 1604.00246 [gr-qc].
- [44] S. Bose et al. “Neutron-star Radius from a Population of Binary Neutron Star Mergers”. In: *Phys. Rev. Lett.* 120.3 (2018), p. 031102. DOI: 10.1103/PhysRevLett.120.031102. arXiv: 1705.10850 [gr-qc].
- [45] J. Veitch et al. “Parameter estimation for compact binaries with ground-based gravitational-wave observations using the LALInference software library”. In: *Phys. Rev.* D91.4 (2015), p. 042003. DOI: 10.1103/PhysRevD.91.042003. arXiv: 1409.7215 [gr-qc].

- [46] B. Allen, K. Blackburn, et al. “LIGO Scientific Collaboration Algorithm Library Specification and Style Guide”. In: (2010). eprint: Tech. Rep. LIGO-T990030-v2.
- [47] C. M. Biwer et al. “PyCBC Inference: A Python-based parameter estimation toolkit for compact binary coalescence signals”. In: (2018). arXiv: 1807.10312 [astro-ph.IM].
- [48] L. S. Finn. “Detection, measurement and gravitational radiation”. In: *Phys. Rev. D* 46 (1992), pp. 5236–5249. DOI: 10.1103/PhysRevD.46.5236. arXiv: gr-qc/9209010 [gr-qc].
- [49] L. S. Finn. “Binary inspiral, gravitational radiation, and cosmology”. In: *Phys. Rev. D* 53 (1996), pp. 2878–2894. DOI: 10.1103/PhysRevD.53.2878. arXiv: gr-qc/9601048 [gr-qc].
- [50] M. van der Sluys et al. “Parameter estimation of spinning binary inspirals using Markov-chain Monte Carlo”. In: *Class. Quant. Grav.* 25 (2008), p. 184011. DOI: 10.1088/0264-9381/25/18/184011. arXiv: 0805.1689 [gr-qc].
- [51] A. W. Metropolis N.and Rosenbluth et al. In: *J. Chem. Phys.* 21.1087 (1952).
- [52] W. Hastings. “Monte Carlo sampling methods using Markov chains and their applications”. In: *Biometrika* 57 (1970), pp. 97–109.
- [53] B. P. Abbott et al. “Prospects for Observing and Localizing Gravitational-Wave Transients with Advanced LIGO, Advanced Virgo and KAGRA”. In: *Living Rev. Rel.* 21 (2018). [Living Rev. Rel.19,1(2016)], p. 3. DOI: 10.1007/s41114-018-0012-9, 10.1007/lrr-2016-1. arXiv: 1304.0670 [gr-qc].
- [54] J. Abadie et al. “Predictions for the Rates of Compact Binary Coalescences Observable by Ground-based Gravitational-wave Detectors”. In: *Class. Quant. Grav.* 27 (2010), p. 173001. DOI: 10.1088/0264-9381/27/17/173001. arXiv: 1003.2480 [astro-ph.HE].
- [55] B. P. Abbott et al. “GWTC-1: A Gravitational-Wave Transient Catalog of Compact Binary Mergers Observed by LIGO and Virgo during the First and Second Observing Runs”. In: (2018). arXiv: 1811.12907 [astro-ph.HE].
- [56] B. P. Abbott et al. “Gravitational Waves and Gamma-Rays from a Binary Neutron Star Merger: GW170817 and GRB 170817A”. In: *Astrophys. J.* 848.2 (2017). DOI: 10.3847/2041-8213/aa920c. arXiv: 1710.05834 [astro-ph.HE].
- [57] K.-W. Lo and L.-M. Lin. “The spin parameter of uniformly rotating compact stars”. In: *Astrophys.J.* 728 (2011), p. 12. DOI: 10.1088/0004-637X/728/1/12. arXiv: 1011.3563 [astro-ph.HE].

- [58] B. P. Abbott et al. “Properties of the binary neutron star merger GW170817”. In: *Phys. Rev. X* 9.1 (2019), p. 011001. DOI: 10.1103/PhysRevX.9.011001. arXiv: 1805.11579 [gr-qc].
- [59] S. Wanajo et al. “Production of all the r -process nuclides in the dynamical ejecta of neutron star mergers”. In: *Astrophys. J.* 789 (2014), p. L39. DOI: 10.1088/2041-8205/789/2/L39. arXiv: 1402.7317 [astro-ph.SR].
- [60] L. Blanchet. “Gravitational Radiation from Post-Newtonian Sources and Inspiralling Compact Binaries”. In: *Living Rev. Relativity* 17 (2014), p. 2. DOI: 10.12942/lrr-2014-2. arXiv: 1310.1528 [gr-qc].
- [61] T. Damour and G. Schäfer. “Lagrangians for n Point Masses at the Second Post-Newtonian Approximation of General Relativity”. In: *Gen. Relativ. Gravit.* 17 (1985), 879–905. DOI: <https://doi.org/10.1007/BF00773685>.
- [62] E. Poisson and C. M. Will. *Gravity, Newtonian, Post-Newtonian, Relativistic*. "Cambridge University Press", "2014". DOI: <https://doi.org/10.1017/CB09781139507486>.
- [63] A. Buonanno et al. “Comparison of post-Newtonian templates for compact binary inspiral signals in gravitational-wave detectors”. In: *Phys. Rev. D* 80 (2009), p. 084043. DOI: 10.1103/PhysRevD.80.084043. arXiv: 0907.0700 [gr-qc].
- [64] B. S. Sathyaprakash and S. V. Dhurandhar. “Choice of filters for the detection of gravitational waves from coalescing binaries”. In: *Phys. Rev. D* 44 (1991), pp. 3819–3834. DOI: 10.1103/PhysRevD.44.3819.
- [65] A. Bohé, S. Marsat, and L. Blanchet. “Next-to-next-to-leading order spin-orbit effects in the gravitational wave flux and orbital phasing of compact binaries”. In: *Class. Quant. Grav.* 30 (2013), p. 135009. DOI: 10.1088/0264-9381/30/13/135009. arXiv: 1303.7412 [gr-qc].
- [66] K. G. Arun et al. “Higher-order spin effects in the amplitude and phase of gravitational waveforms emitted by inspiraling compact binaries: Ready-to-use gravitational waveforms”. In: *Phys. Rev. D* 79 (2009). [Erratum: *Phys. Rev. D* 84,049901(2011)], p. 104023. DOI: 10.1103/PhysRevD.79.104023, 10.1103/PhysRevD.84.049901. arXiv: 0810.5336 [gr-qc].
- [67] B. Mikoeczi, M. Vasueth, and L. A. Gergely. “Self-interaction spin effects in inspiralling compact binaries”. In: *Phys. Rev. D* 71 (2005), p. 124043. DOI: 10.1103/PhysRevD.71.124043. arXiv: arXiv:astro-ph/0504538.

- [68] A. Bohé et al. “Quadratic-in-spin effects in the orbital dynamics and gravitational-wave energy flux of compact binaries at the 3PN order”. In: *Class. Quant. Grav.* 32.19 (2015), p. 195010. DOI: 10.1088/0264-9381/32/19/195010. arXiv: 1501.01529 [gr-qc].
- [69] C. K. Mishra et al. “Ready-to-use post-Newtonian gravitational waveforms for binary black holes with nonprecessing spins: An update”. In: *Phys. Rev. D* 93.8 (2016), p. 084054. DOI: 10.1103/PhysRevD.93.084054. arXiv: 1601.05588 [gr-qc].
- [70] E. Poisson. “Gravitational waves from inspiraling compact binaries: The Quadrupole moment term”. In: *Phys. Rev. D* 57 (1998), pp. 5287–5290. DOI: 10.1103/PhysRevD.57.5287. arXiv: gr-qc/9709032 [gr-qc].
- [71] A. Buonanno and T. Damour. “Effective one-body approach to general relativistic two-body dynamics”. In: *Phys. Rev. D* 59 (1999), p. 084006. DOI: 10.1103/PhysRevD.59.084006. arXiv: gr-qc/9811091.
- [72] A. Buonanno and T. Damour. “Transition from inspiral to plunge in binary black hole coalescences”. In: *Phys. Rev. D* 62 (2000), p. 064015. DOI: 10.1103/PhysRevD.62.064015. arXiv: gr-qc/0001013.
- [73] T. Damour. “The General Relativistic Two Body Problem and the Effective One Body Formalism”. In: *Proceedings, Relativity and Gravitation : 100 Years after Einstein in Prague*. 2012. DOI: 10.1007/978-3-319-06349-2_5. arXiv: 1212.3169 [gr-qc].
- [74] T. Damour, A. Nagar, and S. Bernuzzi. “Improved effective-one-body description of coalescing nonspinning black-hole binaries and its numerical-relativity completion”. In: *Phys. Rev. D* 87 (2013), p. 084035. DOI: 10.1103/PhysRevD.87.084035. arXiv: 1212.4357 [gr-qc].
- [75] T. Damour and A. Nagar. “New effective-one-body description of coalescing nonprecessing spinning black-hole binaries”. In: *Phys. Rev. D* 90.4 (2014), p. 044018. DOI: 10.1103/PhysRevD.90.044018. arXiv: 1406.6913 [gr-qc].
- [76] S. Bernuzzi et al. “Modeling the Dynamics of Tidally Interacting Binary Neutron Stars up to the Merger”. In: *Phys. Rev. Lett.* 114.16 (2015), p. 161103. DOI: 10.1103/PhysRevLett.114.161103. arXiv: 1412.4553 [gr-qc].
- [77] A. Nagar et al. “Time-domain effective-one-body gravitational waveforms for coalescing compact binaries with nonprecessing spins, tides and self-spin effects”. In: *Phys. Rev. D* 98.10 (2018), p. 104052. DOI: 10.1103/PhysRevD.98.104052. arXiv: 1806.01772 [gr-qc].

- [78] A. Bohé et al. “Improved effective-one-body model of spinning, nonprecessing binary black holes for the era of gravitational-wave astrophysics with advanced detectors”. In: *Phys. Rev. D* 95.4 (2017), p. 044028. DOI: 10.1103/PhysRevD.95.044028. arXiv: 1611.03703 [gr-qc].
- [79] M. Pürrer. “Frequency domain reduced order model of aligned-spin effective-one-body waveforms with generic mass-ratios and spins”. In: *Phys. Rev. D* 93.6 (2016), p. 064041. DOI: 10.1103/PhysRevD.93.064041. arXiv: 1512.02248 [gr-qc].
- [80] D. Bini and T. Damour. “Gravitational self-force corrections to two-body tidal interactions and the effective one-body formalism”. In: *Phys. Rev. D* 90.12 (2014), p. 124037. DOI: 10.1103/PhysRevD.90.124037. arXiv: 1409.6933 [gr-qc].
- [81] S. Bernuzzi et al. “Tidal effects in binary neutron star coalescence”. In: *Phys. Rev. D* 86 (2012), p. 044030. DOI: 10.1103/PhysRevD.86.044030. arXiv: 1205.3403 [gr-qc].
- [82] T. Dietrich and T. Hinderer. “Comprehensive comparison of numerical relativity and effective-one-body results to inform improvements in waveform models for binary neutron star systems”. In: *Phys. Rev. D* 95.12 (2017). DOI: 10.1103/PhysRevD.95.124006. arXiv: 1702.02053 [gr-qc].
- [83] B. D. Lackey et al. “Effective-one-body waveforms for binary neutron stars using surrogate models”. In: *Phys. Rev. D* 95.10 (2017), p. 104036. DOI: 10.1103/PhysRevD.95.104036. arXiv: 1610.04742 [gr-qc].
- [84] P. Ajith et al. “Inspirational-merger-ringdown waveforms for black-hole binaries with non-precessing spins”. In: *Phys. Rev. Lett.* 106 (2011), p. 241101. DOI: 10.1103/PhysRevLett.106.241101. arXiv: 0909.2867 [gr-qc].
- [85] L. London et al. “First higher-multipole model of gravitational waves from spinning and coalescing black-hole binaries”. In: *Phys. Rev. Lett.* 120.16 (2018), p. 161102. DOI: 10.1103/PhysRevLett.120.161102. arXiv: 1708.00404 [gr-qc].
- [86] S. Husa et al. “Frequency-domain gravitational waves from nonprecessing black-hole binaries. I. New numerical waveforms and anatomy of the signal”. In: *Phys. Rev. D* 93.4 (2016), p. 044006. DOI: 10.1103/PhysRevD.93.044006. arXiv: 1508.07250 [gr-qc].
- [87] S. Khan et al. “Frequency-domain gravitational waves from nonprecessing black-hole binaries. II. A phenomenological model for the advanced detector era”. In: *Phys. Rev. D* 93.4 (2016), p. 044007. DOI: 10.1103/PhysRevD.93.044007. arXiv: 1508.07253 [gr-qc].

- [88] M. Hannam et al. “Simple Model of Complete Precessing Black-Hole-Binary Gravitational Waveforms”. In: *Phys. Rev. Lett.* 113.15 (2014), p. 151101. DOI: 10.1103/PhysRevLett.113.151101. arXiv: 1308.3271 [gr-qc].
- [89] T. Dietrich, S. Bernuzzi, and W. Tichy. “Closed-form tidal approximants for binary neutron star gravitational waveforms constructed from high-resolution numerical relativity simulations”. In: *Phys. Rev.* D96.12 (2017), p. 121501. DOI: 10.1103/PhysRevD.96.121501. arXiv: 1706.02969 [gr-qc].
- [90] J. E. Vines and E. E. Flanagan. “Post-1-Newtonian quadrupole tidal interactions in binary systems”. In: *Phys. Rev.* D88 (2010), p. 024046. DOI: 10.1103/PhysRevD.88.024046. arXiv: 1009.4919 [gr-qc].
- [91] A. Nagar et al. “Energetics and phasing of nonprecessing spinning coalescing black hole binaries”. In: *Phys. Rev.* D93.4 (2016), p. 044046. DOI: 10.1103/PhysRevD.93.044046. arXiv: 1506.08457 [gr-qc].
- [92] Abbott, B. P. and others. “Properties of the Binary Neutron Star Merger GW170817”. In: *Phys. Rev. X* 9 (1 2019), 011001. DOI: {10.1103/PhysRevX.9.011001}.
- [93] K. Hotokezaka et al. “Exploring tidal effects of coalescing binary neutron stars in numerical relativity. II. Long-term simulations”. In: *Phys. Rev.* D91.6 (2015), p. 064060. DOI: 10.1103/PhysRevD.91.064060. arXiv: 1502.03457 [gr-qc].
- [94] B. P. Abbott et al. “GW170817: Observation of Gravitational Waves from a Binary Neutron Star Inspiral”. In: *Phys. Rev. Lett.* 119.16 (2017), p. 161101. DOI: 10.1103/PhysRevLett.119.161101. arXiv: 1710.05832 [gr-qc].
- [95] A. Viets et al. “Reconstructing the calibrated strain signal in the Advanced LIGO detectors”. In: *Class. Quant. Grav.* 35.9 (2018), p. 095015. DOI: 10.1088/1361-6382/aab658. arXiv: 1710.09973 [astro-ph.IM].
- [96] C. Cahillane et al. “Calibration uncertainty for Advanced LIGO’s first and second observing runs”. In: *Phys. Rev.* D96.10 (2017), p. 102001. DOI: 10.1103/PhysRevD.96.102001. arXiv: 1708.03023 [astro-ph.IM].
- [97] F. Acernese et al. “Calibration of Advanced Virgo and Reconstruction of the Gravitational Wave Signal $h(t)$ during the Science Run O2”. In: *Submitted to: Class. Quant. Grav.* (2018). arXiv: 1807.03275 [gr-qc].
- [98] B. P. Abbott et al. “Characterization of transient noise in Advanced LIGO relevant to gravitational wave signal GW150914”. In: *Class. Quant. Grav.* 33.13 (2016), p. 134001. DOI: 10.1088/0264-9381/33/13/134001. arXiv: 1602.03844 [gr-qc].

- [99] T. Dietrich et al. “Binary Neutron Stars with Generic Spin, Eccentricity, Mass ratio, and Compactness - Quasi-equilibrium Sequences and First Evolutions”. In: *Phys. Rev. D* 92.12 (2015), p. 124007. DOI: 10.1103/PhysRevD.92.124007. arXiv: 1507.07100 [gr-qc].
- [100] W. Kastaun et al. “On the black hole from merging binary neutron stars: how fast can it spin?” In: *Phys. Rev. D* 88 (2013), p. 021501. DOI: 10.1103/PhysRevD.88.021501. arXiv: 1301.7348 [gr-qc].
- [101] W. Kastaun and F. Galeazzi. “Properties of hypermassive neutron stars formed in mergers of spinning binaries”. In: *Phys. Rev. D* 91.6 (2015), p. 064027. DOI: 10.1103/PhysRevD.91.064027. arXiv: 1411.7975 [gr-qc].
- [102] N. Tacik et al. “Binary Neutron Stars with Arbitrary Spins in Numerical Relativity”. In: *Phys. Rev. D* 94.4 (2016), p. 049903. DOI: 10.1103/PhysRevD.94.049903, 10.1103/PhysRevD.92.124012. arXiv: 1508.06986 [gr-qc].
- [103] V. Paschalidis et al. “One-arm Spiral Instability in Hypermassive Neutron Stars Formed by Dynamical-Capture Binary Neutron Star Mergers”. In: *Phys. Rev. D* 92.12 (2015), p. 121502. DOI: 10.1103/PhysRevD.92.121502. arXiv: 1510.03432 [astro-ph.HE].
- [104] W. E. East et al. “Relativistic Simulations of Eccentric Binary Neutron Star Mergers: One-arm Spiral Instability and Effects of Neutron Star Spin”. In: *Phys. Rev. D* 93.2 (2016), p. 024011. DOI: 10.1103/PhysRevD.93.024011. arXiv: 1511.01093 [astro-ph.HE].
- [105] W. Kastaun et al. “Structure of Stable Binary Neutron Star Merger Remnants: Role of Initial Spin”. In: *Phys. Rev. D* 96.4 (2017), p. 043019. DOI: 10.1103/PhysRevD.96.043019. arXiv: 1612.03671 [astro-ph.HE].
- [106] K. Kiuchi et al. “Sub-radian-accuracy gravitational waveforms of coalescing binary neutron stars in numerical relativity”. In: *Phys. Rev. D* 96.8 (2017). DOI: 10.1103/PhysRevD.96.084060. arXiv: 1708.08926 [astro-ph.HE].
- [107] D. Radice, L. Rezzolla, and F. Galeazzi. “Beyond second-order convergence in simulations of binary neutron stars in full general-relativity”. In: *M.N.R.A.S.* 437 (2014), pp. L46–L50. DOI: 10.1093/mnrasl/slt137. arXiv: 1306.6052 [gr-qc].
- [108] M. Breschi et al. “kiloHertz gravitational waves from binary neutron star remnants: time-domain model and constraints on extreme matter”. In: (2019). arXiv: 1908.11418v1 [gr-qc].
- [109] A. Taracchini et al. “Effective-one-body model for black-hole binaries with generic mass ratios and spins”. In: *Phys. Rev. D* 89.6 (2014), p. 061502. DOI: 10.1103/PhysRevD.89.061502. arXiv: 1311.2544 [gr-qc].

- [110] S. Babak, A. Taracchini, and A. Buonanno. “Validating the effective-one-body model of spinning, precessing binary black holes against numerical relativity”. In: *Phys. Rev. D* 95.2 (2017), p. 024010. DOI: 10.1103/PhysRevD.95.024010. arXiv: 1607.05661 [gr-qc].
- [111] F. Zappa et al. “Gravitational-wave luminosity of binary neutron stars mergers”. In: *Phys. Rev. Lett.* 120.11 (2018), p. 111101. DOI: 10.1103/PhysRevLett.120.111101. arXiv: 1712.04267 [gr-qc].
- [112] F. Douchin and P. Haensel. “A unified equation of state of dense matter and neutron star structure”. In: *Astron. Astrophys.* 380 (2001), pp. 151–167. eprint: astro-ph/0111092.
- [113] H. Müller and B. D. Serot. “Relativistic mean field theory and the high density nuclear equation of state”. In: *Nucl. Phys.* A606 (1996), pp. 508–537. DOI: 10.1016/0375-9474(96)00187-X. arXiv: nucl-th/9603037 [nucl-th].
- [114] B. P. Abbott et al. “Effects of waveform model systematics on the interpretation of GW150914”. In: *Class. Quant. Grav.* 34.10 (2017), p. 104002. DOI: 10.1088/1361-6382/aa6854. arXiv: 1611.07531 [gr-qc].
- [115] D. Shoemaker and L. S. Collaboration. “Advanced LIGO anticipated sensitivity curves OBSOLETE”. In: (2010). eprint: Tech.Rep.LIGO-T0900288-v3.
- [116] C. Cutler and E. E. Flanagan. “Gravitational waves from merging compact binaries: How accurately can one extract the binary’s parameters from the inspiral wave form?” In: *Phys.Rev.* D49 (1994), pp. 2658–2697. DOI: 10.1103/PhysRevD.49.2658. arXiv: gr-qc/9402014 [gr-qc].
- [117] E. Poisson and C. M. Will. “Gravitational waves from inspiraling compact binaries: Parameter estimation using second postNewtonian wave forms”. In: *Phys.Rev.* D52 (1995), pp. 848–855. DOI: 10.1103/PhysRevD.52.848. arXiv: gr-qc/9502040 [gr-qc].
- [118] E. Baird et al. “Degeneracy between mass and spin in black-hole-binary waveforms”. In: *Phys. Rev.* D87.2 (2013), p. 024035. DOI: 10.1103/PhysRevD.87.024035. arXiv: 1211.0546 [gr-qc].
- [119] M. Hannam et al. “When can gravitational-wave observations distinguish between black holes and neutron stars?” In: *Astrophys.J.* 766 (2013), p. L14. DOI: 10.1088/2041-8205/766/1/L14. arXiv: 1301.5616 [gr-qc].
- [120] F. Ohme et al. “Statistical and systematic errors for gravitational-wave inspiral signals: A principal component analysis”. In: *Phys. Rev.* D88.4 (2013), p. 042002. DOI: 10.1103/PhysRevD.88.042002. arXiv: 1304.7017 [gr-qc].

- [121] J. A. Clark et al. “Observing Gravitational Waves From The Post-Merger Phase Of Binary Neutron Star Coalescence”. In: *Class. Quant. Grav.* 33.8 (2016), p. 085003. DOI: 10.1088/0264-9381/33/8/085003. arXiv: 1509.08522 [astro-ph.HE].
- [122] K. Chatziioannou et al. “Inferring the post-merger gravitational wave emission from binary neutron star coalescences”. In: *Phys. Rev.* D96.12 (2017), p. 124035. DOI: 10.1103/PhysRevD.96.124035. arXiv: 1711.00040 [gr-qc].
- [123] N. J. Cornish and T. B. Littenberg. “BayesWave: Bayesian Inference for Gravitational Wave Bursts and Instrument Glitches”. In: *Class. Quant. Grav.* 32.13 (2015), p. 135012. DOI: 10.1088/0264-9381/32/13/135012. arXiv: 1410.3835 [gr-qc].
- [124] A. Samajdar and T. Dietrich. “Waveform systematics for binary neutron star gravitational wave signals: Effects of spin, precession, and the observation of electromagnetic counterparts”. In: (2019). arXiv: 1905.03118 [gr-qc].
- [125] J. S. Read et al. “Measuring the neutron star equation of state with gravitational wave observations”. In: *Phys.Rev.* D79 (2009), p. 124033. DOI: 10.1103/PhysRevD.79.124033. arXiv: 0901.3258 [gr-qc].
- [126] A. Samajdar and T. Dietrich. “Waveform systematics for binary neutron star gravitational wave signals: effects of the point-particle baseline and tidal descriptions”. In: *Phys. Rev.* D98.12 (2018), p. 124030. DOI: 10.1103/PhysRevD.98.124030. arXiv: 1810.03936 [gr-qc].
- [127] F. Messina and A. Nagar. “Parametrized-4.5PN TaylorF2 approximants and tail effects to quartic nonlinear order from the effective one body formalism”. In: *Phys. Rev.* D95.12 (2017). [Erratum: *Phys. Rev.* D96,no.4,049907(2017)], p. 124001. DOI: 10.1103/PhysRevD.95.124001, 10.1103/PhysRevD.96.049907. arXiv: 1703.08107 [gr-qc].
- [128] A. Nagar et al. “Nonlinear-in-spin effects in effective-one-body waveform models of spin-aligned, inspiralling, neutron star binaries”. In: *Phys. Rev.* D99 (2019), p. 044007. DOI: 10.1103/PhysRevD.99.044007. arXiv: 1812.07923 [gr-qc].
- [129] S. Akcay et al. “Effective-one-body multipolar waveform for tidally interacting binary neutron stars up to merger”. In: *Phys. Rev.* D99.4 (2019), p. 044051. DOI: 10.1103/PhysRevD.99.044051. arXiv: 1812.02744 [gr-qc].
- [130] D. Shoemaker. eprint: <https://dcc.ligo.org/cgi-bin/DocDB/ShowDocument?docid=2974>.

- [131] T. Damour, A. Nagar, and L. Villain. “Measurability of the tidal polarizability of neutron stars in late-inspiral gravitational-wave signals”. In: *Phys.Rev.* D85 (2012), p. 123007. DOI: 10.1103/PhysRevD.85.123007. arXiv: 1203.4352 [gr-qc].
- [132] <http://www.black-holes.org/SpEC.html>. SpEC - Spectral Einstein Code.
- [133] A. H. Mroue et al. “A catalog of 174 binary black-hole simulations for gravitational-wave astronomy”. In: *Phys.Rev.Lett.* 111 (2013), p. 241104. DOI: 10.1103/PhysRevLett.111.241104. arXiv: 1304.6077 [gr-qc].
- [134] J. Blackman et al. “Fast and Accurate Prediction of Numerical Relativity Waveforms from Binary Black Hole Coalescences Using Surrogate Models”. In: *Phys. Rev. Lett.* 115.12 (2015), p. 121102. DOI: 10.1103/PhysRevLett.115.121102. arXiv: 1502.07758 [gr-qc].
- [135] T. Dietrich et al. “High-resolution numerical relativity simulations of spinning binary neutron star mergers”. In: *2018 26th Euromicro International Conference on Parallel, Distributed and Network-based Processing (PDP)*. 2018, pp. 682–689. DOI: 10.1109/PDP2018.2018.00113. arXiv: 1803.07965 [gr-qc].
- [136] S. E. Field et al. “Fast prediction and evaluation of gravitational waveforms using surrogate models”. In: *Phys.Rev.* X4.3 (2014), p. 031006. DOI: 10.1103/PhysRevX.4.031006. arXiv: 1308.3565 [gr-qc].
- [137] K. Yagi. “Multipole Love Relations”. In: *Phys. Rev.* D89.4 (2014), p. 043011. DOI: 10.1103/PhysRevD.89.043011. arXiv: 1311.0872 [gr-qc].
- [138] T. Yamamoto, M. Shibata, and K. Taniguchi. “Simulating coalescing compact binaries by a new code SACRA”. In: *Phys. Rev.* D78 (2008), p. 064054. DOI: 10.1103/PhysRevD.78.064054. arXiv: 0806.4007 [gr-qc].
- [139] M. Alcubierre. *Introduction to 3+1 Numerical Relativity*. Ed. by M. Alcubierre. Oxford University Press, 2008.
- [140] T. Baumgarte and S. Shapiro. *Numerical Relativity*. Cambridge: Cambridge University Press, 2010.
- [141] E. Gourgoulhon. “3+1 formalism and bases of numerical relativity”. In: (2007). arXiv: gr-qc/0703035 [GR-QC].
- [142] T. Dietrich. “Binary neutron star merger simulations”. Dissertation, Friedrich-Schiller-Universität Jena, 2016. PhD thesis. Jena, 2016.
- [143] M. Alcubierre et al. “On the hyperbolicity of the KST formulation of Einstein’s equations coupled to a modified Bona-Masso slicing condition”. In: *Phys. Rev.* D67 (2003), p. 104021. DOI: 10.1103/PhysRevD.67.104021. arXiv: gr-qc/0303086.

- [144] R. Arnotwitt, S. Deser, and C. Misner. “Canonical Variables for General Relativity”. In: *Physical Review* 117.6 (1960), pp. 1595–1602.
- [145] J. W. York. “Kinematics and Dynamics of General Relativity”. In: *Sources of gravitational radiation*. Ed. by L. L. Smarr. Cambridge, UK: Cambridge University Press, 1979, pp. 83–126.
- [146] T. Nakamura, K. Oohara, and Y. Kojima. “General Relativistic Collapse to Black Holes and Gravitational Waves from Black Holes”. In: *Prog. Theor. Phys. Suppl.* 90 (1987), pp. 1–218.
- [147] M. Shibata and T. Nakamura. “Evolution of three-dimensional gravitational waves: Harmonic slicing case”. In: *Phys. Rev. D* 52 (1995), pp. 5428–5444. DOI: 10.1103/PhysRevD.52.5428.
- [148] T. W. Baumgarte and S. L. Shapiro. “On the numerical integration of Einstein’s field equations”. In: *Phys. Rev. D* 59 (1999), p. 024007. DOI: 10.1103/PhysRevD.59.024007. arXiv: gr-qc/9810065.
- [149] D. Hilditch et al. “Compact binary evolutions with the Z4c formulation”. In: *Phys. Rev. D* 88 (2013), p. 084057. DOI: 10.1103/PhysRevD.88.084057. arXiv: 1212.2901 [gr-qc].
- [150] S. Bernuzzi and D. Hilditch. “Constraint violation in free evolution schemes: comparing BSSNOK with a conformal decomposition of Z4”. In: *Phys. Rev. D* 81 (2010), p. 084003. DOI: 10.1103/PhysRevD.81.084003. arXiv: 0912.2920 [gr-qc].
- [151] J. Wilson and G. Mathews. “Instabilities in Close Neutron Star Binaries”. In: *Phys.Rev.Lett.* 75 (1995), pp. 4161–4164. DOI: 10.1103/PhysRevLett.75.4161.
- [152] J. Wilson, G. Mathews, and P. Marronetti. “Relativistic numerical model for close neutron star binaries”. In: *Phys.Rev. D* 54 (1996), pp. 1317–1331. DOI: 10.1103/PhysRevD.54.1317. arXiv: gr-qc/9601017 [gr-qc].
- [153] J. York James W. “Conformal ‘thin sandwich’ data for the initial-value problem”. In: *Phys.Rev.Lett.* 82 (1999), pp. 1350–1353. DOI: 10.1103/PhysRevLett.82.1350. arXiv: gr-qc/9810051 [gr-qc].
- [154] W. Tichy. “Initial data for binary neutron stars with arbitrary spins”. In: *Phys. Rev. D* 84 (2011), p. 024041. DOI: 10.1103/PhysRevD.84.024041. arXiv: 1107.1440 [gr-qc].
- [155] W. Tichy. “Constructing quasi-equilibrium initial data for binary neutron stars with arbitrary spins”. In: *Phys. Rev. D* 86 (2012), p. 064024. DOI: 10.1103/PhysRevD.86.064024. arXiv: 1209.5336 [gr-qc].

- [156] J. A. Font. “Numerical hydrodynamics and magnetohydrodynamics in general relativity”. In: *Living Rev. Rel.* 11 (2007), p. 7.
- [157] L. Rezzolla and O. Zanotti. *Relativistic Hydrodynamics*. Oxford: Oxford University Press, 2013.
- [158] F. Banyuls et al. “Numerical 3+1 General Relativistic Hydrodynamics: A Local Characteristic Approach”. In: *Astrophys. J.* 476 (1997), p. 221.
- [159] J. S. Read et al. “Constraints on a phenomenologically parameterized neutron-star equation of state”. In: *Phys. Rev. D* 79 (2009), p. 124032. DOI: 10.1103/PhysRevD.79.124032. arXiv: 0812.2163 [astro-ph].
- [160] Ericourgoulhon, Philippe Grandclément, Jean-Alain Marck, Jérôme Novak and Keisuke Taniguchi. <http://www.lorene.obspm.fr/>. Paris Observatory, Meudon section - LUTH laboratory.
- [161] N. Moldenhauer et al. “Initial data for binary neutron stars with adjustable eccentricity”. In: *Phys. Rev. D* 90.8 (2014), p. 084043. DOI: 10.1103/PhysRevD.90.084043. arXiv: 1408.4136 [gr-qc].
- [162] A. Tsokaros, K. Uryū, and L. Rezzolla. “New code for quasiequilibrium initial data of binary neutron stars: Corotating, irrotational, and slowly spinning systems”. In: *Phys. Rev. D* 91.10 (2015), p. 104030. DOI: 10.1103/PhysRevD.91.104030. arXiv: 1502.05674 [gr-qc].
- [163] F. Foucart et al. “Initial data for black hole-neutron star binaries: A Flexible, high-accuracy spectral method”. In: *Phys. Rev. D* 77 (2008), p. 124051. DOI: 10.1103/PhysRevD.77.124051. arXiv: 0804.3787 [gr-qc].
- [164] W. Tichy. “Black hole evolution with the BSSN system by pseudo-spectral methods”. In: *Phys.Rev. D* 74 (2006), p. 084005. DOI: 10.1103/PhysRevD.74.084005. arXiv: gr-qc/0609087 [gr-qc].
- [165] W. Tichy. “A New numerical method to construct binary neutron star initial data”. In: *Class.Quant.Grav.* 26 (2009), p. 175018. DOI: 10.1088/0264-9381/26/17/175018. arXiv: 0908.0620 [gr-qc].
- [166] S. Bernuzzi et al. “Mergers of binary neutron stars with realistic spin”. In: *Phys.Rev. D* 89 (2014), p. 104021. DOI: 10.1103/PhysRevD.89.104021. arXiv: 1311.4443 [gr-qc].
- [167] J. W. T. Hessels et al. “A radio pulsar spinning at 716-hz”. In: *Science* 311 (2006), pp. 1901–1904. DOI: 10.1126/science.1123430. arXiv: astro-ph/0601337 [astro-ph].
- [168] R. S. Lynch et al. “The Timing of Nine Globular Cluster Pulsars”. In: *Astrophys. J.* 745 (2012), p. 109. DOI: 10.1088/0004-637X/745/2/109. arXiv: 1112.2612 [astro-ph.HE].

- [169] K. Stovall et al. “PALFA Discovery of a Highly Relativistic Double Neutron Star Binary”. In: *Astrophys. J.* 854.2 (2018), p. L22. DOI: 10.3847/2041-8213/aaad06. arXiv: 1802.01707 [astro-ph.HE].
- [170] M. Agathos et al. “Constraining the neutron star equation of state with gravitational wave signals from coalescing binary neutron stars”. In: *Phys. Rev. D* 92.2 (2015), p. 023012. DOI: 10.1103/PhysRevD.92.023012. arXiv: 1503.05405 [gr-qc].
- [171] M. Thierfelder, S. Bernuzzi, and B. Brügmann. “Numerical relativity simulations of binary neutron stars”. In: *Phys. Rev. D* 84 (2011), p. 044012. DOI: 10.1103/PhysRevD.84.044012. arXiv: 1104.4751 [gr-qc].
- [172] B. Bruegmann et al. “Calibration of Moving Puncture Simulations”. In: *Phys. Rev. D* 77 (2008), p. 024027. DOI: 10.1103/PhysRevD.77.024027. arXiv: gr-qc/0610128 [gr-qc].
- [173] T. Dietrich et al. “Numerical relativity simulations of neutron star merger remnants using conservative mesh refinement”. In: *Phys. Rev. D* 91.12 (2015), p. 124041. DOI: 10.1103/PhysRevD.91.124041. arXiv: 1504.01266 [gr-qc].
- [174] C. Bona et al. “A Class Of Hyperbolic Gauge Conditions”. In: *The Seventh Marcel Grossmann Meeting: On Recent Developments in Theoretical and Experimental General Relativity, Gravitation, and Relativistic Field Theories*. Ed. by R. T. Jantzen, G. M. Keiser, and R. Ruffini. Singapore: World Scientific, 1996.
- [175] M. Alcubierre et al. “Gauge conditions for long term numerical black hole evolutions without excision”. In: *Phys. Rev. D* 67 (2003), p. 084023. DOI: 10.1103/PhysRevD.67.084023. arXiv: gr-qc/0206072 [gr-qc].
- [176] K. Kyutoku, M. Shibata, and K. Taniguchi. “Reducing orbital eccentricity in initial data of binary neutron stars”. In: *Phys. Rev. D* 90.6 (2014), p. 064006. DOI: 10.1103/PhysRevD.90.064006. arXiv: 1405.6207 [gr-qc].
- [177] T. Dietrich et al. “Gravitational waves and mass ejecta from binary neutron star mergers: Effect of the mass-ratio”. In: *Phys. Rev. D* 95.2 (2017), p. 024029. DOI: 10.1103/PhysRevD.95.024029. arXiv: 1607.06636 [gr-qc].
- [178] T. Dietrich et al. “Gravitational waves and mass ejecta from binary neutron star mergers: Effect of the stars’ rotation”. In: *Phys. Rev. D* 95.4 (2017). DOI: 10.1103/PhysRevD.95.044045. arXiv: 1611.07367 [gr-qc].
- [179] P. Tsatsin and P. Marronetti. “Initial data for neutron star binaries with arbitrary spins”. In: *Phys. Rev. D* 88 (2013), p. 064060. DOI: 10.1103/PhysRevD.88.064060. arXiv: 1303.6692 [gr-qc].

- [180] T. Damour et al. “Energy versus Angular Momentum in Black Hole Binaries”. In: *Phys.Rev.Lett.* 108 (2012), p. 131101. DOI: 10.1103/PhysRevLett.108.131101. arXiv: 1110.2938 [gr-qc].
- [181] M. Levi and J. Steinhoff. “Next-to-next-to-leading order gravitational spin-squared potential via the effective field theory for spinning objects in the post-Newtonian scheme”. In: *JCAP* 1601 (2016), p. 008. DOI: 10.1088/1475-7516/2016/01/008. arXiv: 1506.05794 [gr-qc].
- [182] M. Levi and J. Steinhoff. “Equivalence of ADM Hamiltonian and Effective Field Theory approaches at next-to-next-to-leading order spin1-spin2 coupling of binary inspirals”. In: *JCAP* 1412.12 (2014), p. 003. DOI: 10.1088/1475-7516/2014/12/003. arXiv: 1408.5762 [gr-qc].
- [183] W. E. East and F. Pretorius. “Dynamical Capture Binary Neutron Star Mergers”. In: *Astrophys.J.* 760 (2012), p. L4. DOI: 10.1088/2041-8205/760/1/L4. arXiv: 1208.5279 [astro-ph.HE].
- [184] E. R. Most et al. “Impact of high spins on the ejection of mass in GW170817”. In: (2019). arXiv: 1904.0422v1 [astro-ph.HE].
- [185] T. Damour. “Coalescence of two spinning black holes: An effective one-body approach”. In: *Phys. Rev. D* 64 (2001), p. 124013. DOI: 10.1103/PhysRevD.64.124013. arXiv: gr-qc/0103018.
- [186] T. Damour, B. R. Iyer, and B. S. Sathyaprakash. “A Comparison of search templates for gravitational waves from binary inspiral”. In: *Phys. Rev. D* 63 (2001). [Erratum: *Phys. Rev.D*72,029902(2005)], p. 044023. DOI: 10.1103/PhysRevD.63.044023, 10.1103/PhysRevD.72.029902. arXiv: gr-qc/0010009 [gr-qc].
- [187] F. Messina et al. “Quasi-5.5PN TaylorF2 approximant for compact binaries: point-mass phasing and impact on the tidal polarizability inference”. In: *Phys. Rev. D* 99.12 (2019), p. 124051. DOI: 10.1103/PhysRevD.99.124051. arXiv: 1904.09558 [gr-qc].
- [188] T. Damour, B. R. Iyer, and A. Nagar. “Improved resummation of post-Newtonian multipolar waveforms from circularized compact binaries”. In: *Phys. Rev. D* 79 (2009), p. 064004. DOI: 10.1103/PhysRevD.79.064004. arXiv: 0811.2069 [gr-qc].
- [189] G. Faye, L. Blanchet, and B. R. Iyer. “Non-linear multipole interactions and gravitational-wave octupole modes for inspiralling compact binaries to third-and-a-half post-Newtonian order”. In: *Class. Quant. Grav.* 32.4 (2015). DOI: 10.1088/0264-9381/32/4/045016. arXiv: 1409.3546 [gr-qc].

- [190] F. Messina, A. Maldarella, and A. Nagar. “Factorization and resummation: A new paradigm to improve gravitational wave amplitudes. II: the higher multipolar modes”. In: *Phys. Rev. D* 97.8 (2018), p. 084016. DOI: 10.1103/PhysRevD.97.084016. arXiv: 1801.02366 [gr-qc].

Acknowledgement

I am really thankful to Prof. B. Brüggmann for offering me this position and providing me all the freedom to choose my projects and to collaborate, and also giving me advices beyond work. I am really grateful to Dr. Tim Dietrich for involving me in projects, mentoring me, not being angry with me, and for being a friend at times. I am thankful to Prof. Sebastiano Bernuzzi for teaching and encouraging me, and being so patient with me, Prof. Mark Hannam and Dr. Francesco Pannarale for adopting me, and Dr. Alessandro Nagar for introducing me to the world of PN/EOB framework. I want to thank Prof. Sukanta Bose, Prof. Sanjeev Dhurandhar, and Prof. Sanjit Mitra of IUCCA for giving me opportunities and supporting me.

I am thankful to Banaras city and all the beautiful souls I have met there who have influenced me and shaped me as a person. I would like to express my gratitude to Anuradha and Remya for providing me food and shelter with love, and to SANSKARS and Chanchal for supporting, encouraging, and pulling my legs at times. Thanks, guys, for just being a phone call away always. I like to thank Vivek for liberating discussions on so many topics ranging from Vedic history to corruption, what is real to what is not. Thank you so much for being there in the office all the time. Of course all the Francescos in the world deserves mentioning for teaching me how to party and how to hug and Hannes, for all the help since the time he picked me up from the train station when I first arrived.

Thanks Matteo, Michalis, Rossella, Archisman, Anuradha, Seb, for helping out with LAL. Thank you Sarp, Tim, Bhooshan, and Vivek for proofreading this thesis and correcting endless typos that too within the time constraint.

This thesis, my studies, this journey itself would not have been possible without the love, support and care from my Maa, Papa, Raju Bhaiya, Aruna Bhabhi, Holji, Dr. Ashok Jijaji, Guruji, and Shivashish. Thanks for teaching me the simple laws of life. You all are my world and soul. I am always immensely grateful to you all.

Selbstständigkeitserklärung

Ich erkläre hiermit, dass ich die vorliegende Arbeit selbständig, ohne unzulässige Hilfe Dritter und ohne Benutzung anderer als der angegebenen Hilfsmittel und Literatur angefertigt habe. Die aus anderen Quellen direkt oder indirekt übernommenen Daten und Konzepte sind unter Angabe der Quelle gekennzeichnet.

Bei der Auswahl und Auswertung dieser Arbeit haben mir die nachstehend aufgeführten Personen in beratender Weise unentgeltlich geholfen:

- Dr. Tim Dietrich
- Prof. Sebastiano Bernuzzi
- Prof. Bernd Brüggemann
- Dr. Francesco Pannarale
- Prof. Mark Hannam
- Dr. Nathan K. Johnson-McDaniel
- Dr. Alessandro Nagar
- Prof. Wolfgang Tichy
- M.Sc. Francesco Messina

In Bereichen bei denen auf Arbeit anderer zurückgegriffen wurde, ist dies ausdrücklich in der Arbeit erwähnt. Weitere Personen waren an der inhaltlich-materiellen Erstellung der vorliegenden Arbeit nicht beteiligt. Insbesondere habe ich hierfür nicht die entgeltliche Hilfe von Vermittlungs- bzw. Beratungsdiensten (Promotionsberater oder andere Personen) in Anspruch genommen. Niemand hat von mir unmittelbar oder mittelbar geldwerte Leistungen für Arbeiten erhalten, die im Zusammenhang mit dem Inhalt der vorgelegten Dissertation stehen. Die Arbeit wurde bisher weder im In- noch im Ausland in gleicher oder ähnlicher Form einer anderen Prüfungsbehörde vorgelegt.

Ich versichere ehrenwörtlich, dass ich nach bestem Wissen die reine Wahrheit gesagt und nichts verschwiegen habe.

Jena, 24.10.2019

Unterschrift

ॐ पूर्णमदः पूर्णमिदम् पूर्णात् पूर्णमुदच्यते । पूर्णस्य पूर्णमादाय पूर्णमेवावशिष्यते ॥ ॐ शान्तिः शान्तिः शान्तिः ॥